Integration of Local Positioning System & Strapdown Inertial Navigation System for Hand-Held Tool Tracking

by

Neda Parnian

A thesis
presented to the University of Waterloo
in fulfillment of the
thesis requirement for the degree of
Doctor of Philosophy
in
Electrical and Computer Engineering

Waterloo, Ontario, Canada, 2008

AUTHOR'S DECLARATION

I hereby declare that I am the sole author of this thesis. This is a true copy of the thesis, including any required final revisions, as accepted by my examiners.

I understand that my thesis may be made electronically available to the public.

Abstract

This research concerns the development of a smart sensory system for tracking a hand-held moving device to millimeter accuracy, for slow or nearly static applications over extended periods of time. Since different operators in different applications may use the system, the proposed design should provide the accurate position, orientation, and velocity of the object without relying on the knowledge of its operation and environment, and based purely on the motion that the object experiences. This thesis proposes the design of the integration a low-cost Local Positioning System (LPS) and a low-cost StrapDown Inertial Navigation System (SDINS) with the association of the modified EKF to determine 3D position and 3D orientation of a hand-held tool within a required accuracy.

A hybrid LPS/SDINS combines and complements the best features of two different navigation systems, providing a unique solution to track and localize a moving object more precisely. SDINS provides continuous estimates of all components of a motion, but SDINS loses its accuracy over time because of inertial sensors drift and inherent noise. LPS has the advantage that it can possibly get absolute position and velocity independent of operation time; however, it is not highly robust, is computationally quite expensive, and exhibits low measurement rate.

This research consists of three major parts: developing a multi-camera vision system as a reliable and cost-effective LPS, developing a SDINS for a hand-held tool, and developing a Kalman filter for sensor fusion.

Developing the multi-camera vision system includes mounting the cameras around the workspace, calibrating the cameras, capturing images, applying image processing algorithms and features extraction for every single frame from each camera, and estimating the 3D position from 2D images.

In this research, the specific configuration for setting up the multi-camera vision system is proposed to reduce the loss of line of sight as much as possible. The number of cameras, the position of the cameras with respect to each other, and the position and the orientation of the cameras with respect to the center of the world coordinate system are the crucial characteristics in this configuration. The proposed multi-camera vision system is implemented by employing four CCD cameras which are fixed in the navigation frame and their lenses placed on semicircle. All cameras are connected to a PC through the frame grabber, which includes four parallel video channels and is able to capture images from four cameras simultaneously.

As a result of this arrangement, a wide circular field of view is initiated with less loss of line-of-sight. However, the calibration is more difficult than a monocular or stereo vision system. The calibration of the multi-camera vision system includes the precise camera modeling, single camera calibration for each camera, stereo camera calibration for each two neighboring cameras, defining a unique world coordinate system, and finding the transformation from each camera frame to the world coordinate system.

Aside from the calibration procedure, digital image processing is required to be applied into the images captured by all four cameras in order to localize the tool tip. In this research, the digital image processing includes image enhancement, edge detection, boundary detection, and morphologic operations. After detecting the tool tip in each image captured by each camera, triangulation procedure and optimization algorithm are applied in order to find its 3D position with respect to the known navigation frame.

In the SDINS, inertial sensors are mounted rigidly and directly to the body of the tracking object and the inertial measurements are transformed computationally to the known navigation frame. Usually, three gyros and three accelerometers, or a three-axis gyro and a three-axis accelerometer are used for implementing SDINS. The inertial sensors are typically integrated in an inertial measurement unit (IMU). IMUs commonly suffer from bias drift, scale-factor error owing to non-linearity and temperature changes, and misalignment as a result of minor manufacturing defects. Since all these errors lead to SDINS drift in position and orientation, a precise calibration procedure is required to compensate for these errors.

The precision of the SDINS depends not only on the accuracy of calibration parameters but also on the common motion-dependent errors. The common motion-dependent errors refer to the errors caused by vibration, coning motion, sculling, and rotational motion. Since inertial sensors provide the full range of heading changes, turn rates, and applied forces that the object is experiencing along its movement, accurate 3D kinematics equations are developed to compensate for the common motion-dependent errors. Therefore, finding the complete knowledge of the motion and orientation of the tool tip requires significant computational complexity and challenges relating to resolution of specific forces, attitude computation, gravity compensation, and corrections for common motion-dependent errors.

The Kalman filter technique is a powerful method for improving the output estimation and reducing the effect of the sensor drift. In this research, the modified EKF is proposed to reduce the error of position estimation. The proposed multi-camera vision system data with cooperation of the modified EKF assists the SDINS to deal with the drift problem. This configuration guarantees the real-time position and orientation tracking of the instrument. As a result of the proposed Kalman filter, the effect of the gravitational force in the state-space model will be removed and the error which results from inaccurate gravitational force is eliminated. In addition, the resulting position is smooth and ripple-free.

The experimental results of the hybrid vision/SDINS design show that the position error of the tool tip in all directions is about one millimeter RMS. If the sampling rate of the vision system decreases from 20 fps to 5 fps, the errors are still acceptable for many applications.

Acknowledgements

This thesis represents four years of research work. During these years, I have been encouraged and supported by many people, and I take this opportunity to express my gratitude to them.

First, I would like to express my deep and sincere gratitude to my supervisor, Prof. Farid Golnaraghi, for giving me the opportunity to work in his group and for providing an excellent research environment. I cannot imagine having a better advisor and mentor for my PhD than Prof. Farid Golnaraghi. His confidence in me and in my capabilities gave me the inspiration to pursue my research with great intensity. Without his expertise and knowledge, his sharp perceptiveness, and his tireless support, I would never have completed this thesis.

I would also like to thank the members of my PhD committee who read and provided valuable comments on earlier versions of this thesis: Prof. Robert Gorbet, Prof. William W. Melek, Prof. Hamid R. Tizhoosh, and Prof. Khashayar Khorasani – I thank you all.

I would like to extend my special thanks to Robert Wagner, CNC technician, for his broad technical advice and support in configuring my test set-up. Also, my sincere appreciation goes to the Jason Benninger and John Potzold, Engineering machine shop technicians, for their assistance in creating the hand-held tool.

My warm thanks go to Steve Hitchman and Martha Morales, Computer Specialists, for their kind support in configuring, installing required software on, and maintaining my project PC.

I wish to express my warm and sincere thanks to my friends who created a friendly and pleasant atmosphere, including frequent social gatherings that helped my family and me not to feel lonely and depressed at living far away from our home town.

I appreciate the Ministry of Science, Research, and Technology of the Islamic Republic of Iran for sponsoring my PhD studies.

I cannot end without thanking my family for their constant encouragement and love. I wish to express my deepest and warmest gratitude to my parents for giving me life in the first place, for providing me the best education possible, and for their unconditional support and encouragement as I pursued my interests – even when these interests went beyond boundaries of language and geography.

My endless thanks are also extended to my brother, Navid, for his loving support. I am deeply indebted to him for taking care of my parents and giving them additional love when I was absent.

I owe my loving thanks to my husband, Habib, for his love and patience during my PhD studies. I am most grateful to him for leaving his job to give me the opportunity to continue my education, for helping me in taking care of my children, for listening to my complaints and frustrations, and at last, for believing in me. Without his encouragement and understanding it would have been impossible for me to finish this work.

Last but not the least, I would like to extend my special love to my sons, Hatef and Aref, who instill me with delightful energy and inspiration whenever I feel exhausted and frustrated – and fill my life with charm, joy, and happiness.

Dedication

I dedicate this thesis to my parents, my husband, and my sons. I would not have been able to complete my PhD studies and this thesis without their unconditional love, support, encouragement, and great patience. I deeply value their true love and concern.

Table of Contents

List of Figures xii

List of Tables xv

Chapter 1 Introduction 1

- 1.1 Thesis Overview 2
- 1.2 Literature Survey 3
  - 1.2.1 Medical Application 3
  - 1.2.2 Sensor Drift and Solutions 4
  - 1.2.3 Local Positioning System (LPS) 6
- 1.3 Research Objective 9
  - 1.3.1 New Contribution 10
  - 1.3.2 Publications 13
- 1.4 Summary 14

Chapter 2 Strapdown Inertial Navigation System 16

- 2.1 Inertial Measurement Unit (IMU) 17
  - 2.1.1 IMU Calibration 17
  - 2.1.2 Rate Gyros and Accelerometers Output Modeling 18
  - 2.1.3 Thermal Tests 20
- 2.2 Navigation Equations 21
  - 2.2.1 Reference Frames 21
  - 2.2.2 Motion Analysis 22
  - 2.2.3 Relative-Motion Analysis Using Translating and Rotating Axes 25
  - 2.2.4 Direction Cosine Matrix 30
  - 2.2.5 Quaternion 32
  - 2.2.6 Attitude Compensation 34
  - 2.2.7 Effect of Earth Rotation 35
  - 2.2.8 Physiological Hand Tremor 35
  - 2.2.9 State-Space of the System 36
- 2.3 Experimental Result 37
  - 2.3.1 IMU Calibration 37
  - 2.3.2 Noise and Physiological Hand Tremor Compensation 39
  - 2.3.3 Compensation for the Common Motion-Dependent Errors 41

2.3.4 Acceleration Computation 43

2.3.5 Attitude Computation... 46

2.4 Summary 48

Chapter 3 Local Positioning System 49

3.1 Multi-Camera Vision System.. 49

3.1.1 Configuration 50

3.1.2 Camera Modeling... 53

3.1.3 Single Camera Calibration 56

3.1.4 Stereo Camera Calibration 58

3.1.5 Defining the World Coordinate System.. 58

3.2 Digital Image Processing 59

3.2.1 Image Enhancement... 60

3.2.2 Edge Detection... 61

3.2.3 Boundary Extraction 63

3.2.4 Morphologic Operations 63

3.3 Experimental Results 65

3.3.1 Configuration Setup 66

3.3.2 Single Calibration 67

3.3.3 Stereo Calibration 77

3.3.4 Image Processing 77

3.3.5 Tool Tracking... 83

3.4 Summary 91

Chapter 4 Extended Kalman Filter.. 92

4.1 General Extended Kalman Filter... 93

4.1.1 System Model 93

4.1.2 Measurement Model 94

4.1.3 Extended Kalman Filter Equations 94

4.2 Modified Extended Kalman Filter 96

4.2.1 System Model 96

4.2.2 Measurement Model 100

4.3 Experimental Result.. 101

4.4 Summary 105

Chapter 5 Conclusion and Future Work ... 106
  5.1 Conclusion ... 106
  5.2 Contributions ... 107
  5.3 Future Work and Research ... 109
Bibliography ... 111
Appendix A Detailed Specification for MicroStrain IMU ... 121

List of Figures

Figure 1 - Gyros and accelerometers misalignments ... 17

Figure 2 - Hand-held tool and assigned reference frames ... 21

Figure 3 - The effect of rotation about x-axis on the output of y-axis accelerometer. ... 23

Figure 4 - The effect of rotation about y-axis on the output of x-axis accelerometer. ... 23

Figure 5 - The effect of coning motion around z-axis on the output of x-axis accelerometer. ... 24

Figure 6 - The effect of coning motion around z-axis on the output of y-axis accelerometer. ... 24

Figure 7 - Relative position ... 25

Figure 8 - Euler angels of the tool with respect to the NED frame ... 29

Figure 9 - Sensor's output correction block diagram ... 36

Figure 10 - Accelerometer bias without and with temperature compensation [8079] ... 38

Figure 11 - Accelerometer gain without and with temperature compensation [79] ... 38

Figure 12 - Gyro bias without and with temperature compensation [79] ... 38

Figure 13 - Gyro gain without and with temperature compensation [79] ... 39

Figure 14 - The output of accelerometers: measured (left) denoised (right) ... 40

Figure 15 - The output of gyros: measured (left) denoised (right) ... 40

Figure 16 - Accelerometers outputs while the tool is experiencing the rotational motion around x-axis ... 41

Figure 17 - Accelerometers outputs while the tool is experiencing the rotational motion around y-axis ... 42

Figure 18 - Acceleration error when the tool rotating around x-axis ... 42

Figure 19 - Acceleration error when the tool rotating around y-axis ... 43

Figure 20 - Estimated acceleration vs. measured acceleration in x axis ... 44

Figure 21 - Estimated acceleration vs. measured acceleration in y axis ... 44

Figure 22 - Estimated acceleration vs. measured acceleration in z axis ... 45

Figure 23 - Linear acceleration in x, y, and z axes ... 46

Figure 24 - Quaternion: estimated (solid) vs. true (doted) ... 47

Figure 25 - Quaternion error ... 47

Figure 26 - Euler angles error ... 48

Figure 27 - Cameras configuration set up ... 50

Figure 28 - The field of view of a multi-camera vision system when the lenses of its cameras are placed on a straight line ... 52

Figure 29 - The field of view of the proposed multi-camera vision system..53
Figure 30 - Ideal camera imaging model..54
Figure 31 - Radial and tangential distortion 55
Figure 32 - Checkerboard with 5 cm×5 cm squares..57
Figure 33 - The world coordinate system in the view of:
(a) camera #1 (b) camera #2 (c) camera #3 (d) camera #4..59
Figure 34 - Spatial averaging window mask: (a) 3×3 window (b) 5-point weighted low-pass filter...60
Figure 35 - Edge operators: (a)&(b) pair gradient operators, (c)&(d) single Laplace operators..........62
Figure 36 - Pixel connectivity: (a) four-connected (b) eight-connected...63
Figure 37 - Experimental setup for the multi-camera vision system..66
Figure 38 - Calibration images for camera #1 as a left camera for camera #2....................................67
Figure 39 - Calibration images for camera #2 as a right camera for camera #1..................................68
Figure 40 - Calibration images for camera #2 as a left camera for camera #3....................................68
Figure 41 - Calibration images for camera #3 as a right camera for camera #2..................................69
Figure 42 - Calibration images for camera #3 as a left camera for camera #4....................................69
Figure 43 - Calibration images for camera #4 as a right camera for camera #3..................................70
Figure 44 - Grid extraction for a sample image..71
Figure 45 - Complete distortion model of camera #1...72
Figure 46 - Radial component of distortion model of camera #1..73
Figure 47 - Tangential component of distortion model of camera #1 73
Figure 48 - Extrinsic parameters cam #1 in Figure 38: (left) camera-centered, (right) world-centered
....74
Figure 49 - Extrinsic parameters cam. #2 in Figure 39: (left) camera-centered, (right) world-centered
....74
Figure 50 - Extrinsic parameters cam. #2 in Figure 40: (left) camera-centered, (right) world-centered
....75
Figure 51 - Extrinsic parameters cam. #3 in Figure 41: (left) camera-centered, (right) world-centered
....75
Figure 52 - Extrinsic parameters cam. #3 in Figure 42: (left) camera-centered, (right) world-centered
....75
Figure 53 - Extrinsic parameters cam. #4 in Figure 43: (left) camera-centered, (right) world-centered
....76

Figure 54 - Original Image 78
Figure 55 - Denoised image 78
Figure 56 - Edge Enhancement 79
Figure 57 - Contrast Enhancement 79
Figure 58 - Detected edge by gradient operator 80
Figure 59 - Detected Edges 81
Figure 60 - The effect of opening morphologic operations followed by closing operation 81
Figure 61 - Extracted boundary of the tool tip 82
Figure 62 - Initial guess window mask for the position of tool tip 82
Figure 63 - Mask repositioning 83
Figure 64 - Tool tip tracking by camera #1 83
Figure 65 - Tool tip tracking by camera #2 84
Figure 66 - Tool tip tracking by camera #3 84
Figure 67 - Tool tip tracking by camera #4 84
Figure 68 - Comparison of the positioning with the use of two cameras (1&2) and four cameras 85
Figure 69 - Comparison of the positioning with the use of two cameras (2&3) and four cameras 86
Figure 70 - Comparison of the positioning with the use of two cameras (3&4) and four cameras 86
Figure 71 - The traced path by tool tip (red) in comparison with the pre-designed path (blue) 88
Figure 72 - The location of the maximum errors occurred during video tracking 88
Figure 73 - Integration of SDINS and vision system with using EKF 93
Figure 74 – The discrete difference of a Zero-mean Gaussian noise: 98
Figure 75 - Estimated position by applying different estimation method: continuous EKF (left), Switch EKF (center), and proposed EKF (right); when the sampling rate of the cameras is 16 fps. 103
Figure 76 - Estimated position by applying different estimation method: continuous EKF (left), Switch EKF (center), and proposed EKF (right); when the sampling rate of the cameras is 5 fps. .. 104

List of Tables

Table 1 - Camera specifications 65
Table 2 - Frame grabber specifications 66
Table 3 - Intrinsic parameters 71
Table 4 - Transformation parameters from each camera frame to the world coordinate system 76
Table 5 - Extrinsic parameters for each two adjacent cameras 77
Table 6 - The position error of the multi-camera vision system compared with each camera pair 87
Table 7 - Magnified images of the maximum errors in the tool tip positioning 89
Table 8 - Positions estimated by different estimation methods are compared with the position estimated by the multi-camera vision system 102

Chapter 1

Introduction

Over the past few decades, micro-electromechanical systems (MEMS) have been used in a wide range of research areas. Recently, MEMS have found new applications in medicine, especially surgery [1]. This technology provides real-time data, such as the surgical tool force, temperature, position, or direction, to improve the functionality of the surgical devices. The real-time feedbacks help surgeons to not only control the surgical procedure, but also develop new techniques for cutting and extraction.

During a medical operation, a surgeon is interested in knowing the position and orientation of surgical tools so as to control the surgery process with lowest possible risk. An endoscope is traditionally used for localizing surgical instruments in a patient. The view of the tools is not always ideal for estimating the position of an instrument precisely. Moreover, if the instrument is outside of the camera's view, then its position is unknown. Computer-aided surgery techniques deal with this problem by providing 3D models. An imaging device, such as MRI or CAT, scans the patient body during the operation and simulates 3D models with position and orientation to give a better view of the surgical area.

Tracking system technologies in this area are solely optically-based. In these tracking system techniques, two sets of markers are used for localization. Some markers are mounted on the surgical tools for tracking, and some are located on the specific position on the body of the patient for reference. Since the position of the reference markers are known, a computer can localize and align the tools with the image of the patient's body. The positions and orientations of the tool tips must be estimated by extrapolating techniques; but because of bending of the tools as well as the compression of tissues, these techniques are not precise and accurate. During a surgery, the markers must be in the field of view of the camera system, and the surgeon must pay attention not to obstruct, with arms or hands or surgical tools, the path from marker to cameras.

To deal with these issues, in this study a tracking system based on inertial sensors is proposed. As the MEMS fabrication techniques miniaturize the inertial sensors in size and weight, then MEMS-based inertial sensors can easily be mounted on a tool and do not interfere with the surgery.

The real-time states estimation of rigid bodies, including position, orientation, and velocity, has been the focus of research for several decades. The principal reason for this interest is its application in the guidance and navigation of aircraft and spacecraft and in robotics and automation. The best-known way of deriving position and orientation in these systems is to use inertial navigation sensors, which provide high frequency and continuous acceleration and rotation rate data. The inherent noise and biases of the sensors lead to unbounded and exponential error that grows in time. Researchers have long sought to aid inertial sensors with other sensors' measurements [2, 3]. A hybrid Inertial Navigation System (INS) can now provide a robust system with grouping of the best features of different tracking technologies, and compensate for their limitations by using multiple measurements.

The integration of vision and inertial measurements is an attractive solution to address both system problems. Vision measurements can be employed to reduce the INS drift that results from integrating noisy and biased inertial measurements. However, a vision system can provide the absolute position and velocity of a moving object independent of time, but, because of low measurement rate, it is difficult to meet the high dynamic range of fast moving. In addition, the image-based pose estimation is sensitive to the incorrect image feature tracking and camera modeling errors. Nevertheless, highly precise cameras such as Optotrak [4] can track an object in a high frequency and also provide the accurate position; these cameras are extremely expensive and are not even easily portable for use in many applications. Besides, keeping the moving object in the field of view requires the chaining of several of these cameras together.

This research proposes the integration of a low-cost multi-camera vision system and low-cost MEMS-based inertial sensors to provide a robust and cost-effective system. The proposed multi-camera vision system includes four common CCD cameras, with their lenses placed on an arc line. Accordingly, the total workspace of the vision system is expanded compared with the straight line configuration, an arrangement that reduces the possibility of the loss of the line-of-sight.

1.1 Thesis Overview

This thesis presents the development of the integration of the LPS/SDINS. The thesis is organized as follows. The rest of Chapter 1 reviews previous related work and results. It also presents our research and describes its application and its contribution to the state of knowledge. Chapter 2 describes the strapdown inertial navigation system, introduces the inertial measurement unit, and develops the navigation equations for a hand-held tool. Chapter 3 presents the LPS concepts, develops the multi-camera vision system, and gives details on calibration and vision tracking procedures. Chapter 4 discusses the sensor fusion via estimation filtering and proposes a modification of indirect Kalman filter for the application in hand. Finally, Chapter 5 summarizes the significant findings of this research and provides recommendations for future work.

1.2 Literature Survey

1.2.1 Medical Application

Positioning accuracy in microsurgery has recently been a focus of attention. Modern surgical tools for the improvement of microsurgical precision [5] use inertial navigation sensors to compensate for active tremor and improve human performance in micro-manipulation. In this approach, the hand-held microsurgical tool is equipped with a unique inertial measurement unit (IMU) [6], consisting of three dual-axis miniature accelerometers and a three-axis magnetometer. However, the six accelerometers of an IMU provide high resolution angular and translational components of the motion; they are drifting. The three-axis magnetometer with non-drifting but noisy output assists all-accelerometer IMU to overcome the drift problem. Therefore, a quaternion-based augmented-state Kalman filter [7] has been developed to estimate and improve the resolution of the orientation without drift. However, the accurate model of the system provides the precise estimation; the computational complexity increases, a fact that interferes with implementing in real-time. Nevertheless, their theoretical development presents the drift errors that would be eliminated, but in practice, they have had to make a simpler and more linear model to balance between time consumption and nonlinearity.

Another application of the inertial navigation sensors is the home-based rehabilitation program. Traditionally, physiotherapists help patients who have physical problems due to illness or injury to take physiotherapy as part of their rehabilitation activities. Recently, integration of vision and inertial sensors for arm [8, 9] and upper limb [10] motion tracking in a home-based rehabilitation program has been proposed. In this technique, a simple kinematic model of arm and forearm are considered. The arm is modeled as two rigid segments with known lengths, which are linked by a revolute joint. In this assumption, the upper arm has a three-degree of freedom (3D), and the forearm, including the hand, has a one-degree of freedom. The position of the shoulder is considered to be fixed, and the elbow position is calculated based on the fixed position of the elbow with respect to the shoulder. The rotation matrix can be calculated from Euler angles which come from the inertial sensors. The wrist position is found based on elbow position and image tracking results. However, a hybrid tracking system is used to follow the arm motion; during a short experiment (20 second), the result showed a large drift in the estimation [8]. Since the intrinsic sensor error is not modeled, the approach relies on the accelerometer readings to apply to the 2D image processing algorithm to calculate the position. Later, a new and simple orientation update technique is used to overcome the drift problem of gyros [11]. In this method, the outputs of gyros are taken into account when the changes in accelerometers' outputs are more than threshold. The result shows a significant improvement.

1.2.2 Sensor Drift and Solutions

Most of the research shows that the inertial navigation sensors have drifts. There are two drift components in the inertial sensors, bias stability and bias variability. The first one refers to the bias varying from turn-on to turn-on and is modeled as a Gaussian random constant. The second refers to the variability of bias after turn-on and is modeled as a random walk or first-order Markov process. Since these factors are involved in the inertial navigation computing task, they cause unavoidable drift in orientation and position estimation. Removing the drift of inertial navigation systems requires that the sensors be assisted with other resources or technologies. In fact, the sensor fusion can improve the estimation result and reduce the effect of the drifts. In order to sensor fusion, the Kalman filter, such as the traditional one or a modified version, is used to integrate data provided by various sensors and obtain the best estimate for the states of a system. The following collection of related aided technology serves as examples in order to discuss the method of each approach to solve the drift problem.

In the field of human movement tracking, a conventional IMU was used with the recommended Kalman filtering [12, 13]. However, the Kalman filter is a powerful technique to estimate output of a system; but for this particular case, the estimation cannot solely solve the drift problem, because the prediction based on the output of the inertial sensors, which has intrinsically drifted, always includes the drift. Since these researchers performing this work did not take advantage of any extra sensors to improve the estimation with the fusion of additional information, the drift still remains in the estimation results.

A miniature inertial sensing system for a head-mounted display has been presented in the area of virtual reality [14]. The sensing system is based on a three-accelerometer, three-gyro, and three-magnetometer system called InertiaCube. The InertiaCube uses the magnetometer output as a reference to remove errors resulting from the gyros' drift in the Euler angles estimation. The sensors fusion is achieved by a complementary separate-bias Kalman filter [15]. This approach provides an algorithm to correct the estimated orientation by using the output of accelerometers and magnetometers. However, such sensor errors as bias, scale-factor nonlinearity, and temperature dependency are not modeled explicitly. In this scope, another device called MARG has been invented [16, 17]. MARG consists of a three-axis magnetometer, three-axis angular rate, and three-axis gravity sensor to track human body movement and model humans in motion in a virtual environment The quaternion-based Kalman filter has been applied to combine the nine sensors outputs, and estimate orientation. Their approach takes advantage of the Gebre-Egziabher [18] method by combining the quaternion error to solve the nonlinear measurement equation with a lower numerical computational load. The dynamic error of the gyro is modeled using the Gauss-Markov process. In addition, a linear model is considered for the scale factor error and bias.

The global positioning system (GPS) is another interesting resource for consideration in the application of INS aiding. Although, GPS was developed for military purposes; it is now used as a navigation and positioning tool in airplanes, boats, and cars, and for many outdoor recreational activities. Finding the instantaneous three-dimensional position and velocity, and detecting the accurate time were the initial objectives of this system [19]. GPS is a satellite radio positioning system that provides continuous and low-rate data to track an object anywhere on or near the surface of the Earth. The non-drifting and noisy GPS signals might be lost for a while because of signal blocking, interference, or overcrowding [3]. However, the short-term loss never occurs in the use of IMU. Since both systems have complementary working characteristics, the integration of GPS and IMU associated with the Kalman filter is recommended. In order to achieve hybridization, different Kalman filtering methods are developed and implemented [20-25]. Although, the result shows that this method can deal with INS drift; the use of GPS is restricted to outdoor activities.

Generally, dead-reckoning or vision were used for mobile robot localization. In the dead-reckoning techniques, the odometer system is a common position sensor for mobile robots. Since it records total traversed distance by cumulating the travelled distances continuously, any sensing error is included in this accumulation and the error of estimated distances increases as time passes. To prevent excessive error and obtain accurate estimations of position and orientation, dead-reckoning is integrated with the inertial navigation sensors [26]. Owing to the intrinsic error of both IMU and odometer, the data fusion requires precision calibration of the IMU [27]. The dead-reckoning methods are not suitable for use in precise manipulation applications since small movements cannot be sensed and slow signal processing does not allow real-time processing. In vision-based robot localization, the robot equipped by camera finds its current location using different features extracted from visual information of the environment. Each feature and its corresponding position are stored in a database, and the robot retrieves its position by comparing the current extracted feature with the database and finding the most similar vector. Lately, the inertial sensors have been playing a role in robot positioning [28, 29] as well as augmented reality [30, 31].

Most vision-based hybrid INS systems are based on a monocular vision system [29, 30]. While the inertial sensors measure the components of the motion, the current position of the moving object is simultaneously determined by using visual information from the surrounding environment. In fact, a camera is mounted on the object, and a database of various features corresponding to a landmark is established. During object navigation, several images are captured and then different invariant features are extracted. The extracted feature vector is compared with those in the database. The current position can be retrieved once the optimum vector is found. Then, the sensor fusion algorithm estimates the current state of the object. In many applications, land marking is not practical or is hard to implement. Besides, mounting a camera on the tracking object is not possible because of the size and weight of the camera compared with the dimensions of the object. However, two-camera vision systems are used in particular applications [9, 10, 28, 32, 33]; they have a limited field of view and accuracy.

Without considering the result of the above hybrid vision-inertial systems, the robot's precision is not satisfactory and reasonable in precise manipulation tasks.

1.2.3 Local Positioning System (LPS)

The Local Positioning System (LPS) is a system with the capability of detecting, tracking, and localizing multiple targets accurately in real-time in an indoor environment. Typical applications of LPS include resource management [34], robot localization [35, 36], environment monitoring [37], and people-tracking for purposes of special supervision [38] and public safety [39].

The target or moving object is equipped with a small transmitter that includes a micro-controller and an emitting device. The emitting device sends the identification of the target to the LPS receiver with a unique sequence of on and off flashing.

The current localization systems can be classified by the core transmission techniques as IR, RF, ultrasound, magnetic, or electromagnetic. Their distinctive characteristics make them popular for different applications.

RF-based systems now have a low accuracy. However, they do not require a direct line of sight between sender and receiver, and their accuracy is considerably reduced by multiple-path and fading effects. Experience shows that the measurement results can be influenced even by the number of targets and by varying the number of objects standing close to a target [40].

In the ultrasound technique, targets emit an ultrasonic pulse to a set of ceiling-mounted receivers, such as the Active Bat system [41]. The objects can be located to within 9 cm of their true position. The accuracy of ultrasound-based systems suffers from reflections and obstacles between senders and receivers. However, the performance of these systems can be improved by establishing a dense network of receivers; this requirement makes them expensive, as well as complex to install.

Magnetic-based tracking systems are commonly used in virtual reality and motion capture applications. However, the magnetic tracking technique offers a high resolution; the use of magnetic-based systems is limited to a small and precisely controlled environment.

The electromagnetic systems are based on a network of wire coils covering the area of tracking. The accuracy of the electromagnetic systems is within a few millimeters in 3D; however, the large metal objects affect the electromagnetic systems; to achieve good accuracy, therefore, a precise calibration procedure is required. In addition, the infrastructure of these systems is such that it is difficult to install them in rooms with high ceilings.

Ultra-WideBand systems (UWBs) [42] are wireless communications techniques based on very high frequency signals, and their bandwidth is much wider than the conventional RF bandwidth. Furthermore, a higher receiver density than that in traditional RF systems is required. UWBs are capable to transmit pulses with duration as short as nanosecond or less. Since these systems are less affected by multi-path than are conventional RF systems, they can be accurate to about 5 cm in 3D. Besides, they can be installed much easier than ultrasound and electromagnetic systems.

Infrared (IR) optical-based systems cover a wide range of field [41], but they require a direct line of sight between transmitter and receiver. This means that obstacles and surfaces cause the communication linkage between senders and receivers to be missed. However, the emitters must be mounted at uncovered places; this constraint does not severely limit their use.

Considering the complementary working characteristic of RF- and IR-localization systems, researchers have started to focus attention on finding effective means to combine these two systems into a hybrid localization system with higher accuracy and better performance than previous systems [43, 44]. Thus, large rooms can be covered easily and positioning within the room is possible with less limitation; however, the complexity of the system is drastically increased.

An IR-LPS for smart items and devices is designed for integration with a camera [40]. This system covers a wide area (~100m^2) and tracks a large number of targets with a constant sampling rate without impacting on performance significantly. The result shows the accuracy is about 8 cm over a small range and 16 cm over a wide range. As well, the multi-robot positioning experiment [43], which takes advantage of the hybrid IR/RF communication system, shows that the measured distance error is relative to the range of view; the target can be located within 3.25 cm to 15 cm of its true position. In addition, bandwidth, sampling time, number of targets, and some hardware intrinsic bottlenecks are restricted when using this system.

Typically available IR optical tracking systems, such as Optotrak [4] and Firefly [45], are used mostly in precise applications, given that the accurate and instantaneous responses are two vital and crucial factors. The IR optical systems can cover and bring up to the field of view a wide region, while the Optotrak positional resolution and accuracy of positioning each marker in 3D is about 0.002 mm and 0.05 mm at 2.5 m respectively. Accordingly, even though IR optical systems are extremely expensive, their use in medical applications has grown. On the other hand, in most vision-based tracking systems including Optotrak, cameras are aligned on a straight line. When applications require keeping the object in the field of view during all of its movement, several of these optical systems must be chained together, creating an exceedingly expensive tracking system.

1.3 Research Objective

In this research, we propose a Local Positioning System (LPS)/SDINS for use in designing a hand-held tool tracking system. At the beginning of using the tool, a stationary reference point is affixed in the workspace. The ultimate goal here is to develop a hand-held tool, which is instrumented with MEMS sensors for full six degrees of freedom (6D) tracking. The tool is placed in the reference point in a mechanically stable and repeatable fashion. The measurement system is reset when the tool is placed in the reference position. This position is considered the origin, where acceleration due to gravity can be determined. The orientation is therefore determined relative to gravity. The tool can then be removed from the reference point. It is moved by hand to a point of interest in the workspace.

The end tip position and tool orientation must be tracked and be reported to a host computer for further analysis. This end-tip measurement and the attitude of the tool must remain accurate to better than one millimeter RMS and one degree RMS for duration of at least one minute as it is required for many applications in medicine and industry. An audible or visual indication must be made after such time that the system determines it can no longer accurately report the pose. The user then returns the tool to the reference holder to re-establish the origin. Remaining accurate for a time greater than one minute would be of great benefit as the operator does not require returning the tool frequently. The local coordinate system of the tool can be established relative to the reference holder by well-known registration techniques.

The LPS is designed to calculate the position and orientation of the tool. To implement the LPS, we locate a multi-camera vision system around the workspace, which is connected to our own computer to facilitate 6D position-orientation calculation during tool operation.

The proposed multi-camera vision system is implemented by employing CCD cameras which are fixed in the navigation frame and their lenses placed on a semicircle. All cameras are connected to a PC through the frame grabber, which includes four parallel video channels and is able to capture images from four cameras simultaneously. Digital image processing algorithms are applied to detect the tool with markers which are located on the body of the tool, determine the tool orientation, and find the 3D position of the tool tip with respect to the navigation frame.

In the SDINS, three accelerometers and three gyros are mounted rigidly and directly to the body of the tool in a three perpendicular axes frame. Since these sensors provide the full range of heading changes, turn rates, and applied forces that the object is experiencing along its movement, accurate 3D kinematics equations are developed to compensate for the motion-dependent errors caused by vibration, coning motion, sculling, and rotational motion.

In addition, the multi-camera vision system data with cooperation of the modified EKF aids the inertial sensors to deal with the drift problem.

The specifications of a final solution for a hand-held tool tracking are as follows:

- Measuring Devices for 6D (translational and rotations) or 3D (only rotations)
- Update rate of 100 Hz.
- Inexpensive
- Light weight and ergonomically balanced for the human hand.
- Auto-cleavable for at least 10 cycles (withstand storage temperatures of 125° C and high humidity).
- User-friendly push-buttons, LED indicators, and limited capacity programmable memory device.

1.3.1 New Contribution

The objective of this research is to design a reliable and cost-effective positioning system which is capable to locate precisely the position of the tool and determine accurately its orientation in real-time.

The accurate available positioning systems such as Optotrak are expensive and not affordable to be used in many applications such as industries. Therefore, the system is designed based on the cost-effective factor.

The performance of the positioning systems is not only evaluated based on the accuracy but also the measurement rate. The measurement rate of the existing positioning systems is reduced by increasing the number of markers. Keeping the sampling rate of the system at the same measurement rate that the system is operating with fewer markers requires extra hardware. Introducing more hardware to the system adds more complexity in hardware and software design. This means the price will be increased significantly.

One of the most important contributions of this research is that the proposed positioning system is capable to respond at the highest measurement rate at all time of operation, which is at least 100 HZ in order to response in real time.

The low-cost and high frequency features of the MEMS-based inertial sensors allow us to meet the high measurement rate requirement. Besides of these features, they are miniaturized in size and weight which allow them to be mounted on an object and without interfering with its operation. In addition, they can provide full dynamic range of the motion that the target is experiencing during its movement. All these characteristics make them popular in navigation applications; however, few research studies have been done in the field of the tool tracking [5]. Current tool tracking systems based on MEMS-based inertial sensors use 6 or 9 accelerometers and no rate gyros, which is call all-accelerometer IMU or gyro free IMU. Magnetometers are introduced in these systems to assist the accelerometers in estimating the 3D orientations. As the function of the magnetometers is affected easily by metals around the workspace, they are not appropriate for many applications. To address this problem, this research study proposes to employ a 3-axis accelerometer and a 3-axis rate gyro to estimate the 6D positions and orientations.

Although, the general equations of the SDINS computing task are applied in many navigation applications such as the navigation of land vehicles, airplanes, spacecrafts, and submarines; introducing MEMS-based inertial sensors in the tool tracking system whose accuracy should be in the range of few millimeters requires developing precise kinematics equations in order to minimize the SDINS errors resulting from the common motion-dependent errors as much as possible. The relative motion analysis and driven equations in the current research studies in this area are based on the gyro free assumption. The 3D relative motion analysis and developing required 3D kinematics equations for the hand-held tool including a three-axis rate gyro and a three-axis accelerometer is the other essential contribution of this thesis.

Even though, the drift error of the SDINS is significantly reduced by developing 3D kinematics equations and applying them into the general equations of the SDINS; but the SDINS still lose its accuracy over the time. This thesis recommends that the SDINS is integrated with another local positioning system associated with a sensor fusion technique to improve the accuracy of the system and keep it in the desired range for a longer period of the time.

However, GPS is commonly used for integrating with INS and SDINS in many outdoor applications; it is not recommended for indoor applications, since the satellite signals cannot penetrate the buildings materials. Vision systems are one of the most popular indoor tracking systems. Aside form Optotrak which is used three IR cameras and are not optical cameras, other research studies employ monocular or stereo vision systems in order to video tracking. One of the shortcomings of the vision systems is the loss of line of sight; which means the path between the target and the cameras will be blocked by obstacles and the video tracking will be failed.

Another significant contribution of this research is the design of a multi-camera vision system with individual configuration so as to prevent the loss of line of sight as much as possible. This configuration proposes to place the cameras along a semicircle in order to expand the angle of view and initiate a wide circular field of view.

As a matter of cost effectiveness, the low-cost CCD cameras are chosen to be employed in the proposed vision system. The more inexpensive cameras the smaller angle of view. As a result of smaller angle of view, more cameras are required to be employed to cover the entire circular workspace. However, utilizing more cameras introduces more complexity in calibration procedures and computer vision algorithms; the positioning error of the multi-camera vision system is significantly reduced. The number of required cameras is directly relative to the angle of view of the cameras. Since the angle of view of the chosen cameras in this project is $\frac{\pi}{8}$, four cameras are necessary for achieving the proposed arrangement.

As a result of this arrangement, an individual calibration procedure is designed to estimate the intrinsic and extrinsic parameters of the multi-camera vision system. In addition, the 3D position estimated by SDINS is provided in the navigation frame, therefore, a 3D transformation is required in order to map each point expressed in the world coordinate system of the multi-camera vision system into the navigation frame. First, the calibration procedure assigns a unique world coordinate system into the multi-camera vision system, and then provides a 3D homogenous transformation for each single camera to transform each point in camera frame into the unique world coordinate system and a 3D homogenous transformation to map each point in world coordinate system into the navigation frame.

Aside from the camera calibration, video tracking requires applying digital image processing and computer vision algorithms. To address the computation load problem of the video tracking, the simple and efficient algorithms for application in hand are selected.

Integration of the multi-camera vision system and SDINS requires an estimation method. Various types of EKF are developed for different application. These methods provide an estimation of the state variables or the errors. This research develops an EKF which offers the estimation of the changes in the state variables. Then the current estimated values of changes in the variables are added to the previous estimation. According to the general equations of the SDINS, the constant value of the gravitational force is removed from the resulted equations and the resulting error from the uncertainty value of the gravitational force is eliminated.

The inertial sensor noise is theoretically modeled with a zero-mean Gaussian random process. In reality, the actual mean of the noise is not absolutely zero. As a result of the proposed EKF and due to the inherent characteristic of the Gaussian random process, the average of the input noise is decreased while its variance is increased. It is expected that the resulting drift from input noise is reduced and smooth positioning is obtained.

1.3.2 Publications

Journals:

N. Parnian, M. F. Golnaraghi, 2007, “Integration of Vision and Inertial Sensors for Industrial Tools Tracking,” Sensor Review, Vol. 27, No. 2.

N. Parnian, M. F. Golnaraghi, 2008, “Compensation for the Common Motion-Dependent Errors in the Strapdown Inertial Navigation System in Application of a Hand-Held Tool Positioning,” Submitted to: IEEE Journal of selected topics in Signal Processing, Paper Number: ASPGRN.103

N. Parnian, M. F. Golnaraghi, 2008, “Integration of the Multi-Camera Vision System and SDINS with a modified EKF,” ready for submission.

N. Parnian, M. F. Golnaraghi, 2008, “A New Configuration for a Multi-Camera Vision System in its Integration with the Strapdown Inertial Navigation System for Hand-held Tool Tracking,” ready for submission.

Conferences:

N. Parnian, S.P. Won M. F. Golnaraghi, “Position Sensing Using Integration of a Vision System and Inertial Sensors,” Proceeding of IECON2008, November 2008, Orlando, Florida, USA.

S.P. Won, N. Parnian, M. F. Golnaraghi, W. Melek, “A Quaternion-Based Tilt Angle Correction Method for a Hand-Held Device Using an Inertial Measurement Unit,” Proceeding of IECON2008, November 2008, Orlando, Florida, USA.

N. Parnian, M. F. Golnaraghi, “A Low-Cost Hybrid SDINS/Multi-Camera Vision System for a Hand-held Tool Positioning,” Proceeding of IEEE/ION PLANS Conference, May 2008, Monterey, California, USA.

N. Parnian, M. F. Golnaraghi, “Hybrid Vision/Inertial Tracking for a Surgical Application,” NTC2007 Proceeding of the First Nano Technology Conference, February 2007, Shiraz, Iran.

N. Parnian, M. F. Golnaraghi, “Integration of Vision and Inertial Sensors for a Surgical Tool Tracking,” Proceedings of IMECE2006 2006 ASME International Mechanical Engineering Congress and Exposition, November 2006, Chicago, Illinois USA.

1.4 Summary

Our survey of the prior-art shows that there is a need for research in the area of precise positioning and the proposed topic will advance the state of knowledge in this field. In particular, the advancements from the proposed research will have the potential to benefit computer-assisted surgical devices in medical applications. The research will provide innovations in sensor tracking of devices utilizing the multi-camera vision system and inertial sensors, a new configuration and calibration method for the proposed vision system, and integration of the vision system and SDINS by introducing a new estimation algorithm.

Chapter 2

Strapdown Inertial Navigation System

Inertial navigation systems (INSs) were initially developed for military aviation applications. INSs are widely used in the positioning of various types of vehicles such as land vehicles, aircrafts, spacecrafts, and submarines. An INS is implemented based on two different techniques, gimbaling and strapdown systems.

The first system requires complicated, power consuming, and massive structures for gimbaling the inertial sensors on a mechanized-platform [46]. In the second system, inertial sensors are mounted on the body of a moving object [2] rather than a mechanized-platform. As a result of MEMS fabrication techniques, the inertial sensors such as accelerometers and angular rate gyros have been manufactured in a small size and light weight, allowing them to be strapped onto the moving object.

Because MEMS fabrication techniques have made inertial sensors low-cost and inexpensive, SDINS is allowed to be used for outdoor recreational activities, as well as for indoor environment applications such as medicine, industry, robotics, sports, virtual reality, and human motion tracking.

In an SDINS, inertial sensors are mounted rigidly and directly to the body of the tracking object and the inertial measurements are transformed computationally to the known navigation frame. The SDINS can continuously monitor the position and orientation of a moving object with respect to the known navigation reference frame, based on measuring its instantaneous linear acceleration and angular velocity with respect to the body reference frame and knowing its initial position, velocity, and attitude with respect to the navigation reference frame. Since the inertial measurements are in the body reference frame, computing the position and orientation requires a set of guidance navigation equations to transform the inertial measurements to the navigation reference frame.

In order to implement SDISN, three gyros and three accelerometers, or a three-axis gyro and a three-axis accelerometer are employed. These sensors are typically integrated in a unit which is referred to as inertial measurement unit (IMU).

2.1 Inertial Measurement Unit (IMU)

An Inertial Measurement Unit (IMU), includes gyros and accelerometers, is mounted on the moving object to track its motion, attitude, and position. IMUs commonly suffer from bias drift, scale-factor error owing to non-linearity and temperature changing, and misalignment as a result of minor manufacturing defects. All these errors lead to SDINS drift in position and orientation. Reducing the resulting drift in SDINS requires that the IMU be calibrated and parameters be estimated before mounting the IMU on a mobile object.

2.1.1 IMU Calibration

Calibration is the process of comparing a sensor's output with known reference quantities over the range of output values. The precision of the SDINS depends on the accuracy of calibration parameters such as scale factors and cross-coupling, measurement noise, and sensor bias.

An IMU measures acceleration and angular velocity in three perpendicular sensor axes, using one accelerometer and one gyro per axis. In a real device, these three sensor axes are not truly perpendicular owing to the minor manufacturing defects, as shown in Figure 1.

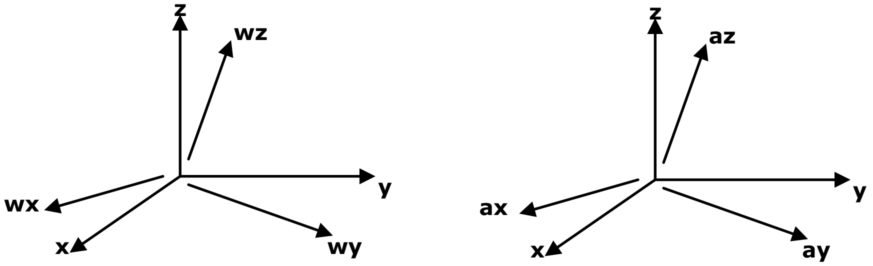

Figure 1 - Gyros and accelerometers misalignments

As a result of this misalignment, each sensor output is affected by sensing the motion in another direction and leading to SDINS drift. In addition, scale-factor error and inherent static bias are the common errors in sensors. The changing scale-factor error could be non-linear [32, 47], and the bias error usually does not remain static but changes dynamically [48-50]. Error modeling of gyros and accelerometers is required to apply the calibration process.

2.1.2 Rate Gyros and Accelerometers Output Modeling

The outputs of the rate gyros and accelerometers are electrical signals that are proportional to the angular rate and the specific force. For these sensors, the following model is widely used [51]:

$$\begin{aligned} \tilde{\omega}(t) &= \omega(t) + b_{\omega}(t) + \zeta(t) \\ \dot{b}_{\omega}(t) &= \eta(t) \end{aligned} \tag{2.1}$$

and

$$\begin{aligned} \tilde{a}(t) &= a(t) + b_a(t) + \varsigma(t) \\ \dot{b}_a(t) &= \xi(t) \end{aligned} \tag{2.2}$$

where $\tilde{\omega}(t)$ and $\omega(t)$ represent the continuous-time measured angular rate and the actual angular rate, $\tilde{a}(t)$ and $a(t)$ refer correspondingly to the continuous-time measured acceleration and the actual acceleration; $b_{\omega}(t)$ and $b_a(t)$ show the dynamic bias for gyro and accelerometer; and $\zeta(t)$, $\eta(t)$, $\varsigma(t)$, and $\xi(t)$ represent independent zero-mean Gaussian white noise process.

Since $\tilde{\omega}(t)$ and $\tilde{a}(t)$ are related to the output of gyros and accelerometers, a simple first-order model can be written in order to take into account the misalignment error:

$$\begin{aligned} \tilde{\omega}(t) &= M.v_g(t) \\ \tilde{a}(t) &= N.v_a(t) \end{aligned} \tag{2.3}$$

where $v_g(t)$ and $v_a(t)$ are 3×1 vectors and refer to the output voltage of the gyros and accelerometers in the three directions of x, y, and z; *M* and *N* are 3×3 matrices, while their diagonal indices represent the scale-factor and their off-diagonal indices show the misalignment factors.

Substituting equation (2.3) into equations (2.1) and (2.2) gives a simple model for estimating the scale-factors, misalignments, and biases by applying the least square technique:

$$\begin{aligned}\omega(t) &= M.v_g(t) - b_\omega(t) + \zeta(t)\\ a(t) &= N.v_a(t) + b_a(t) + \varsigma(t)\\ \dot{b}_\omega(t) &= \eta(t)\\ \dot{b}_a(t) &= \xi(t)\end{aligned} \tag{2.4}$$

Modern calibration techniques utilize the benefits of recursive least square estimation to achieve optimal estimates of the calibration parameters [52]. If a single-input single-output system is described by

$$y = Ax + b + n \tag{2.5}$$

where *y* and *u* represent output and input respectively, *A* and *b* refer to the model parameters, and *n* is the input noise, then the system model can be rewritten as:

$$y = \begin{bmatrix} A \\ b \end{bmatrix} \begin{bmatrix} x & 1 \end{bmatrix} + n = \beta u + n \tag{2.6}$$

Then β, which consists of model parameters, is calculated as follows:

$$\begin{aligned}\beta_k &= \beta_{k-1} + K(y_k - \beta_{k-1}u_k)\\ P_k &= P_{k-1} - Ku_kP_{k-1}\\ K &= P_{k-1}u_k^T\left(\sigma^2 + u_kP_{k-1}u_k^T\right)^{-1}\end{aligned} \tag{2.7}$$

where σ is a variance of the noise measurement, $P_{2\times2}$ is the covariance matrix of the estimation, and $K_{2\times1}$ is the gain. Since the IMU is a nonlinear and multi-input multi-output (MIMO) system, equation (2.6) can be expanded with respect to equation (2.4) as follows [3]:

$$\begin{aligned}\begin{bmatrix}\omega\\ a\end{bmatrix} &= \begin{bmatrix}M\\ N\end{bmatrix}\begin{bmatrix}v_g\\ v_a\end{bmatrix} + \begin{bmatrix}b_\omega\\ b_a\end{bmatrix} + \begin{bmatrix}\zeta\\ \varsigma\end{bmatrix}\\ \begin{bmatrix}\omega\\ a\end{bmatrix} &= \begin{bmatrix}M & b_\omega & \mathbf{0} & 0\\ \mathbf{0} & 0 & N & b_a\end{bmatrix}\begin{bmatrix}v_g\\ 1\\ v_a\\ 1\end{bmatrix} + \begin{bmatrix}\zeta\\ \varsigma\end{bmatrix} \rightarrow Y = \beta U + \epsilon\end{aligned} \tag{2.8}$$

As a result, equation (2.7) is rewritten for the MIMO system as:

$$\begin{aligned} \beta_k &= \beta_{k-1} + K(Y_k - \beta_{k-1}U_k) \\ P_k &= P_{k-1} - KU_kP_{k-1} \\ K &= P_{k-1}U_k^T\left(R + U_kP_{k-1}U_k^T\right)^{-1} \end{aligned} \tag{2.9}$$

where R is the noise measurement covariance matrix.

Determining the unknown parameters requires measuring the output of gyros and accelerometers in different temperatures over the range when the actual angular rates and actual acceleration are known or obtained from the precise device, such as a turntable.

It is well known that the scale factors of inertial sensors are changing with temperature. These changes are considerable even the temperature is changing in the small range (see the result in the section 2.3.1). Since the hand-held tool can operate in different environment for different applications, then a wider range of temperature is considered for IMU calibration.

2.1.3 Thermal Tests

The thermal tests are employed to establish the variation in the calibration parameters with temperature; when either the sensor is working at the lowest or highest operating temperature. The sensor is usually placed in the thermal chamber allowing tests to be run at the sub-zero temperatures and increased to the high temperatures. Various tests can be carried out to study the behavior of the inertial sensors in different temperatures. Soak method and ramp method are two popular thermal tests for MEMS inertial sensors [53 , 54].

In the soak method, the sensor is put in the chamber for sufficient time allowing the sensor to establish its temperature at the temperature of the chamber. Then, the system records the output of the sensor.

In the ramp method, the response of the sensor is recorded during different rates of temperatures. The sensor is placed in the chamber with the variable temperature. The temperature is linearly increased or decreased during a given period of time. During this period, the output of the sensor and temperatures are recorded correspondingly.

2.2 Navigation Equations

A SDINS determines the position and orientation of the tracking object by measuring applied specific forces to, and turning rates of, the body. In order to obtain the position and attitude of the object with respect to the known navigation frame, a set of equations are required to compensate measured inertial components for common motion-dependent errors and transform compensated quantities to the navigation frame. Navigation equations provide the motion behavior of a known particle of a rigid moving object [3]. In order to derive the motion equations of the moving object, a precise definition of reference frames is required.

2.2.1 Reference Frames

Analyzing the three-dimensional motion of a rigid body requires the use of two reference frames: the body reference frame attaching to the body of a moving object, and the navigation frame.

Figure 2 shows the reference frames and a symmetric hand-held tool equipped with an IMU when the body frame aligned on the IMU coordinate system.

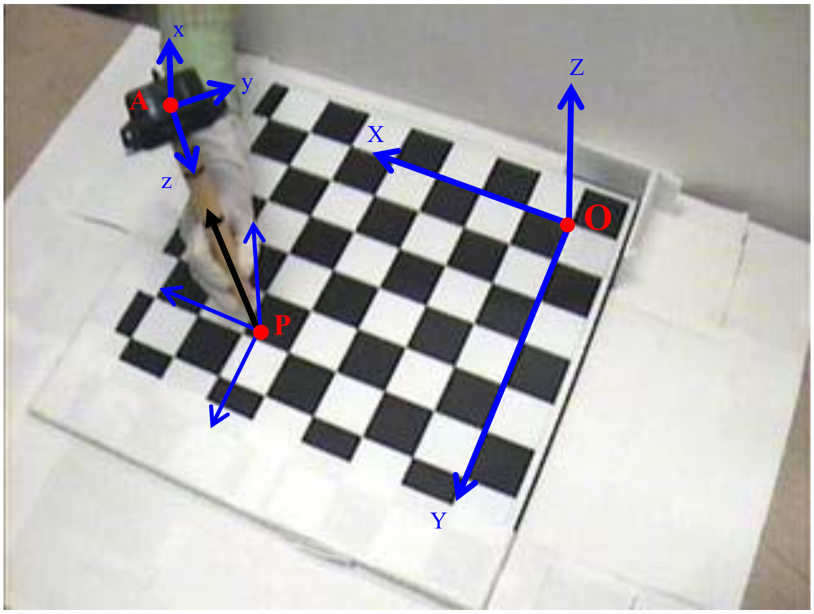

Figure 2 - Hand-held tool and assigned reference frames

When the position of the tool tip is desired, the IMU is attached to the bottom of the tool. The assigned body frame is the IMU frame, while its z-axis is aligned on the tool tip axis. The navigation frame is a fixed geographical reference frame whose x-axis points to the North, y-axis to the East, and z-axis to Down.

2.2.2 Motion Analysis

Motion analysis of a rigid body provides a set of equations determining its trajectory, speed, and attitude during its movement. Since the IMU measures the inertial components of the connected point, the acceleration and velocity of other points on the body can be computed relatively. Achieving complete knowledge of the motion and orientation of the tool tip requires significant computational complexity and challenges relating to resolution of specific forces, attitude computation, gravity compensation, and corrections for common motion-dependent errors.

The performance of a SDINS is certainly dependent on the motion of the host object. The precision of the SDINS depends not only on the accuracy of calibration parameters but also on the common motion-dependent errors. Many research studies on the subject of the inertial navigation do not take into account the common motion-dependent errors [2]. Their impact on the performance of the SDINS in aerospace and vehicle navigation can be neglected by applying some constraint on the motion. Even in some applications, such as navigation shoe [55, 56], autonomous underwater vehicles [57], or even oil drilling [58], the zero-update velocity is considered to address and cancel the effect of the common motion-dependent errors; but in the application of the hand-held tool tracking, these errors grow rapidly over time because of the non-restricted and non-constrained movement in 3D space.

The common motion-dependent errors refer to the errors caused by vibration, coning motion, sculling, and rotational motion [59, 60]. A number of motions can be experienced by inertial sensors that show the tool is moving; however, the tool tip still remains in the initial position. For instance, the tool is rotating alternately about either the x-axis or y-axis while the tool tip is fixed in the ground. As shown in Figure 3 and Figure 4, the accelerometer mounted on the y-axis or x-axis is correspondingly affected by this rotation; however, the tool tip is not moving. If the tool is experiencing the coning motion around z-axis, then both accelerometers of x-axis and y-axis would be affected, see Figure 5 and Figure 6.

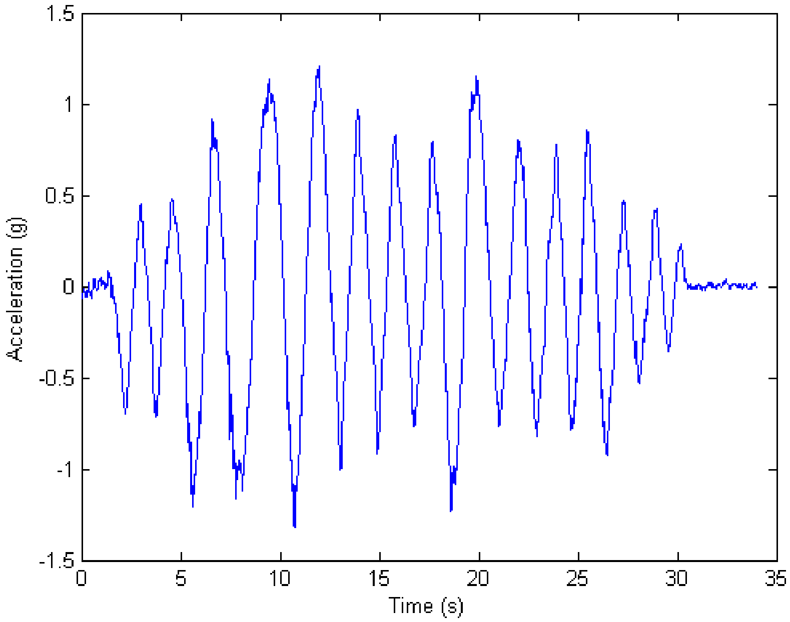

Figure 3 - The effect of rotation about x-axis on the output of y-axis accelerometer.

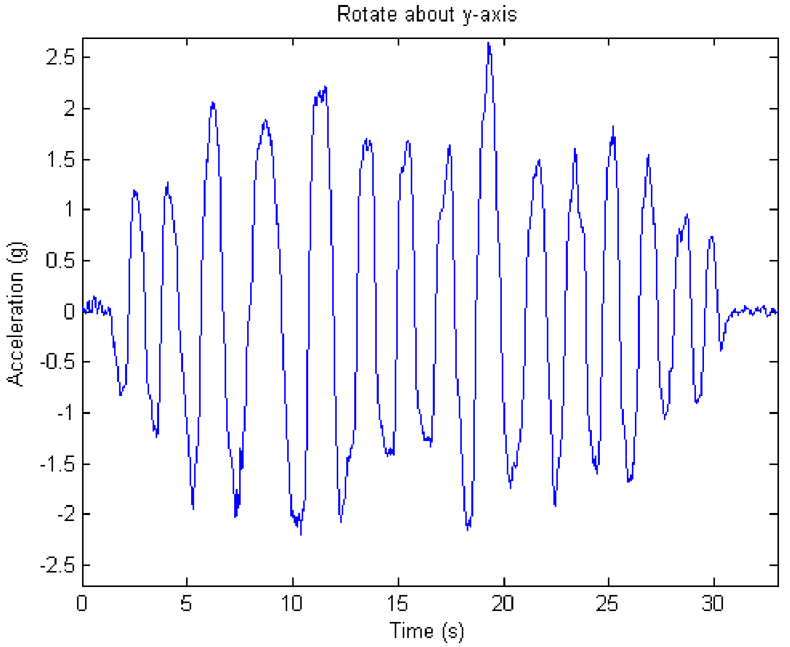

Figure 4 - The effect of rotation about y-axis on the output of x-axis accelerometer.

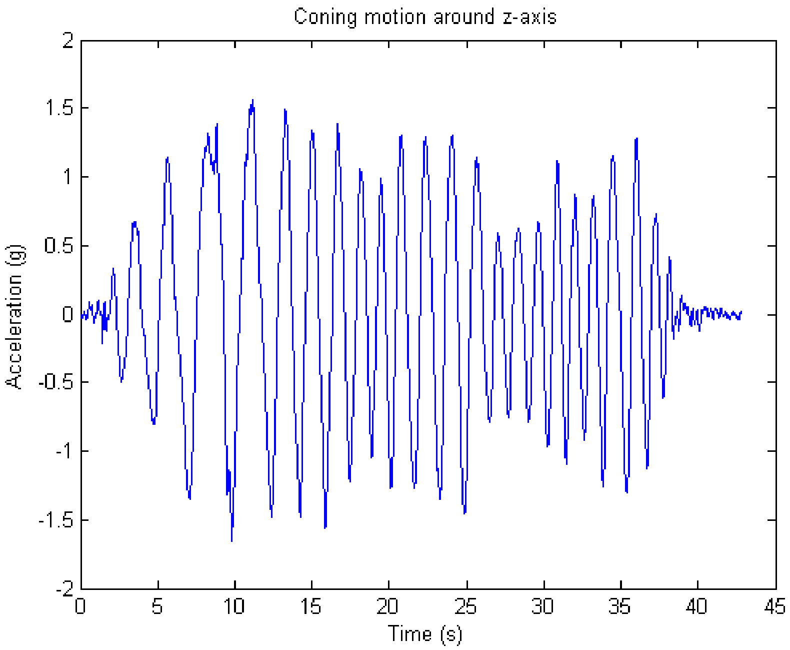

Figure 5 - The effect of coning motion around z-axis on the output of x-axis accelerometer.

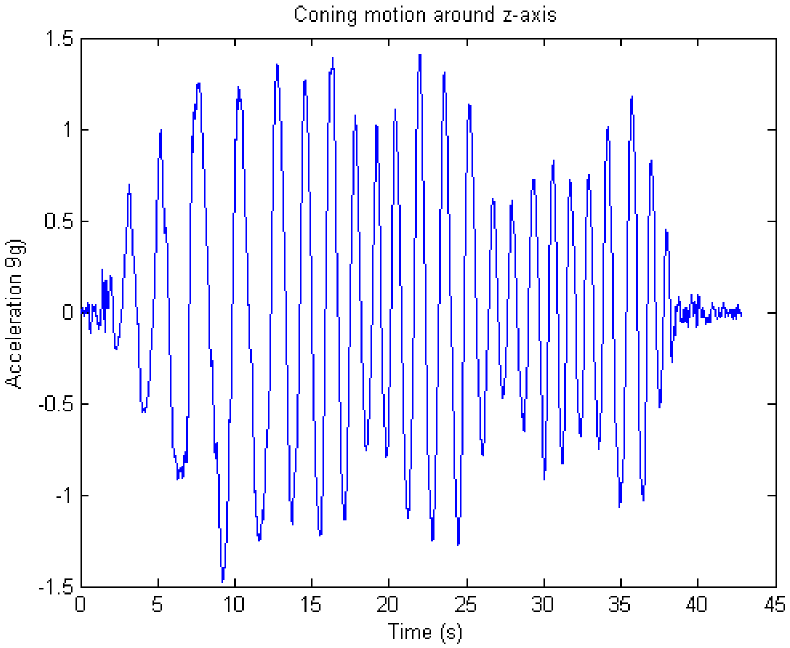

Figure 6 - The effect of coning motion around z-axis on the output of y-axis accelerometer.

Inertial sensors provide the full range of heading changes, turn rates, and applied forces that the object is experiencing along its movement. The accurate 3D kinematics equations for a hand-held tool are developed to compensate for the common motion-dependent errors.

2.2.3 Relative-Motion Analysis Using Translating and Rotating Axes

The hand-held tool is grabbed at the known point B by the fingers of an operator in order to perform the manipulation task. The possible motions are the translational motion of the tool tip and the rotational motion of the body. As a result of the tool rotation, the sculling and coning errors appear in the measurements. These errors must be taken into account in order to determine the absolute acceleration of the tool tip accurately. When the tool is rotating about its axes at the fixed point *P*, the Coriolis and centripetal accelerations are detected by accelerometers. The general kinematics equations [61] for the motion of two points *A* and *P*, the origin of the body frame aligned on the IMU reference frame and the tip of the tool shown in Figure 2, are derived by using the relative motion analysis.

If the position of point *A* with respect to point *P* measured in the local frame is denoted by the relative position vector $r_{A/P}$, Figure 7, then the vector summation rule gives:

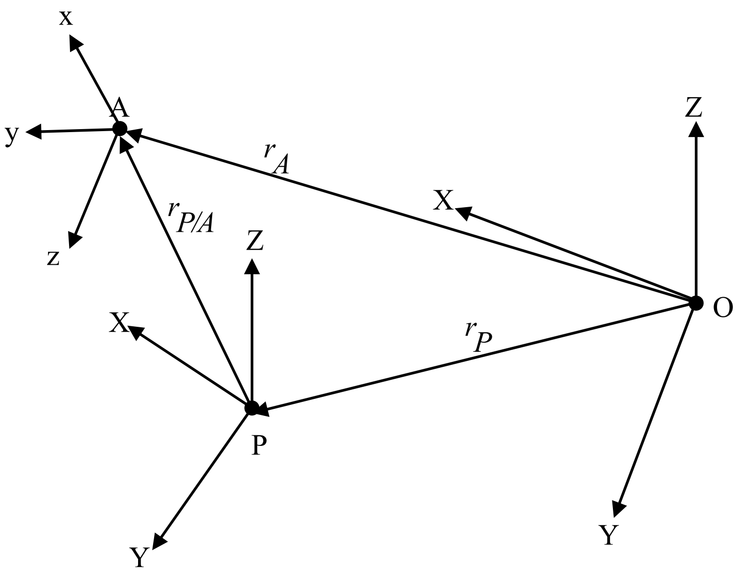

Figure 7 - Relative position

$$r_A = r_P + r_{A/P} \tag{2.10}$$

where r_A and r_P are vectors defining position of points *A* and *P* with respect to the navigation frame. The velocity of point *A* measured from navigation frame is obtained by taking the time derivative of equation (2.10):

$$\dot{r}_A = \dot{r}_P + \dot{r}_{A/P} \tag{2.11}$$

Since the body frame axes are rotating with respect to the navigation frame, the time derivative of each arbitrary vector in the body frame must take into account the change not only in the vector's magnitude but also in the vector's direction [62], meaning that:

$$\dot{k} = \left(\dot{k}\right)_{xyz} + \omega \times k \tag{2.12}$$

where k is an arbitrary vector in the body frame; $\dot{k}$ is its time derivative with respect to the fixed navigation frame; ω is a vector referring to the angular rate of the body frame measured in the fixed navigation frame; and "×" denotes the cross product operation.

By considering the angular velocity of body frame, ω, measured from navigation frame, the last term in equation (2.11) yields:

$$\dot{r}_{A/P} = (\dot{r}_{A/P})_{xyz} + \omega \times r_{A/P} \tag{2.13}$$

Then equation (2.11) is rewritten as:

$$\dot{r}_A = \dot{r}_P + (\dot{r}_{A/P})_{xyz} + \omega \times r_{A/P} \tag{2.14}$$

or

$$v_A = v_P + \omega \times r_{A/P} + (v_{A/P})_{xyz} \tag{2.15}$$

where v_A and v_P represent the velocity of points *A* and *P,* and $(v_{A/P})_{xyz}$ is the relative velocity of point *A* with respect to point *P* measured from the body frame. As well, the acceleration of point *A* measured form the navigation frame is calculated by taking the time derivative of equation (2.15):

$$\dot{v}_A = \dot{v}_p + \dot{\omega} \times r_{A/P} + \omega \times \dot{r}_{A/P} + \frac{d}{dt}(v_{A/P})_{xyz} \tag{2.16}$$

Once again, due to the rotation of the body frame with respect to the navigation frame, equation (2.12) will be applied into the last two terms of equation(2.16):

$$\begin{aligned} \omega \times \dot{r}_{A/P} &= \omega \times \left((\dot{r}_{A/P})_{xyz} + \omega \times r_{A/P}\right) \\ &= \omega \times (v_{A/P})_{xyz} + \omega \times \left(\omega \times r_{A/P}\right) \end{aligned} \tag{2.17}$$

$$\frac{d}{dt}(v_{A/P})_{xyz} = (\dot{v}_{A/P})_{xyz} + \omega \times (v_{A/P})_{xyz} \tag{2.18}$$

Substituting equations (2.17) and (2.18) into equation (2.16) yields:

$$\dot{v}_A = \dot{v}_p + \dot{\omega} \times r_{A/P} + \omega \times \left(\omega \times r_{A/P}\right) + 2\omega \times (v_{A/P})_{xyz} + (\dot{v}_{A/P})_{xyz} \tag{2.19}$$

or

$$a_A = a_P + \dot{\omega} \times r_{A/P} + \omega \times (\omega \times r_{A/P}) + 2\omega \times (v_{A/P})_{xyz} + (a_{A/P})_{xyz} \tag{2.20}$$

where a_A and a_P are the total acceleration of points *A* and *P*; $\dot{\omega}$ refers to the time derivative of angular velocity; and $(a_{A/P})_{xyz}$ denotes the relative acceleration of point *A* with respect to *P* measured in the body frame.

Since the estimation of the position of the tool tip, point *P*, is desired, a_P must be evaluated from equation (2.20) by measuring and evaluating other quantities.

According to Figure 2, the attached IMU measures both the angular velocity and applied forces at point *A*. This means that the angular velocity, ω, is measured by the gyros and $\dot{\omega}$ can be determined by taking the time derivate of ω. It is well known that the derivative of noisy signals produces a noisy result with the very large values. To address this problem, the data is smoothed before derivation and a low-pass filter is also applied after signal derivation.

The acceleration of point *A*, a_A, can be evaluated by using the following equation:

$$a_A = f_A + g_b \tag{2.21}$$

where f_A denotes applied forces or the accelerometer measurements, and g_b is the gravity vector represented in the body frame.

Since both points *P* and *A* located on the same rigid body and moving along the motion of the tool, the two terms $(v_{tip\,/A})_{xyz}$ and $(a_{tip\,/A})_{xyz}$ become zero. As demonstrated in Figure 7, $r_{A/P}$ is changing because of the rotation of the tool:

$$r_{A/P} = -\begin{bmatrix} L\sin\theta \\ -L\sin\phi \\ L\sqrt{1-\sin^2\theta-\sin^2\phi} \end{bmatrix} = -\begin{bmatrix} L\sin\theta \\ -L\sin\phi \\ LD \end{bmatrix} \tag{2.22}$$

Therefore, the total acceleration of the tool tip, a_P, is computed as:

$$a_P = f_A - \dot{\omega} \times r_{A/P} - \omega \times (\omega \times r_{A/P}) + g_b \tag{2.23}$$

The Euler angles corresponding to the roll, pitch, and yaw [63] are shown in Figure 8, and denoted with the angles ϕ, θ, and ψ, respectively. The length of the line *AP* which connects the tool tip to the origin of the body frame has a known value of L.

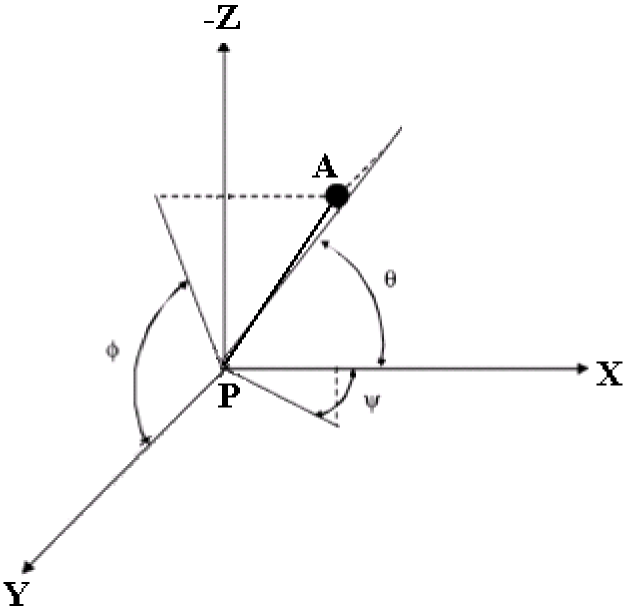

Figure 8 - Euler angels of the tool with respect to the NED frame

The direction of the attached local reference frame is the same as the direction of the navigation frame and translating only with respect to the navigation frame, while the tool is rotating only with respect to the local reference frame.

Expanding the second and third terms in equation (2.23) by considering $\omega = [\omega_x \ \omega_y \ \omega_z \ ]^T$ and $\dot{\omega} = [\dot{\omega}_x \ \dot{\omega}_y \ \dot{\omega}_z \ ]^T$, gives the following equations:

$$a_t = \dot{\omega} \times r_{A/P} = -L \begin{bmatrix} \dot{\omega}_y D - \dot{\omega}_z \sin\phi \\ \dot{\omega}_z \sin\theta - \dot{\omega}_x D \\ \dot{\omega}_x \sin\phi - \dot{\omega}_y \sin\theta \end{bmatrix} \tag{2.24}$$

$$a_n = \omega \times \left(\omega \times r_{A/P}\right) = -L \begin{bmatrix} \omega_x\omega_y \sin\phi + \omega_x\omega_z D - \omega_y^2 \sin\theta - \omega_z^2 \sin\theta \\ \omega_y\omega_z D + \omega_x\omega_y \sin\theta - \omega_x^2 \sin\phi - \omega_z^2 \sin\phi \\ \omega_x\omega_z \sin\theta + \omega_y\omega_z \sin\phi - \omega_y^2 D - \omega_x^2 D \end{bmatrix} \tag{2.25}$$

According to Figure 2, the possible sculling and rotation motion is about the x-axis and y-axis and the feasible conical motion is the circular cone traced by the z-axis. If equations (2.24) and (2.25) are rearranged as follows:

$$a_t = -L\begin{bmatrix} -\dot{\omega}_z \sin\phi \\ \dot{\omega}_z \sin\theta \\ 0 \end{bmatrix} - L\begin{bmatrix} \dot{\omega}_y D \\ -\dot{\omega}_x D \\ \dot{\omega}_x \sin\phi - \dot{\omega}_y \sin\theta \end{bmatrix} \tag{2.26}$$

$$a_n = -L\begin{bmatrix} \omega_x\omega_z D - \omega_z^2 \sin\theta \\ \omega_y\omega_z D + -\omega_z^2 \sin\phi \\ 0 \end{bmatrix} - L\begin{bmatrix} \omega_x\omega_z D - \omega_y^2 \sin\theta \\ \omega_x\omega_y \sin\theta - \omega_x^2 \sin\phi \\ \omega_x\omega_z \sin\theta + \omega_y\omega_z \sin\phi - \omega_y^2 D - \omega_x^2 D \end{bmatrix} \tag{2.27}$$

then the first terms and the second terms of equations (2.26) and (2.27) introduce the effect of the coning motion and the sculling/rotation motion, respectively. Therefore, equation (2.23) can be rewritten as:

$$a_P = f_A - a_t - a_n + g_b \tag{2.28}$$

Since the angular velocity, angular acceleration, and applied force in equation (2.28) are expressed in the body frame, a transformation matrix [64] is required to convert the acceleration of the tool tip from the body frame to the navigation frame.

2.2.4 Direction Cosine Matrix

The direction cosine matrix (DCM), C_b^n, is a 3×3 matrix that transforms any represented vector in the body frame, r^b, to the corresponding vector in the navigation frame, r^n,:

$$r^n = C_b^n r^b \tag{2.29}$$

Therefore, the acceleration of tool tip with respect to the navigation frame is computed as:

$$a_p = C_b^n (f_A - a_t - a_n) + g_n \tag{2.30}$$

where g_n denotes the gravity vector in the navigation frame $[0 \quad 0 \quad 9.81]^T$.

Obviously, the body frame is rotating with respect to the navigation frame around three directions during the movement of the tool, so the changes of direction cosine matrix should be calculated with respect to time. The changes in the rate of C_b^n with time is given by:

$$\dot{C}_b^n = \lim_{\delta t \to 0} \frac{\delta C_b^n}{\delta t} = \lim_{\delta t \to 0} \frac{C_b^n(t+\delta t) - C_b^n(t)}{\delta t} \tag{2.31}$$

where $C_b^n(t)$ and $C_b^n(t+\delta t)$ refer to the transformation matrix at times *t*, and $(t+\delta t)$. $C_b^n(t+\delta t)$ can be considered a product of two sequent rotations: a transformation from body frame to navigation frame and transformation from body frame at time *t* to body frame at time $(t+\delta t)$. As a result,

$$C_b^n(t+\delta t) = C_b^n(t)D(t) \tag{2.32}$$

The three rotations of body frame may be expressed as a transformation from one frame to another frame as:

$$D = \begin{bmatrix} \cos\theta\cos\psi & -\cos\phi\sin\psi + \sin\phi\sin\theta\cos\psi & \sin\phi\sin\psi + \cos\phi\sin\theta\cos\psi \\ \cos\theta\sin\psi & \cos\phi\cos\psi + \sin\phi\sin\theta\sin\psi & -\sin\phi\cos\psi + \cos\phi\sin\theta\sin\psi \\ -\sin\theta & \sin\phi\cos\theta & \cos\phi\cos\theta \end{bmatrix} \tag{2.33}$$

where ψ, θ, and ϕ are represented the Euler rotation angles. For a small angle rotation of $\delta\psi$, $\delta\theta$, and $\delta\phi$ which the body frame has rotated over the time interval δt about its yaw, pitch, and roll axes; $\sin\delta\psi \to \delta\psi$, $\sin\delta\theta \to \delta\theta$, and $\sin\delta\phi \to \delta\phi$; and the cosines of these angles approach unity. Making this substitution into equation (2.33) and ignoring the angles products, which are much smaller than the angles itself, gives:

$$D = \begin{bmatrix} 1 & -\delta\psi & \delta\theta \\ \delta\psi & 1 & -\delta\phi \\ -\delta\theta & \delta\phi & 1 \end{bmatrix} = \begin{bmatrix} 1 & 0 & 0 \\ 0 & 1 & 0 \\ 0 & 0 & 1 \end{bmatrix} + \begin{bmatrix} 0 & -\psi & \theta \\ \psi & 0 & -\phi \\ -\theta & \phi & 0 \end{bmatrix} = I + \delta\Psi \tag{2.34}$$

By substituting equation (2.34) into equation (2.32), the direction cosine matrix at time $(t+\delta t)$ is expressed in terms of the changes in Euler angles:

$$C_b^n(t+\delta t) = C_b^n(t)[I + \delta\Psi] \tag{2.35}$$

According to equation (2.31), the rate of changes of $C_b^n(t)$ can be rewritten as:

$$\dot{C}_b^n = C_b^n(t) \lim_{\delta t \to 0} \frac{\delta\Psi}{\delta t} \tag{2.36}$$

where

$$\lim_{\delta t \to 0} \frac{\delta \Psi}{\delta t} = \Omega_{nb}^{b} \tag{2.37}$$

In equation (2.37), Ω_{nb}^{b} denotes the skew-symmetric form of the angular rate vector $\omega_{nb}^{b} = [\omega_x \quad \omega_y \quad \omega_z]^T$, which refers to the turn rate of the body frame with respect to navigation frame expressed in body axes and measured by gyros. As a result, the changes in the rate of transformation matrix is calculated by the following equation:

$$\begin{aligned} \dot{C}_b^n &= C_b^n(t)\,\Omega_{nb}^{b} = C_b^n[\omega_{nb}^{n} \times] \\ \Omega_{nb}^{b} &= \begin{bmatrix} 0 & -\omega_z & \omega_y \\ \omega_z & 0 & -\omega_x \\ -\omega_y & \omega_x & 0 \end{bmatrix} \end{aligned} \tag{2.38}$$

2.2.5 Quaternion

The three-dimensional Euler angles representations were applied for attitude estimation in the SDINS, but these representations are singular or discontinuous for certain attitudes [65]. Since the quaternion parameterization has the lowest dimensional possibility for a globally non-singular attitude representation [51, 66], the quaternion is generally used for attitude estimation in the SDINS.

The direction cosine matrix, C_b^n, can be expressed in terms of the quaternion [2, 3] $q = [q_1\, q_2\, q_3\, q_4]^T$ as:

$$C_b^n(q) = \begin{bmatrix} q_1^2 + q_2^2 - q_3^2 - q_4^2 & 2(q_2 q_3 - q_1 q_4) & 2(q_2 q_4 + q_1 q_3) \\ 2(q_2 q_3 + q_1 q_4) & q_1^2 - q_2^2 + q_3^2 - q_4^2 & 2(q_3 q_4 - q_1 q_2) \\ 2(q_2 q_4 - q_1 q_3) & 2(q_3 q_4 + q_1 q_2) & q_1^2 - q_2^2 - q_3^2 + q_4^2 \end{bmatrix} \tag{2.39}$$

Since $q_1^2 + q_2^2 + q_3^2 + q_4^2 = 1$, equation (2.39) can be rewritten as:

$$C_b^n(q) = 2 \times \begin{bmatrix} q_1^2 + q_2^2 - 0.5 & q_2 q_3 - q_1 q_4 & q_2 q_4 + q_1 q_3 \\ q_2 q_3 + q_1 q_4 & q_1^2 + q_3^2 - 0.5 & q_3 q_4 - q_1 q_2 \\ q_2 q_4 - q_1 q_3 & q_3 q_4 + q_1 q_2 & q_1^2 + q_4^2 - 0.5 \end{bmatrix} \tag{2.40}$$

Moreover, a quaternion vector for small angular displacements can be expressed in terms of the direction cosine matrix as follows:

$$
\begin{aligned}
q_1 &= \frac{1}{2}\sqrt{1 + c_{11} + c_{22} + c_{33}} \\
q_2 &= \frac{1}{4q_1}(c_{32} - c_{23}) \\
q_3 &= \frac{1}{4q_1}(c_{13} - c_{31}) \\
q_4 &= \frac{1}{4q_1}(c_{21} - c_{12})
\end{aligned}
\tag{2.41}
$$

The complete algorithm for the computation of quaternion parameters from the transformation matrix can be found in [67].

On the other hand, the angular velocity is related to the quaternion [68], and can be written as:

$$
\begin{aligned}
\omega_x &= 2(-q_2\dot{q}_1 + q_1\dot{q}_2 + q_4\dot{q}_3 - q_3\dot{q}_4) \\
\omega_y &= 2(-q_3\dot{q}_1 - q_4\dot{q}_2 + q_1\dot{q}_3 + q_2\dot{q}_4) \\
\omega_z &= 2(-q_4\dot{q}_1 + q_3\dot{q}_2 - q_2\dot{q}_3 + q_1\dot{q}_4)
\end{aligned}
\tag{2.42}
$$

Rearranging equation (2.42) gives:

$$
\begin{aligned}
\dot{q}_1 &= -\frac{1}{2}\left(q_2\omega_x + q_3\omega_y + q_4\omega_z\right) \\
\dot{q}_2 &= \ \ \frac{1}{2}\left(q_1\omega_x - q_4\omega_y + q_3\omega_z\right) \\
\dot{q}_3 &= \ \ \frac{1}{2}\left(q_4\omega_x + q_1\omega_y - q_2\omega_z\right) \\
\dot{q}_4 &= -\frac{1}{2}\left(q_3\omega_x - q_2\omega_y - q_1\omega_z\right)
\end{aligned}
\tag{2.43}
$$

This set of equations can be represented in two matrix forms:

$$
\dot{q} = \frac{1}{2}\Lambda_{nb}^{n}\, q = \frac{1}{2}Q(q)\begin{bmatrix} 0 \\ \omega_{nb}^{b} \end{bmatrix} \tag{2.44}
$$

where Q(q) is a quaternion matrix representation and Λ_{nb}^{n} is a 4×4 skew symmetric matrix of the angular rate vector. These two matrices are described as follows:

$$\Lambda_{nb}^{n} = \begin{bmatrix} 0 & -[\omega_{nb}^{b}]^{T} \\ \omega_{nb}^{b} & -[\omega_{nb}^{b} \times] \end{bmatrix}$$
$$Q(q) = \begin{bmatrix} q_1 & -q_2 & -q_3 & -q_4 \\ q_2 & q_1 & -q_4 & q_3 \\ q_3 & q_4 & q_1 & -q_2 \\ q_4 & -q_3 & q_2 & q_1 \end{bmatrix} \tag{2.45}$$

where × denotes the cross product operator.

2.2.6 Attitude Compensation

While the angular velocity remains fixed over a computational update interval [2], the quaternion vector update equation [59] may be written as:

$$q_{k+1} = \left[\exp\left(\frac{1}{2}\int_{\mathrm{t_k}}^{\mathrm{t_{k+1}}} \Lambda \,\mathrm{dt}\right)\right] q_k = \exp\left(\frac{\Sigma}{2}\right) q_k$$
$$\Sigma = \begin{bmatrix} 0 & -\sigma^{T} \\ \sigma & -[\sigma \times] \end{bmatrix} and\ \sigma = \int_{\mathrm{t_k}}^{\mathrm{t_{k+1}}} \omega \,\mathrm{dt} \tag{2.46}$$

where σ represents the change in the rotation angle express in navigation frame over the computer cycle t_k to t_{k+1}.

According to existing coning motion, the attitude cannot be computed solely based on the measured angular velocity [69]. The rate of the rotation angle, $\dot{\sigma}$, is expressed as follows:

$$\dot{\sigma} = \omega + \dot{\varepsilon} \tag{2.47}$$

where $\dot{\varepsilon}$ is a component of $\dot{\sigma}$ because of coning motion. By using the Bortz equation [69] and neglecting the higher order terms [51, 70], the following approximation is obtained for equation (2.47):

$$\dot{\sigma} \cong \omega + \frac{1}{2}\sigma \times \omega + \frac{1}{12}\sigma \times (\sigma \times \omega) \cong \omega + \frac{1}{2}\alpha(t) \times \omega$$
$$\alpha(t) = \int_{\mathrm{t_k}}^{\mathrm{t}} \omega \, \mathrm{d}\tau \tag{2.48}$$

2.2.7 Effect of Earth Rotation

Aside from the motion that the tool is experiencing during its operation, the entire system including both the navigation frame and body frame are also rotating simultaneously along the Erath. Since the accelerometers measure the total acceleration resulting from any rotational and translational motion that they are sensing, the effect of Earth rotation must be taken into account and considered in the relative motion analysis.

According to the relative motion equations, the acceleration of point *A* can be expressed in the Earth frame as:

$$\begin{aligned} a_A = a_O + \dot{\omega}_{Earth} \times r_{A/O} + \omega_{Earth} \times \left(\omega_{Earth} \times r_{A/O}\right) \\ +2\omega \times (v_{A/O})_n + (a_{A/O})_n \end{aligned} \tag{2.49}$$

where *O* is the origin of the navigation frame. As the navigation frame is considered to be fixed to the ground, the relative acceleration of the navigation frame with respect to the Earth, a_O, is zero. Moreover, the angular acceleration of the Earth is almost zero [71] because of its constant angular velocity. Since the angular velocity of the Earth is nearly 7.3×10^{-5} rad/s [72] and the relative position and velocity of *A* with respect to the *O* is too small owing to description of on-hand application, the effects of Coriolis and centripetal acceleration in equation (2.49) are too small to be detected by available accelerometers. As a result, the acceleration of point *A* with respect to the Earth reference frame is the same as its acceleration with respect to the navigation frame.

2.2.8 Physiological Hand Tremor

Physiological hand tremor introduces a linear and Gaussian random process to the output of the inertial sensors [73, 74]. Generally, low pass filters (LPF) are added [75] to reduce the errors resulting from noise and physiological hand tremor.

Research studies [73 , 74] show the frequency of this rhythmic and oscillatory motion lies in the range 2.5 Hz to 17 Hz; therefore, the cut-off frequency of 2 Hz is considered for the low pass filters.

In addition, the errors resulting from sensor bias are compensated by employing high pass filters (HPF) [75] with a very low cut-off frequency. A cut-off frequency of 0.5 Hz is chosen as it is consistent with frequencies used by other researchers. For example, Bouten and *et. al.* [76] used 0.1 Hz, Forster and Fahrenberg [77] chose to use 0.5 Hz, and Verburg and Strackee [78] decided to use 0.7 Hz.

In this research, a band pass filter is designed with cascading a high pass filter and low pass filter. For each sensor, a second order Butterworth high pass filter and second order Butterworth low pass filter are cascaded with a cut-off frequency of 0.5 Hz and 2 Hz, respectively. Selecting the order of a filter is a compromise between the resulted overshooting and settling time.

The entire correction process before the strapdown computing task is represented in Figure 9.

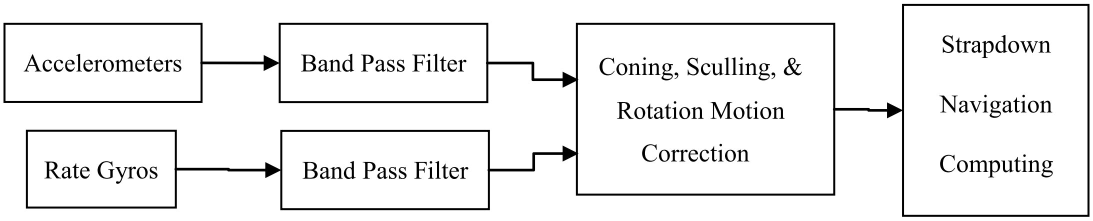

Figure 9 - Sensor's output correction block diagram

2.2.9 State-Space of the System

Finally, the general equations of the SDINS for the hand-held tool application can be written from equations (2.31) and (2.44):

$$
\begin{aligned}
\dot{r}^n &= v^n \\
\dot{v}^n &= C_b^n(f_A - a_t - a_n) + g_n \\
\dot{q} &= \frac{1}{2}\Lambda_{nb}^n q = \frac{1}{2}Q(q)\begin{bmatrix} 0 \\ \omega_{nb}^b \end{bmatrix}
\end{aligned}
\tag{2.50}
$$

where r^n and v^n denote the position and velocity of the tool tip with respect to the navigation frame.

2.3 Experimental Result

In this research, a 3DX-GX1 IMU from the Microstrain was used, which included three rate gyros and three accelerometers with a sampling rate of 100 Hz and a noise density of $3.5\,°/\sqrt{hour}$ and $0.4\,mg/(rms\,\sqrt{Hz})$, respectively [79]. Detailed specifications are found in Appendix A.

2.3.1 IMU Calibration

Microstrain Company has performed the calibration procedure for 3DX-GX1 IMU. This IMU is calibrated for the scale factor, bias, misalignment, and even gyro G-sensitivity. In addition, the performance of 3DX-GX1 is improved by full temperature compensation.

According to 3DX-GX1 documentation [79], the calibration parameters such as sensor gain and bias are changed with temperature. Therefore, the calibration parameters must be calibrated with respect to the operating temperature. Figure 10 through Figure 13 show the effect of temperature compensation on the stability of the sensor gain and bias over the range of -20°C to 60°C. As shown in these figures, the changes in the sensor gain and bias are considerable even the temperature is changing in the small range. These results illustrated the importance of the parameter calibration with respect to the temperature when it is hard to control the temperature of the environment that the inertial sensors are operating.

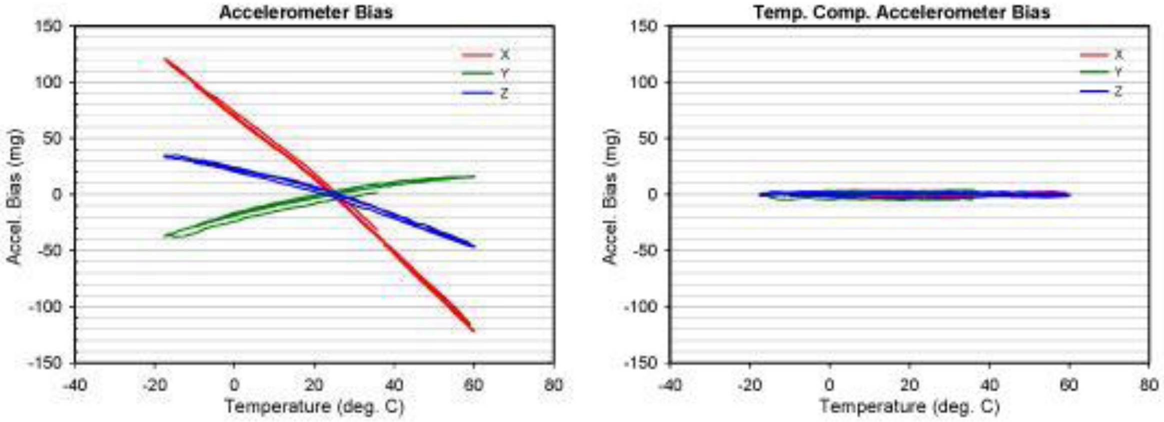

Figure 10 - Accelerometer bias without and with temperature compensation [8079]

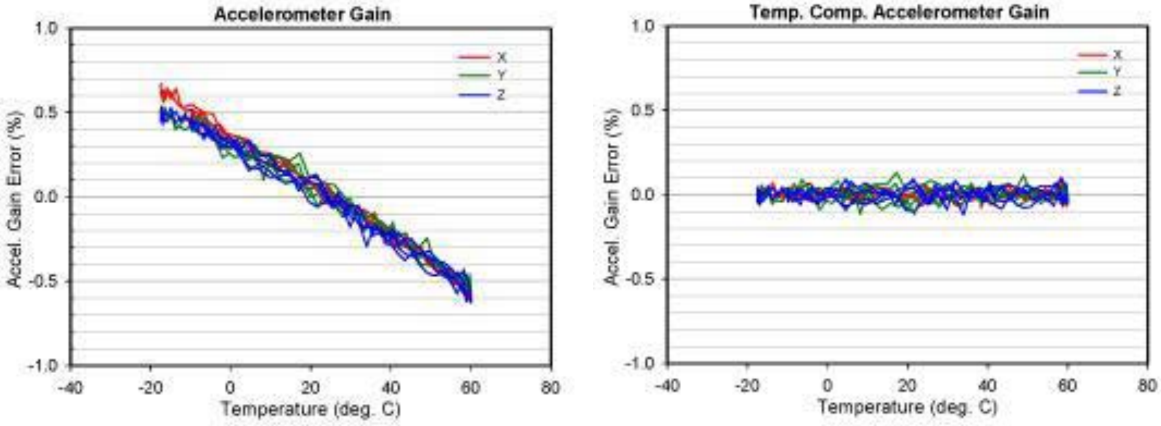

Figure 11 - Accelerometer gain without and with temperature compensation [79]

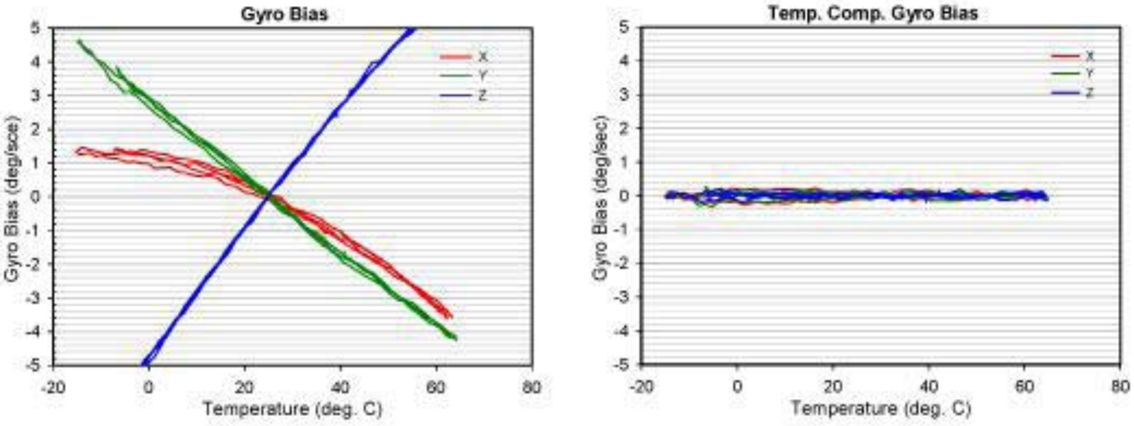

Figure 12 - Gyro bias without and with temperature compensation [79]

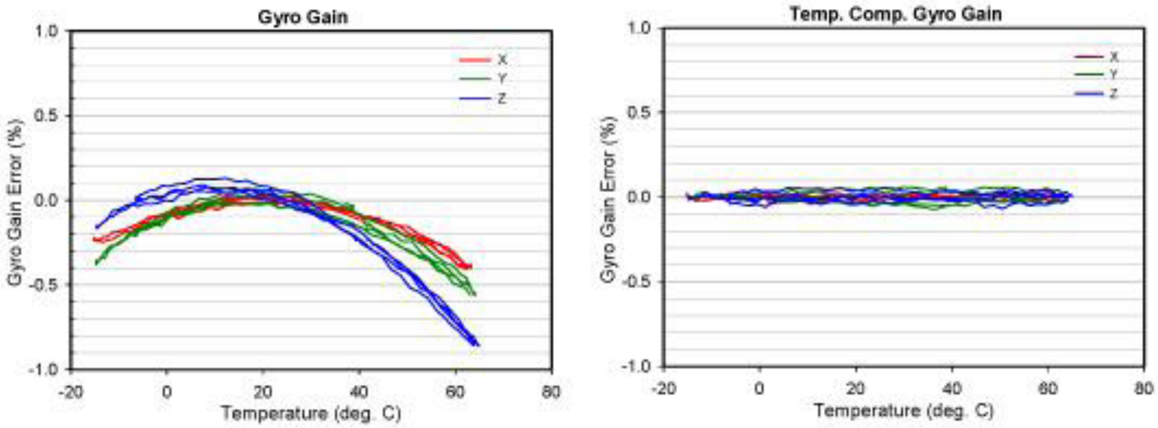

Figure 13 - Gyro gain without and with temperature compensation [79]

2.3.2 Noise and Physiological Hand Tremor Compensation

The inherent noise of sensors and the noise introduced by the hand tremor must be removed by means of a low pass filter. Figure 14 and Figure 15 show the denoised output versus the actual output, while the tool is moving on the 2D plane has and experiencing both rotational and translational motion. As a result of the low pass filtering, the noise is greatly diminished and smoother signal are resulted; consequently, it is expected that the SDINS drift resulting form the noise is reduced.

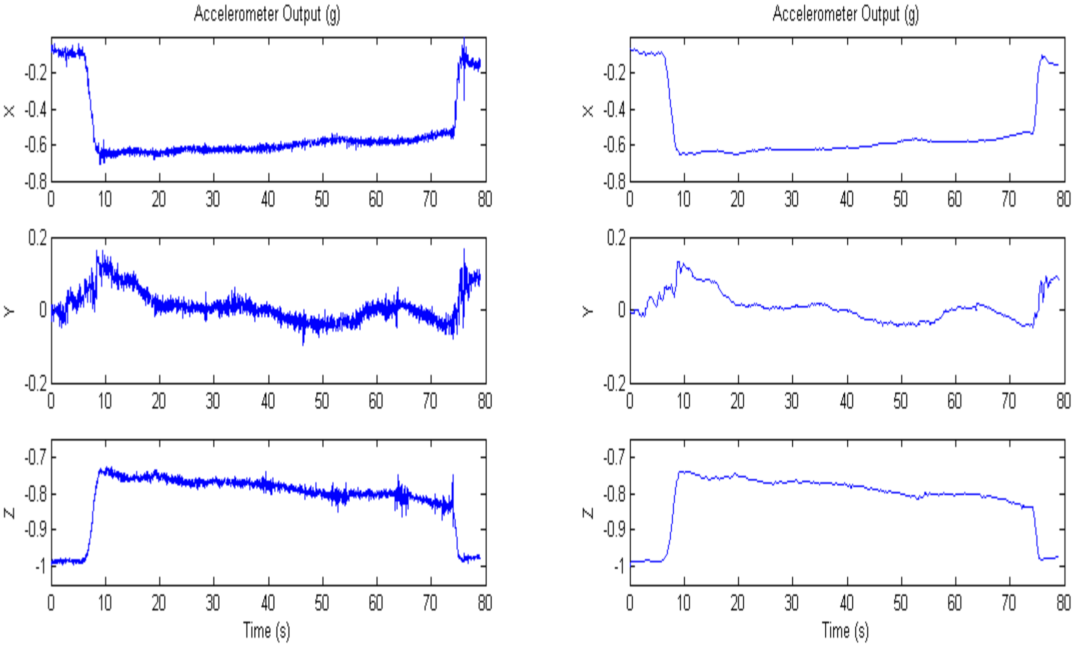

Figure 14 - The output of accelerometers: measured (left) denoised (right)

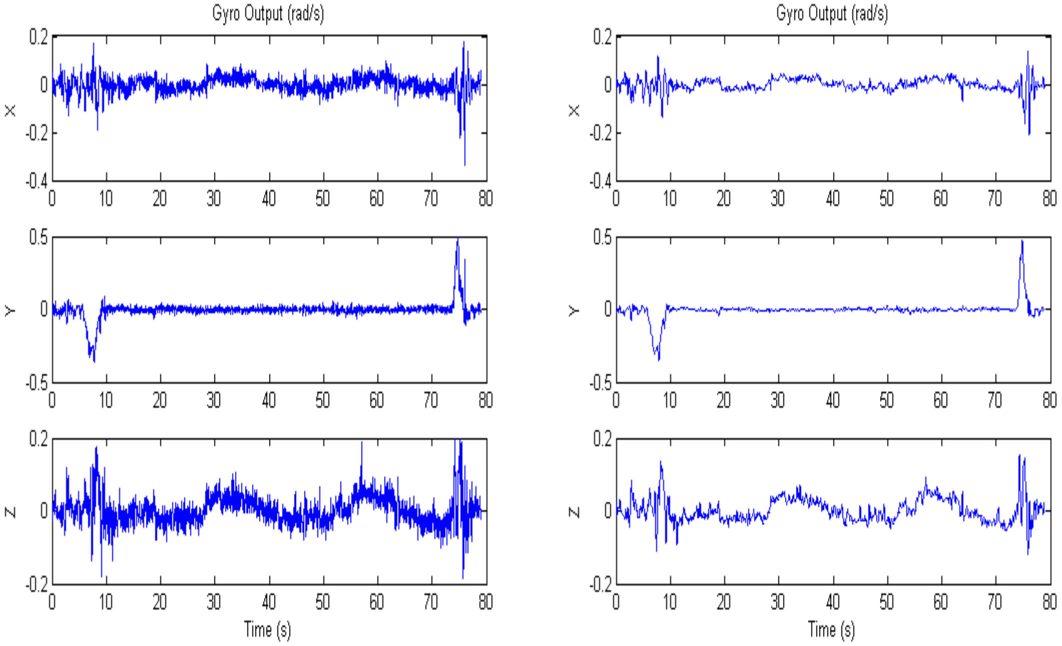

Figure 15 - The output of gyros: measured (left) denoised (right)

2.3.3 Compensation for the Common Motion-Dependent Errors

While the tool is experiencing only the rotational motion and the tool tip is fixed at the initial position, it is expected that the absolute acceleration of the tool tip will be zero. By assuming zero acceleration for the tool tip in the equation (2.28), the output of the accelerometers must be equal to the acceleration resulting from sculling and coning motion.

Figure 16 and Figure 17 show the effect of the rotational motion around x- and y- axis on all accelerometers, while Figure 18 and Figure 19 represent the error of the estimated acceleration of the tool tip in x, y, and z axes in the body frame; however, it is assumed to be zero. The error is a result of the remaining noise and bias in the inertial sensors measurements and the error in the attitude estimation which involves in the evaluation of the Euler angles. As shown, the magnitude of the error is less than 5 mg in all directions, and it can be neglected in the strapdown navigation computing task.

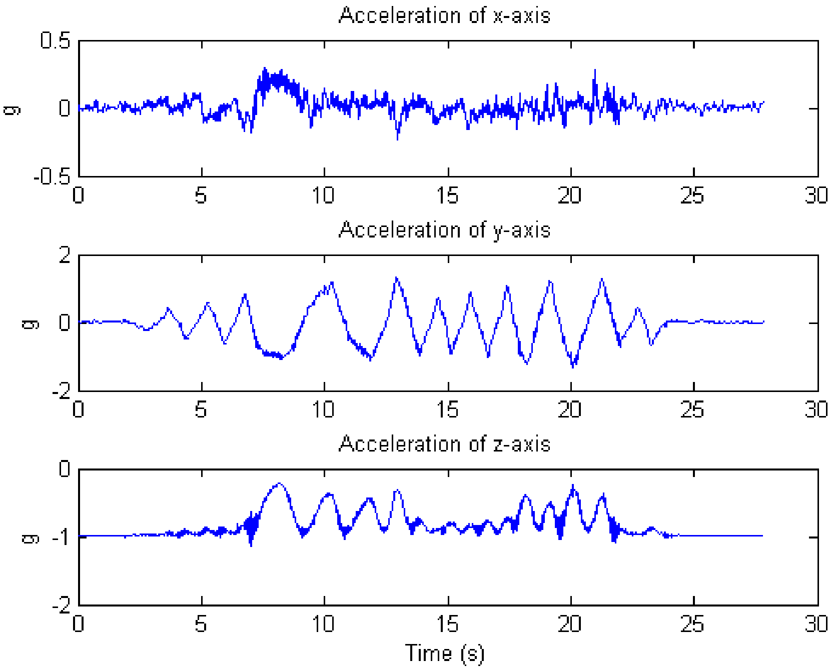

Figure 16 - Accelerometers outputs while the tool is experiencing the rotational motion around x-axis

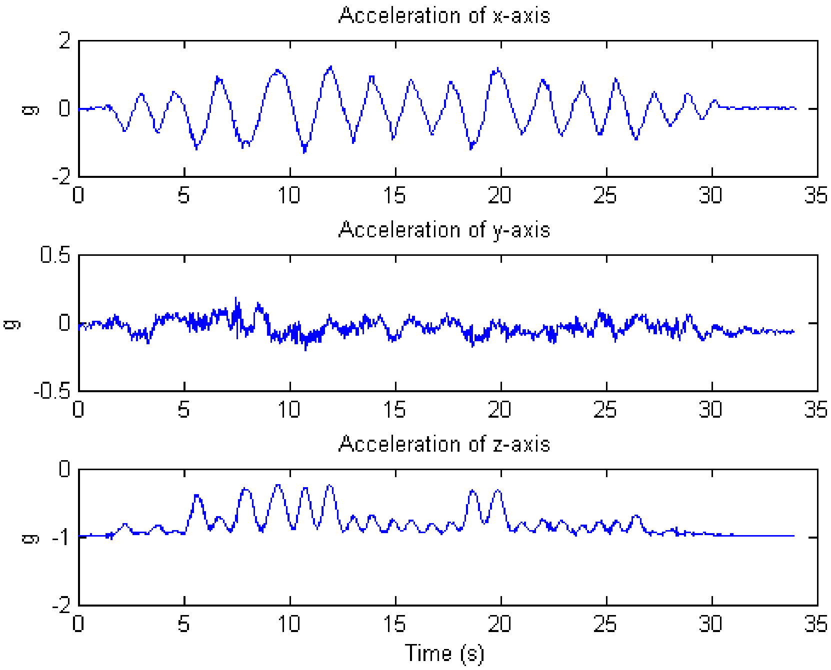

Figure 17 - Accelerometers outputs while the tool is experiencing the rotational motion around y-axis

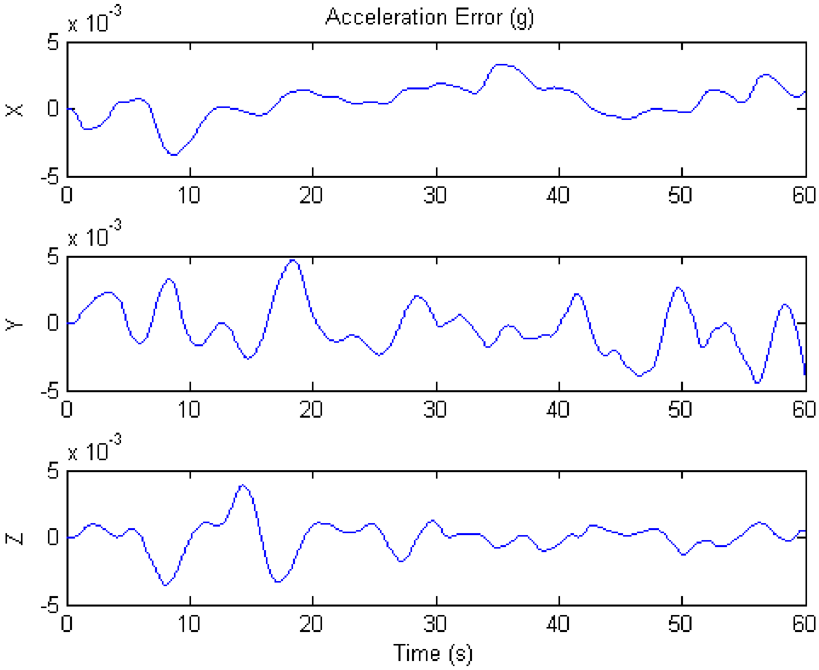

Figure 18 - Acceleration error when the tool rotating around x-axis

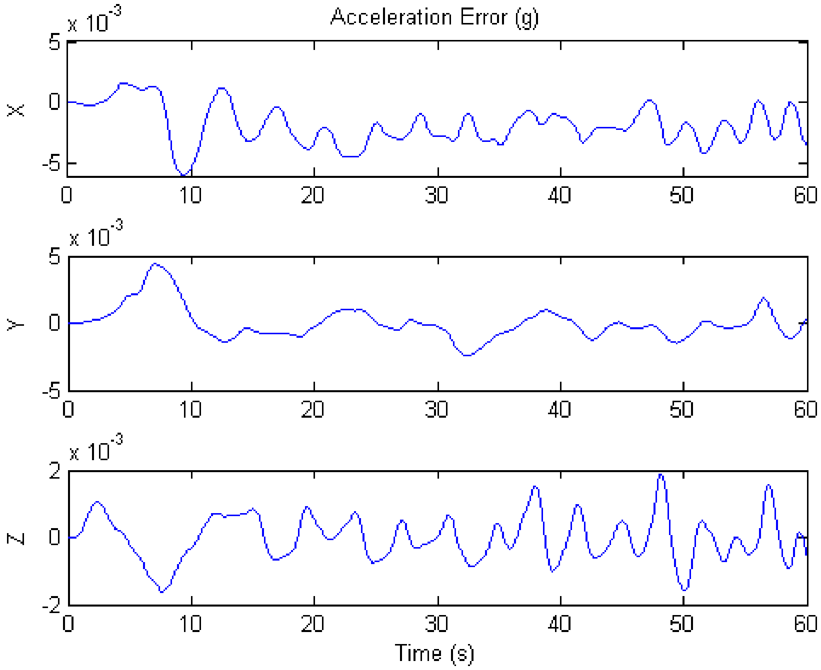

Figure 19 - Acceleration error when the tool rotating around y-axis

2.3.4 Acceleration Computation

When the hand-held tool is moving on a 2D plane and experiencing both translational and rotational motion, the residue in equation (2.28) estimates the linear acceleration of the tool tip. The total acceleration resulting from both the coning motion and the sculling/rotation motion expressed in the body frame is estimated from equation (2.27), and then compared with the acceleration measured by accelerometers, see Figure 20 through Figure 22.

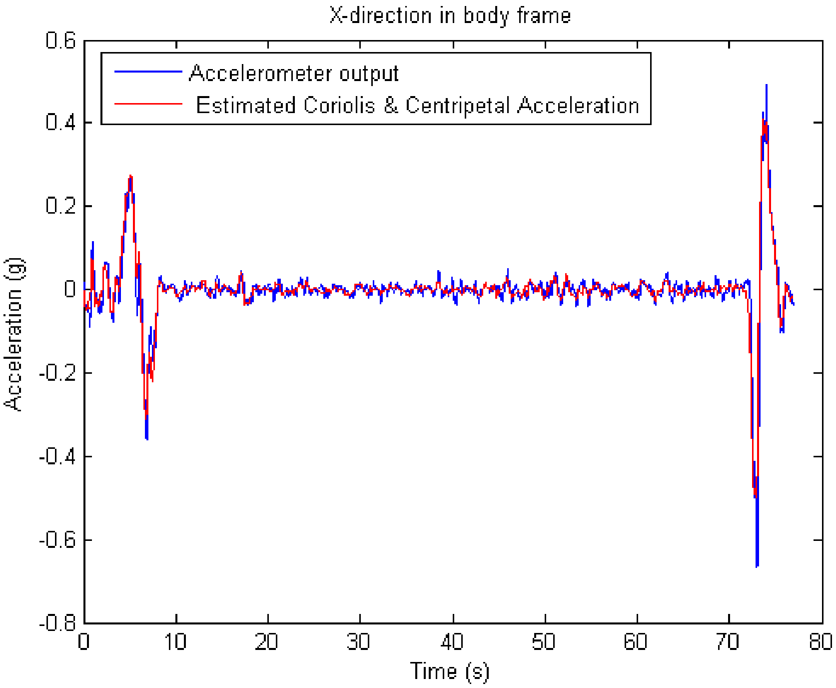

Figure 20 - Estimated acceleration vs. measured acceleration in x axis

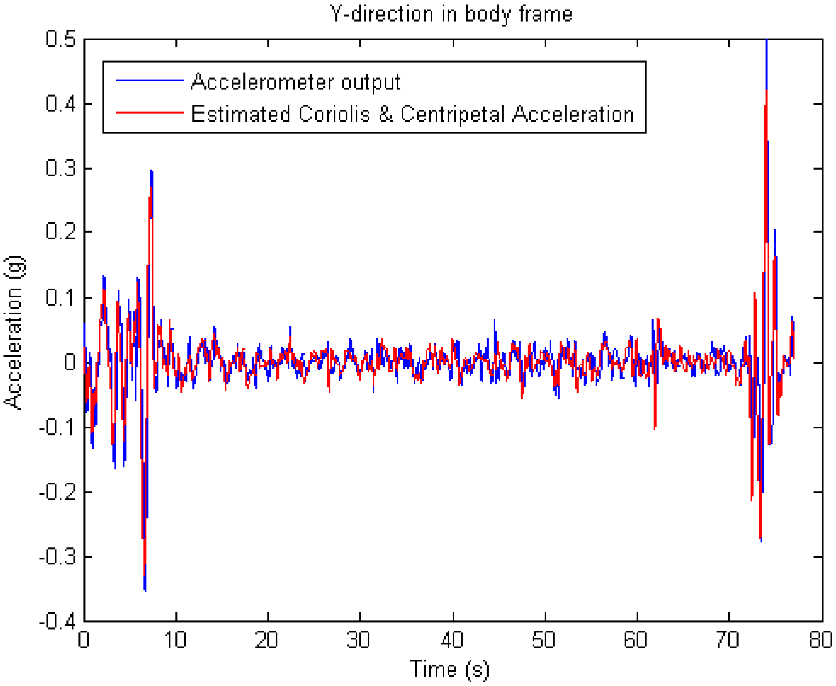

Figure 21 - Estimated acceleration vs. measured acceleration in y axis

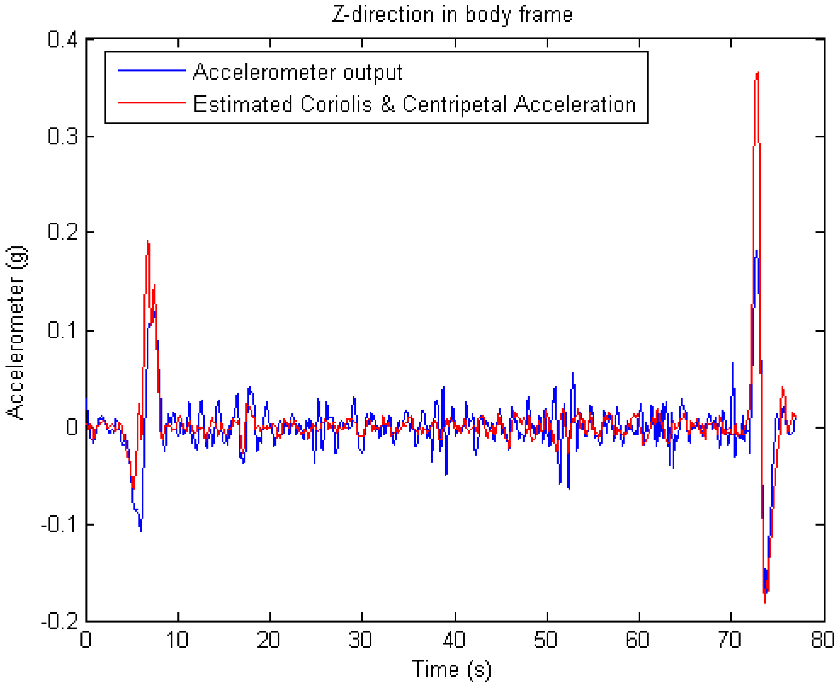

Figure 22 - Estimated acceleration vs. measured acceleration in z axis

The total linear acceleration of the tool tip along x, y, and z axes resulting from both the translational of the hand-held tool on a XY plane is shown in Figure 23. Since the tool tip is not experiencing any translational motion along the direction of z-axis, its linear acceleration is supposed to be zero; however, the estimated linear acceleration in z-axis is about 5 mg. This error is nut unexpected, since the results in section 2.3.3 shows that the linear acceleration error is less than 5 mg, when there is no translational motion in each direction.

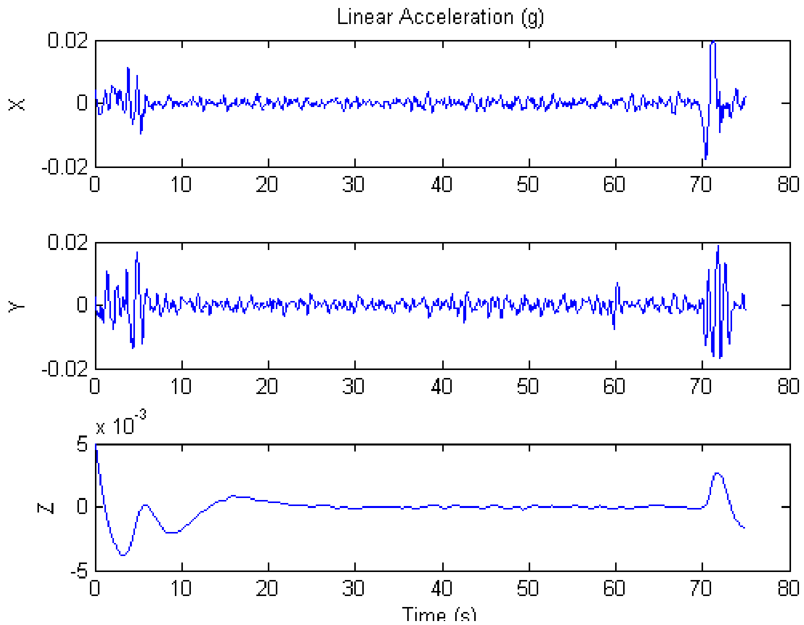

Figure 23 - Linear acceleration in x, y, and z axes

2.3.5 Attitude Computation

While the hand-held tool is moving on a 2D plane and experiencing both translational and rotational motion, the attitude of the tool can be estimated by equations (2.46) and (2.48). The computed heading compared with the actual attitude measured by magnetometers is shown in Figure 24, and the error of estimated orientation is represented in Figure 25. However, the error in quaternion format is less than 0.05, but the corresponding error in the Euler angle domain is about 8 degrees, see Figure 26.

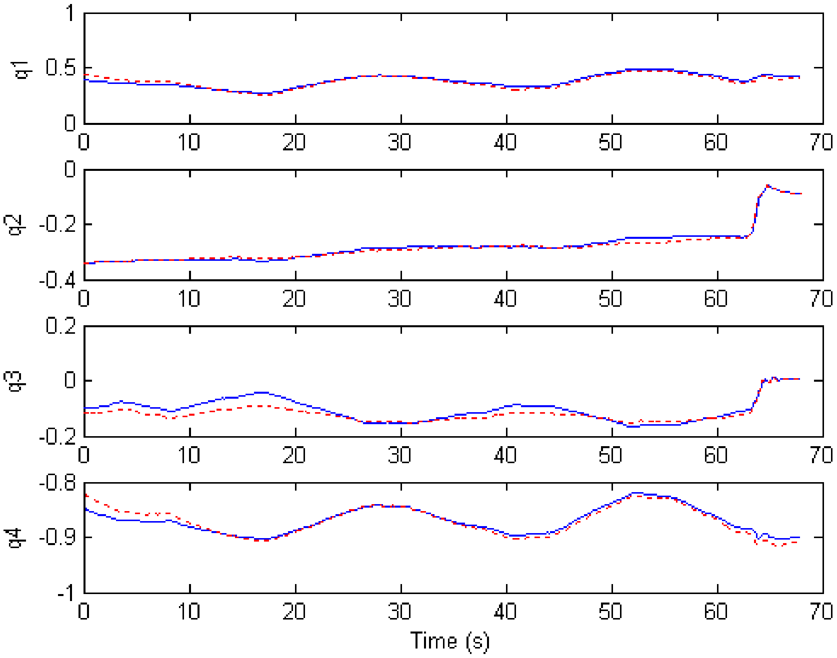

Figure 24 - Quaternion: estimated (solid) vs. true (doted)

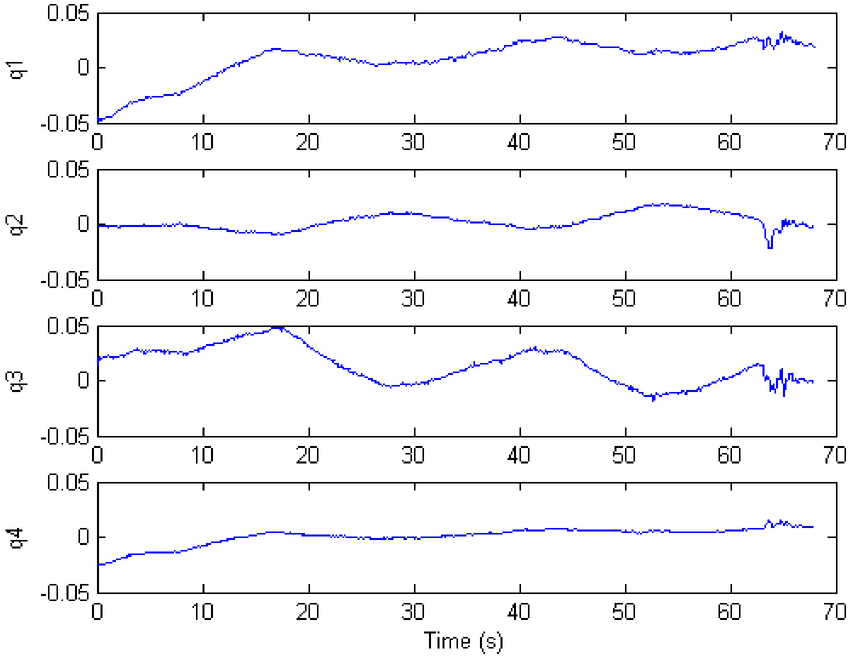

Figure 25 - Quaternion error

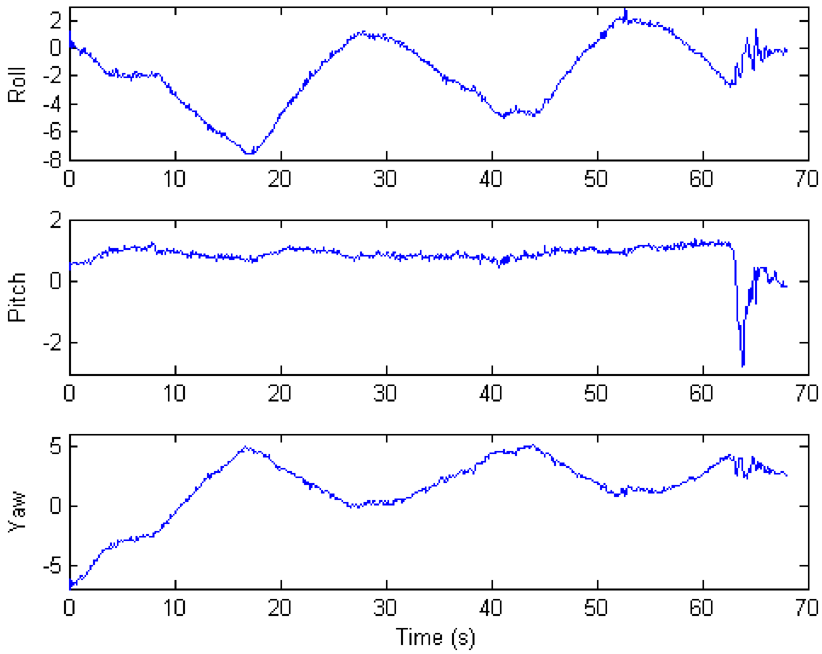

Figure 26 - Euler angles error

2.4 Summary

This chapter presents an algorithm for reducing the effect of the common motion-dependent errors in SDINS for a hand-held tool tracking system. The drift resulting from accelerometer bias is reduced by applying a high-pass filter, while the error produced by the sensor noise and the tool vibration is diminished by employing a low-pass filter. The common motion-dependent errors including rotational and coning motion are taken into account not only in the calculation of the effective acceleration but also in the computation of the attitude. The effects of the common motion-dependent errors are reduced considerably, but the remaining attitude error is still great enough to cause a drift in position estimation.

Chapter 3

Local Positioning System

The Local Positioning System (LPS) is a reliable and cost-effective tracking system for indoor applications, designed to localize a moving object by estimating its three-dimensional position in real-time. The LPS provides a small centralized version of the Global Positioning System (GPS) for indoor environments, since the satellite signals are blocked easily by construction materials of buildings.

Over the last few decades, the real-time video tracking systems have been used for a wide range of applications such as robotics [35, 36], medicine [38], security [39], and even interactive games [80, 81]. Automated video analysis has been made possible by the easy access to high-powered computers and high-quality but inexpensive video cameras.

In computer vision, object tracking refers to the detection of a desired object in each single frame of sequential frames and the estimation of its trajectory as it moves around the scene. Video tracking can be a complex and time-consuming process because of the noise in images, complex motion, partial or full object occlusions, and loss of information because of projection of the 3D world on a 2D image.

Video tracking includes mounting the cameras around the workspace, calibrating the cameras, capturing images, applying image processing algorithms and features extraction for every single frame from each camera, and estimating the 3D position from 2D images.

In this chapter, the proposed multi-camera vision system, which includes four common CCD cameras, is described with a new configuration set up and calibration procedure. In addition, the required image processing techniques and feature extraction method is discussed.

3.1 Multi-Camera Vision System

The multi-camera systems generally include two or three digital cameras, while the positions of their lens are placed in a straight line. However, the calibration procedure for the cameras is easier and more accurate than it would otherwise be; the total field of view of the system is limited. A multi-camera vision system is proposed which includes at least four common CCD cameras when their lenses are placed on an arc line.

Because each tracking point is visible for two or more cameras, the average value of the estimated positions by triangulation between each two adjacent cameras is used so as to obtain a more accurate positioning and reduce the uncertainty.

3.1.1 Configuration

A multi-camera vision system with a unique configuration is recommended as being a reliable and cost-effective vision system. A specific configuration for mounting the multi-camera vision system is proposed so as to prevent the loss of line of sight as much as possible. The number of cameras, the position of the cameras with respect to each other, and the position and orientation of the cameras with respect to the center of the navigation frame are the crucial characteristics in this configuration set up.

It is proposed that all cameras are located in a semicircle, as shown in Figure 27 for a four-camera vision system. In addition, the distance between each two adjacent lenses is the same as for the others and depends on the radius of the semicircle.

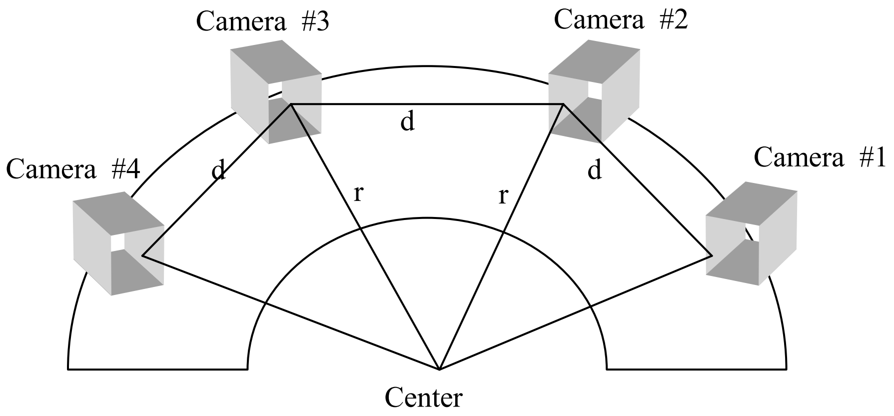

Figure 27 - Cameras configuration set up

According to Figure 27, the distance between each two cameras is calculated as follows:

$$d = 2\, r \tan\left(\frac{\pi}{8}\right) \tag{3.1}$$

Moreover, the tilt of the lenses toward the center and the length of the radius of semicircle depend on the angle of view of each camera, the height of the cameras from the workspace, and the width of the desired workspace.

As a result of this arrangement, a wide circular field of view is initiated with less loss of line-of-sight. Figure 28 and Figure 29 show the field of view of the proposed multi camera vision systems with a straight line and a semicircle configuration.

As shown in Figure 28, if the angle of view of each camera is α, the angle of view of the multi-camera vision system with the straight line configuration is still equal to α with a forward-facing field of view. However, the proposed multi-camera vision system initiates the wider angle of view which is equal to $(\pi - \pi/8)$. In addition, a circular field of view is provided with this configuration as illustrated in Figure 29.

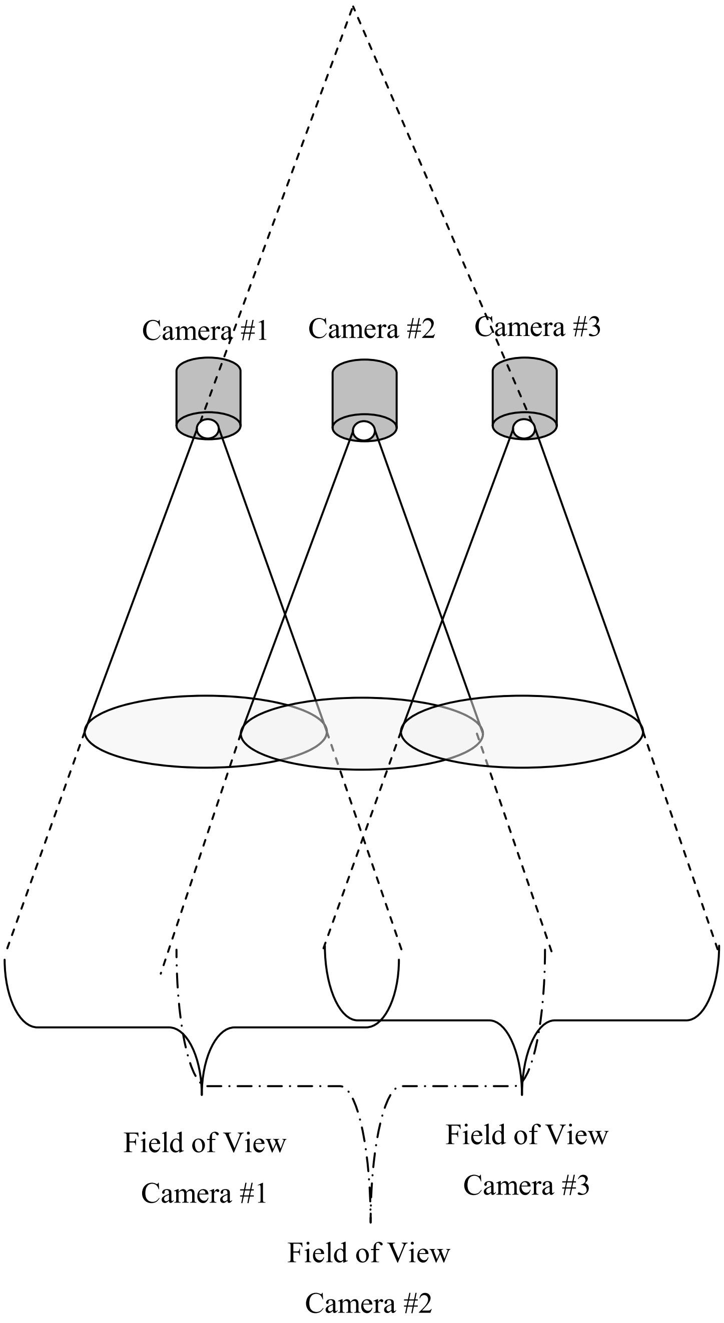

Figure 28 - The field of view of a multi-camera vision system when the lenses of its cameras are placed on a straight line

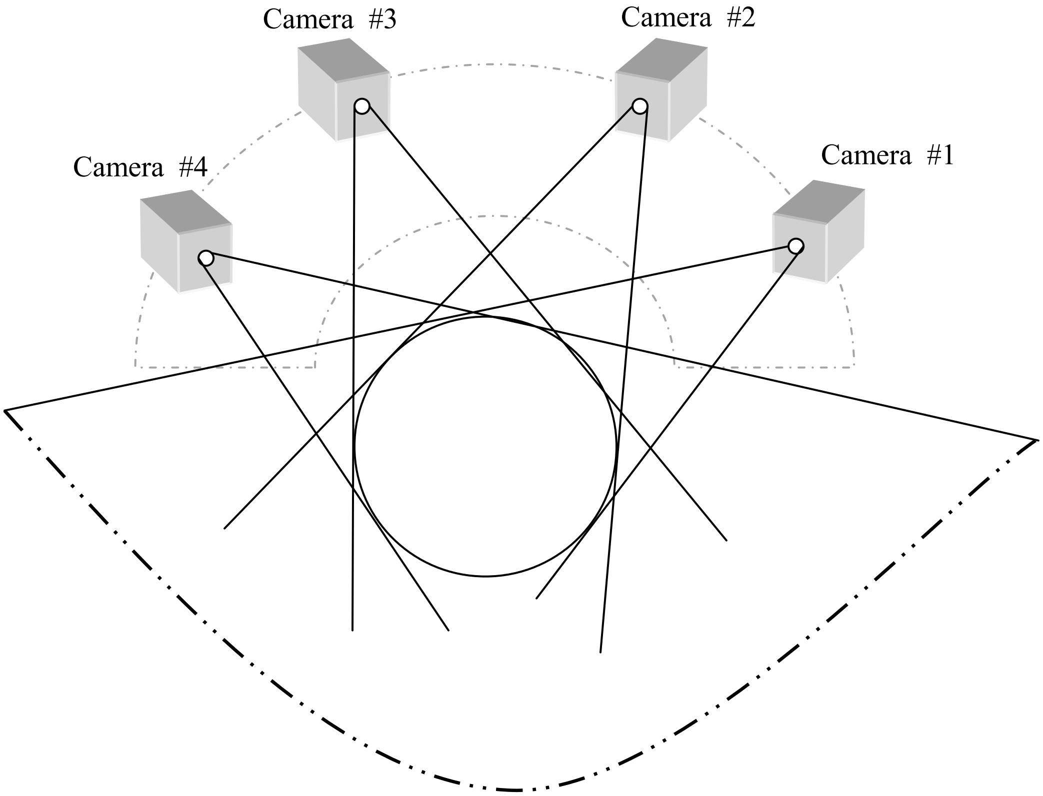

Figure 29 - The field of view of the proposed multi-camera vision system

3.1.2 Camera Modeling

In order to find the Cartesian mapping grid for transforming 2D positions in the cameras' image plane to the corresponding 3D position in the navigation frame, the single camera calibration for each camera and the stereo camera calibration for each two adjacent cameras are required.

Performing the single and stereo camera calibrations requires the camera model which provides the relationship between the physical camera parameters and projected point into the camera display. A perspective projection model of an ideal camera is shown in Figure 30.

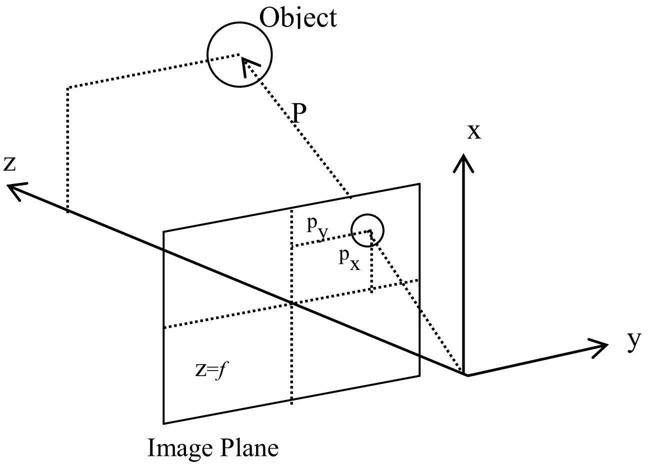

Figure 30 - Ideal camera imaging model

In this model, the image plane is located at the focal length of the lens on the optical axis z parallel with the x-y plane of the camera frame [82]. Each point of an object in the navigation frame, $P = [x\ y\ z]^T$, is projected to the corresponding point *p*:

$$p = \begin{bmatrix} p_x \\ p_y \end{bmatrix} = \begin{bmatrix} kfs_u \dfrac{x}{z} \\ lf \dfrac{y}{z} \end{bmatrix} + \begin{bmatrix} N_x \\ N_y \end{bmatrix} \tag{3.2}$$

where *f* is the focal length of the camera lens, $\frac{1}{k}$ and $\frac{1}{l}$ denote the dimension of a pixel on the image plane, s_u represents the image scale factor [83], and the vector *N* is a zero-mean Gaussian random measurement noise.

In a real digital camera, because of the lens distortion, the location of point *p* is not located exactly on the projected line [84, 85]. As shown in Figure 31, two tangential and radial distortions relocate the position of the projected point.

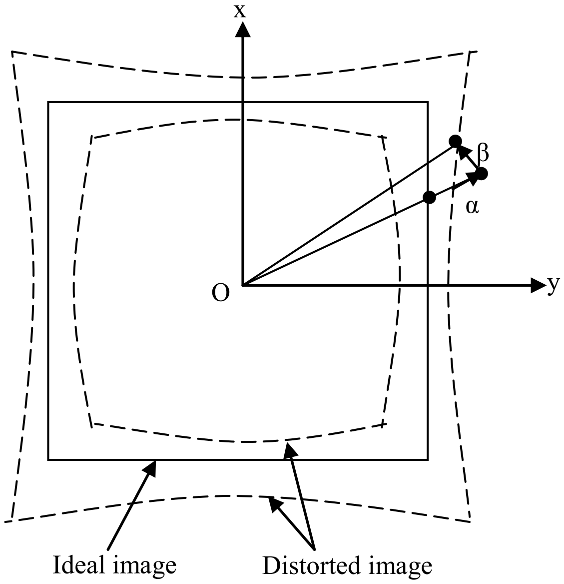

Figure 31 - Radial and tangential distortion

The direction of the radial distortion is inward or outward of the center of image plane and along the line connecting the projected point to the principal point *O*, while the direction of the tangential distortion is perpendicular to the radial distortion [84]. The total relocation for each point is directly related to its distance from the principal point, $d^2 = \left(\frac{x}{z}\right)^2 + \left(\frac{y}{z}\right)^2$, and distortion parameters of the lens [86, 87]:

$$d_r = (1 + \alpha_x d^2 + \alpha_y d^4) \tag{3.3}$$

$$d_t = \begin{bmatrix} d_{t,x} \\ d_{t,y} \end{bmatrix} = \begin{bmatrix} 2\beta_x \frac{x}{z}\frac{y}{z} + \beta_y \left(d^2 + 2\left(\frac{x}{z}\right)^2\right) \\ \beta_x \left(d^2 + 2\left(\frac{y}{z}\right)^2\right) + 2\beta_y \frac{x}{z}\frac{y}{z} \end{bmatrix}$$

where d_r and d_t denote the radial and tangential displacements of a point; *d* represents the distance from the center of the image plane; and α_x, α_y, β_x, and β_y are the distortion parameters of the lens in both directions x and y.

In addition to the distortion, because of minor manufacturing defects, the vision sensor pixels may be skewed, while the angle of the x and y pixel axes are not exactly perpendicular [83]. Taking into account the effect of the distortions and skewed pixels, the following model applies:

$$p = f d_r \begin{bmatrix} k s_u \dfrac{x}{z} + k s_u \gamma \left(\dfrac{y}{z} + d_{t,y}\right) \\ l \dfrac{y}{z} \end{bmatrix} + \begin{bmatrix} d_{t,x} \\ d_{t,y} \end{bmatrix} + \begin{bmatrix} N_x \\ N_y \end{bmatrix} \tag{3.4}$$

where γ is the skew coefficient and equal to zero when the angle of the x and y pixel axes is exactly 90 degree.

Furthermore, the actual origin of the camera coordinate system is at the upper-left corner of the image plane and not at its center. This adds the coordinate of principal points [88] into equation (3.4). The principal point refers to the intersection of the optical axis with the image plane. The center of the image plane matrix usually does not coincide with the principal point.

$$p = f d_r \begin{bmatrix} k s_u \dfrac{x}{z} + k s_u \gamma \left(\dfrac{y}{z} + d_{t,y}\right) \\ l \dfrac{y}{z} \end{bmatrix} + \begin{bmatrix} C_x \\ C_y \end{bmatrix} + \begin{bmatrix} d_{t,x} \\ d_{t,y} \end{bmatrix} + \begin{bmatrix} N_x \\ N_y \end{bmatrix} \tag{3.5}$$

3.1.3 Single Camera Calibration

The single camera calibration refers to the estimation of geometric camera parameters. According to the camera model obtained in equation (3.5), the geometric parameters *f*, s_u, *C*, α, β, and γ can be estimated by capturing enough images while the coordinate of both points *P* and *p* are known in calibration grids.

The calibration grids are obtained by capturing a set of images from an identical checkerboard [89] in various poses in the field of view of the camera. In the calibration process, the number and the size of the checkerboard grids are essential. Usually, a 9×8 or 8×7 checkerboard with 5 cm×5 cm or 3 cm×3 cm squares, shown in Figure 32, is used for the calibration procedure.

Figure 32 - Checkerboard with 5 cm×5 cm squares

During the single calibration, an arbitrary coordinate is assigned with respect to the sequence of the grid corner selection. In each image, the first selected corner grid is assumed to be the origin of the coordinate system. Subsequently, the x and y axes are considered in the next grid selection, and then the z-axis is chosen perpendicular to the checkerboard plane whose direction is chosen with respect to the right hand rule. Once the coordinate system is assigned to the image, the rotation matrix and translation vector are obtained to convert this coordinate system to the camera frame. As a result, the coordinate of point *P* and its 2D projection, point *p*, are known. If equation (3.5) is rearranged as:

$$p = \frac{1}{z}\begin{bmatrix} f d_r k s_u & k s_u \gamma & d_{t,x} + k s_u \gamma d_{t,y} + C_x \\ 0 & f d_r l & d_{t,y} + C_y \\ 0 & 0 & 1 \end{bmatrix}\begin{bmatrix} x \\ y \\ 1 \end{bmatrix} + \begin{bmatrix} N_x \\ N_y \end{bmatrix} = \frac{1}{z} M P + N \tag{3.6}$$

then matrix *M* can be estimated by applying the least square parameter estimation method [90, 91].

In case where the world coordinate system is distinct from the camera frame, each point in the camera frame can be transformed to the world coordinate system by the homogenous transfer matrix:

$$P^C = \begin{bmatrix} R_C^W & T \\ 0 & 1 \end{bmatrix}\begin{bmatrix} P^W \\ 1 \end{bmatrix} \tag{3.7}$$

By substituting equation (3.7) into equation (3.6):

$$p = \frac{1}{z} M \begin{bmatrix} R_C^W & T \\ 0 & 1 \end{bmatrix} \begin{bmatrix} P^W \\ 1 \end{bmatrix} + N = \frac{1}{z} \mathcal{M} P + N \tag{3.8}$$

where matrix $\mathcal{M}$ includes intrinsic and extrinsic parameters; and then, the geometric parameter of the camera can be obtained by estimating matrix $\mathcal{M}$.

3.1.4 Stereo Camera Calibration

Since the 3D position of each tracking point with respect to the navigation frame is desirable, aside from the single camera calibration, the stereo camera calibration [92] for each two adjacent cameras should be performed to make three-dimensional vision possible.

The stereo camera calibration refers to a procedure that provides the extrinsic parameters of two adjacent cameras relative to each other. This procedure allows us to calculate depth by using triangulation algorithm. Performing stereo camera calibration requires a set of images captured by two neighboring cameras simultaneously. Going through the corner extraction process, the same set of points must be selected in both the left and right image of the same scene. In addition, this is crucial that the same grid must be selected as being the origin point for both images. This means the identical pattern must be chosen for selecting the corner grids for all pair of images.

As a result of the stereo calibration, the homogenous transfer matrix is obtained, which transforms each point in the right camera frame into the left camera frame and allows computing the 3D position of each point in the image plane expressed in the both right and left camera frame.

3.1.5 Defining the World Coordinate System

Finding the 3D position of the tool tip with respect to the navigation frame requires that a unique world coordinate system is considered for all cameras.

According to the single camera calibration procedure, a unique world coordinate system can be considered for all four cameras as shown in Figure 33. This world coordinate system is also aligned on the navigation frame which is defined in the SDINS.

First, all four cameras capture the image of the checkerboard simultaneously. Then a unique corner of checkerboard in four images is chosen as the origin of the world coordinate system. Since the direction of the x, y, and z axes are obtained with respect to the next grids selection, the next grids must be selected in the same pattern in four images. Once the calibration procedure is performed for all cameras, the homogenous transfer matrix is available to convert each point from each camera frame to the world coordinate system.

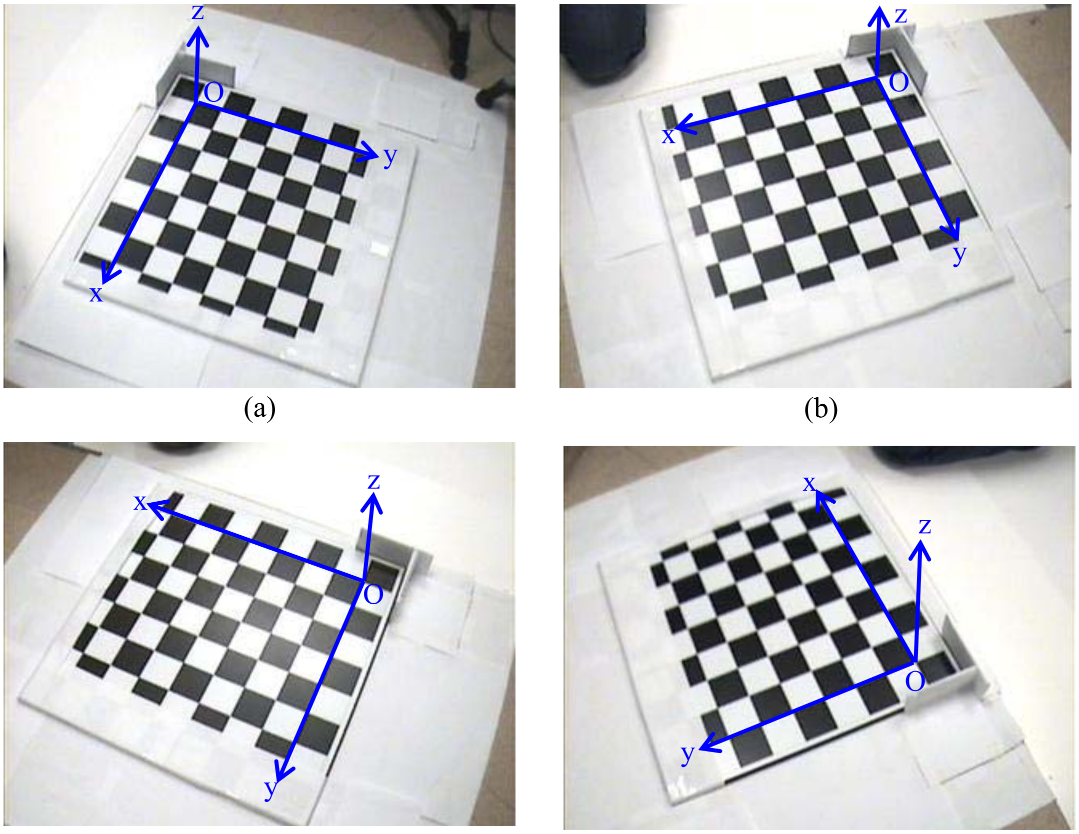

(a) (b)

(c) (d)

Figure 33 - The world coordinate system in the view of:
(a) camera #1 (b) camera #2 (c) camera #3 (d) camera #4

3.2 Digital Image Processing

Digital image processing techniques are the two-dimensional digital signal processing which are designed to enhance the quality of an image, restore information from a distorted image, and extract required information.

Digital image processing techniques, as a fundamental part of the image analysis, are applied in a wide category of images – such as space images, satellite images, medical images, and optical camera images – for classification, recognition, diagnosis, prediction, and object tracking in the field of the computer vision.

3.2.1 Image Enhancement

Image enhancement refers to the process of enhancing the quality of image features such as edges, boundaries, and contrast. Typically, noise reduction and edge enhancement operators are applied into images to remove the isolated noise and sharpen the boundaries, respectively.

The denoising and sharpening operations can be performed in the spatial domain or frequency domain by filtering. Image filtering is usually used to deal with the restoration of degradation [93].

Spatial operations are designed to enhance the image based on local neighboring pixels [94]. The common spatial noise reduction and smoothing operators are spatial averaging, spatial low pass filtering, and median filtering. Each of these operators introduces a masking window, when the window defines the weight of enhancing pixel and its neighboring pixels in the spatial domain. In the spatial averaging, the weights of all pixels are the same and equal to 1/N, where N is the number of pixels in the window. The usual size of the window is 3×3, 5×5, or 7×7, shown in Figure 34. In the low pass filtering, the weights are chosen such that their summation is 1 and the weights are spread in the window symmetrically. The 5-point weighted low pass filter is show in Figure 34. In the median filtering, the pixel is replaced by the median of the pixels in the masking window.

$$\begin{bmatrix} \frac{1}{9} & \frac{1}{9} & \frac{1}{9} \\ \frac{1}{9} & \frac{1}{9} & \frac{1}{9} \\ \frac{1}{9} & \frac{1}{9} & \frac{1}{9} \end{bmatrix} \qquad \begin{bmatrix} 0 & \frac{1}{8} & 0 \\ \frac{1}{8} & \frac{1}{4} & \frac{1}{8} \\ 0 & \frac{1}{8} & 0 \end{bmatrix}$$

(a) (b)

Figure 34 - Spatial averaging window mask: (a) 3×3 window (b) 5-point weighted low-pass filter

The original image is blurred by applying the noise reduction and smoothing operators. The *unsharp* masking operation is generally used to sharpen the edges. This operation can be represented as:

$$v(m,n) = u(m,n) + \lambda g(m,n) \tag{3.9}$$

where $u(m,n)$, $v(m,n)$, and $g(m,n)$ are the original, *unsharp* masked, and gradient image, respectively; and λ is chosen to be greater than zero. The gradient is a discrete Laplacian operator:

$$g(m,n) = u(m,n) - \frac{1}{4}[u(m-1,n) + u(m,n-1) + u(m+1,n) + u(m,n+1)] \tag{3.10}$$

Besides the spatial domain, denoising and sharpening can be performed in the frequency domain. Digital Fourier transform (DFT) or Discrete Wavelet transform (DWT) of an image is the representation of the image in the frequency domain. Accordingly, various filters have been designed to apply into the image in this domain. Displaying the resulting image in the spatial domain requires inverse transformation of DFT or DWT. Studies show that the result of image filtering in the frequency domain is more precise than it is in the spatial domain [95].

3.2.2 Edge Detection

The very first step of features extraction and segmentation is edge detection. Edges can be considered the pixels that their luminous intensity or gray-level changes sharply with respect to their neighboring pixels.

Edges can be localized by finding maximum local in the image derivatives [96]. Gradient and Laplace operators are designed based on computing the first- and second-order derivatives of the image. These operators include a mask or pair of masks, shown in Figure 35.

$$\begin{bmatrix} -1 & 0 & 1 \\ -2 & 0 & 2 \\ -1 & 0 & 1 \end{bmatrix} \quad \begin{bmatrix} -1 & -2 & -1 \\ 0 & 0 & 0 \\ 1 & 2 & 1 \end{bmatrix} \qquad \begin{bmatrix} -1 & 0 & 1 \\ -1 & 0 & 1 \\ -1 & 0 & 1 \end{bmatrix} \quad \begin{bmatrix} -1 & -1 & -1 \\ 0 & 0 & 0 \\ 1 & 1 & 1 \end{bmatrix}$$

(a) Sobel (b) Prewitt

$$\begin{bmatrix} 0 & -1 & 0 \\ -1 & 4 & -1 \\ 0 & -1 & 0 \end{bmatrix} \qquad \begin{bmatrix} 1 & -2 & 1 \\ -2 & 4 & -2 \\ 1 & -2 & 1 \end{bmatrix}$$

(c) (d)

Figure 35 - Edge operators: (a)&(b) pair gradient operators, (c)&(d) single Laplace operators

The edge detection masks can be considered as a weighted window when the summation of weights is zero. In fact, these masks define high pass filters [97].

For detecting the edges, first the mask is applied into the image by:

$$g(m,n) = u(m,n) \otimes h(-m,-n) \tag{3.11}$$

where ⊗ represent the convolution operator.

For the operator with a pair of masks, each mask must be applied into the image separately, and then the magnitude gradient is calculated as:

$$g(m,n) = \sqrt{g_1^2(m,n) + g_2^2(m,n)} \tag{3.12}$$

Then, the pixel *(m,n)* is detected as an edge position if *g(m,n)* is greater than a threshold. The resulting image is a binary image, while the binary value of the edges is 1. The luminance histogram of *g(m,n)* gives the contrast distribution of the image which is useful for selecting the threshold. Since the edges play an important role in tracing the boundaries, it is essential to choose the proper value for thresholding.

3.2.3 Boundary Extraction

The outline of an object or the boundary of its hole can be found by connected edges. Two pixels are connected in a binary image if they have the same value. In the boundary detection, two types of connectivity are defined: four- and eight-connected neighbors [98], as shown in Figure 36.

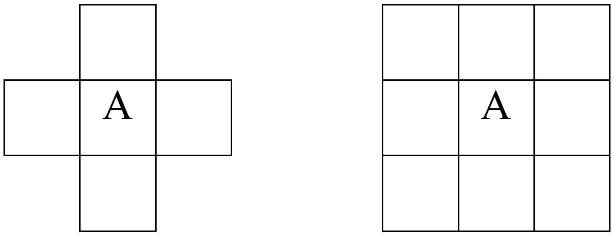

(a) (b)

Figure 36 - Pixel connectivity: (a) four-connected (b) eight-connected

Tracing the boundaries requires linking all connected edges which belong to the same boundary. Typically, these connected edges are linked by labeling. The pixels with the same labels represent the boundary an object or a hole.

3.2.4 Morphologic Operations

Once the boundaries of objects are extracted, further operations are required to localize a desired object in the image or extract certain features. An object can be recognized by its shape and geometric features which can be extracted by comparing with a template whose structures composed of line or arc patterns.

Mathematical morphology algorithms [99] refer to a set of simple operations based on shape structure, which are used for shape analysis and object detection. These techniques are different from many image processing algorithms because of their nonlinear approaches.

Morphologic operations usually are declared in binary mode and applied into the binary images such as the images resulting from the edge detection process. These operations require defining the structuring elements. The structuring element is a masking window when the origin pixel in the center is defined based on the structure of the shape which needs to be detected or extracted. Typical operations are dilation, erosion, opening, and closing, with the net effect of expanding, shrinking, simplifying, and smoothing the shapes [100], respectively.

The dilation of set *A* by set *B* denoted by $A \oplus B$ and defined as:

$$A \oplus B = \langle \max(z) | \left(\breve{B}\right)_z \cap A \neq \emptyset \rangle \tag{3.13}$$

where sets *A* and *B* are members of the 2D integer space; $\left(\breve{B}\right)_z$ is the translation of the reflection of the set *B* by point $z = (z_1, z_2)$ and obtained by

$$\begin{aligned} \breve{B} &= \{x | x = -b, for\ b \in B\} \\ (B)_z &= \{y | y = b + z, for\ b \in B\} \end{aligned} \tag{3.14}$$

In other words, the origin pixel is replaced by the maximum value of all the neighboring pixels in the structure window B. In a binary image, if the value of any of the neighboring pixels is 1, the origin pixel is set to 1.

The erosion of set *A* by set *B* denoted by $A \ominus B$ and defined as:

$$A \ominus B = \{\min(z) | (B)_z \subseteq A\} \tag{3.15}$$

where sets *A* and *B* are members of the 2-D integer space.

In other words, the value of origin pixel is set to the minimum value of all the neighboring pixels in the structure window B. In a binary image, if the value of any of the neighboring pixels is 0, the origin pixel is replaced by 0. The opening and closing operation are called dual operations.

An opening operation is defined by erosion followed by dilation with the same structuring element, while a closing operation is defined by dilation followed by erosion with the same structuring element.

3.3 Experimental Results

This section summarizes the experimental results based on the described multi-camera vision system. The multi-camera vision includes four surveillance IR-CCD cameras; their specifications are described in Table 1.

Table 1 - Camera specifications

Image Sensor	1/3" Color Sharp CCD
Effective Pixels	NTSC: 510(H) X492(V)
Unit Cell Size	9.6µm (H) × 7.5µm (V)
Sensor Size	4.8mm (H) × 3.6 mm(V)
Scanning System	2:1 Interlace
Signal System	NTSC
Infrared LED's	24 LED's
Infrared Illumination	60 ft
Minimum Luminance	0 Lux
Horizontal Resolution	420 TV Lines
S/N Ratio	Less than 48 dB
Gamma	0.45
Video Out	BNC

All cameras are connected to a PC through the IDS Falcon Quattro PCIe frame grabber, which includes four parallel video channels and is capable of capturing simultaneously images from four cameras with a sampling rate of 20 fps. Detailed characteristics of the frame grabber are listed in Table 2.

Table 2 - Frame grabber specifications

Hardware Interface	PCI Express Interface
Video Channels	4 Parallel Video Channels
Video Inputs	MAX 16 (4×4) CVBS video inputs
Video Outputs	1 CVBS video output
Digital Inputs	12 Digital Inputs
Digital Outputs	8 Digital Outputs
Frame size	Free scalability of frame sizes for each channel
Triggers	4 Triggers
Multi-board support	Up to 4 board
Other	Programmable EEPRO

3.3.1 Configuration Setup

As described, the cameras are arranged in a semicircle, as shown in Figure 37.

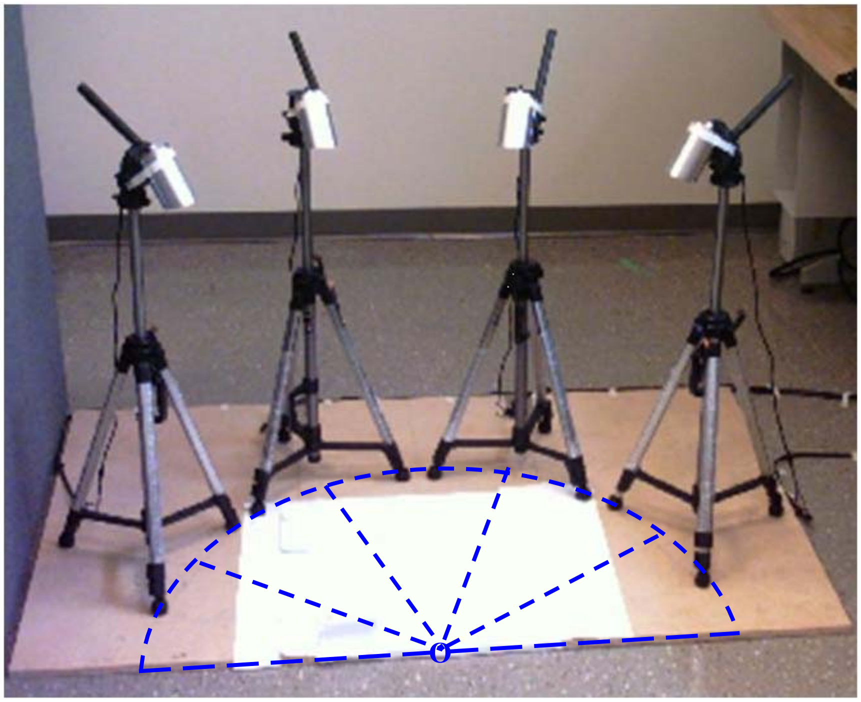

Figure 37 - Experimental setup for the multi-camera vision system

3.3.2 Single Calibration

The single calibration procedures are performed to obtain the intrinsic and extrinsic parameters for each single camera. The Camera Calibration Toolbox for MATLAB [101] is used for the single calibration. Calibration of the cameras is accomplished by using an 8×9 checkerboard with 5 cm×5 cm squares, as shown in Figure 32.

The Single calibration procedure requires a number of images of the checkerboard which are captured by each camera when the checkerboard is placed in different poses in the field of view of camera. In this experiment, 50 images are captured for each camera. As the stereo calibration is based on the two sets of left and right images which are captured simultaneously by two adjacent cameras, the images are acquired for two neighboring cameras at the same time, as shown in Figure 38 through Figure 43.

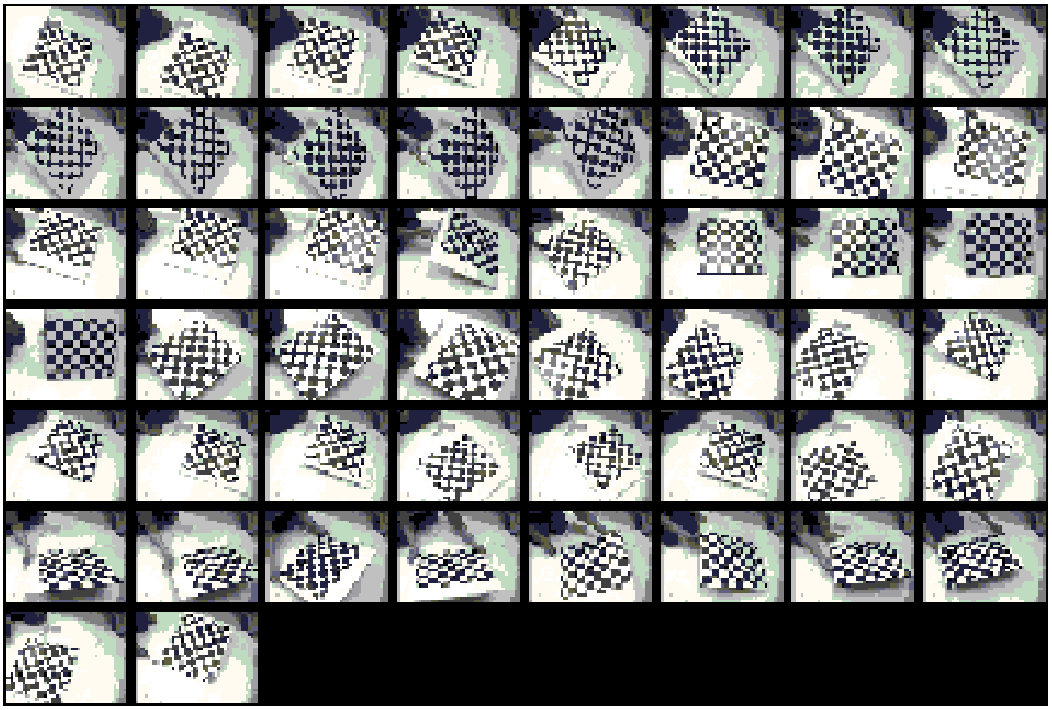

Figure 38 - Calibration images for camera #1 as a left camera for camera #2

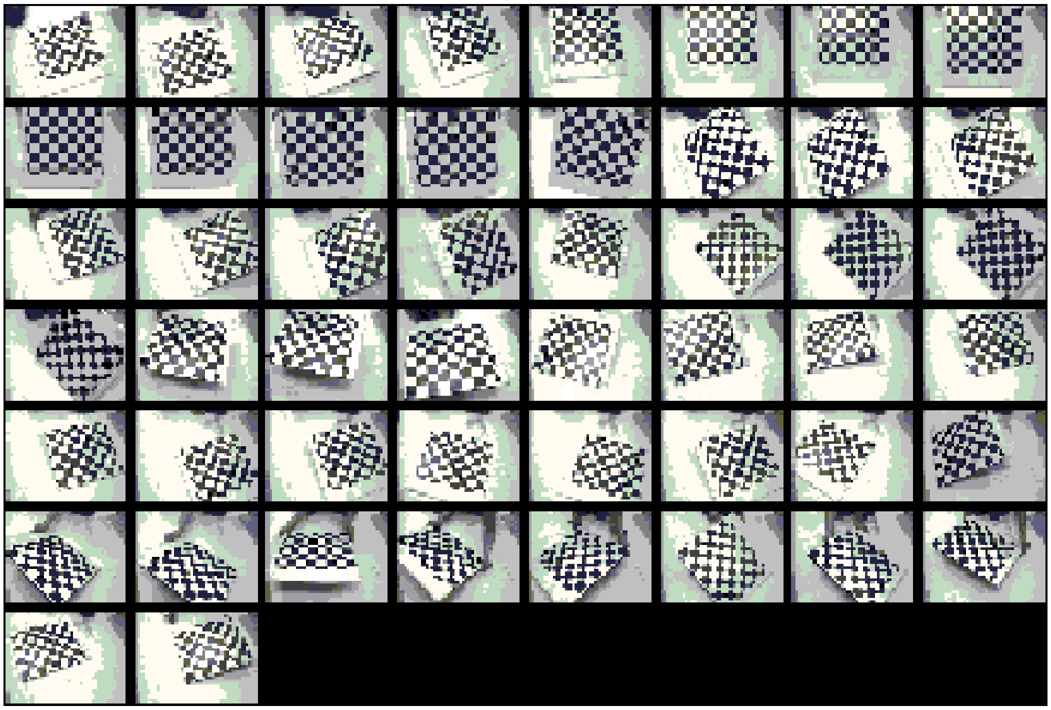

Figure 39 - Calibration images for camera #2 as a right camera for camera #1

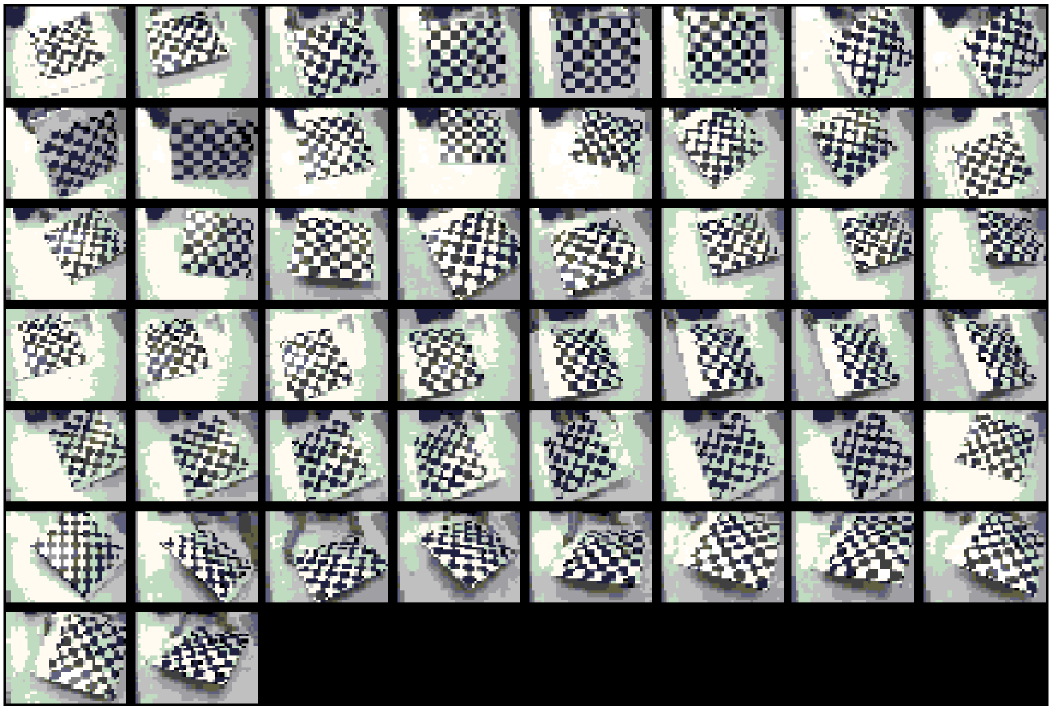

Figure 40 - Calibration images for camera #2 as a left camera for camera #3

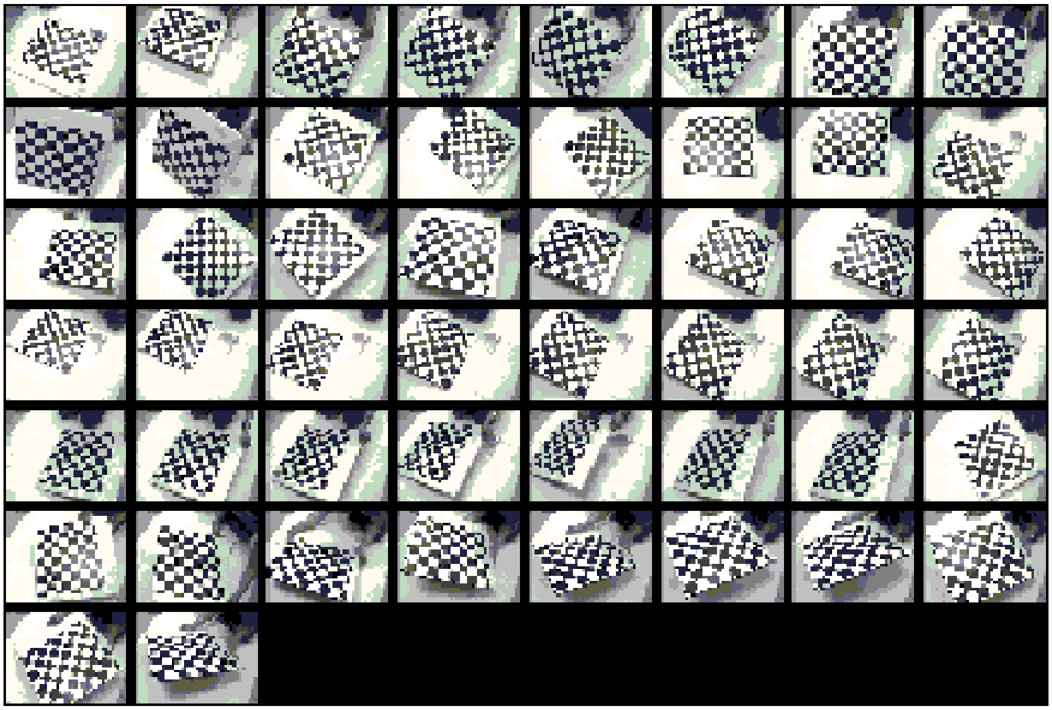

Figure 41 - Calibration images for camera #3 as a right camera for camera #2

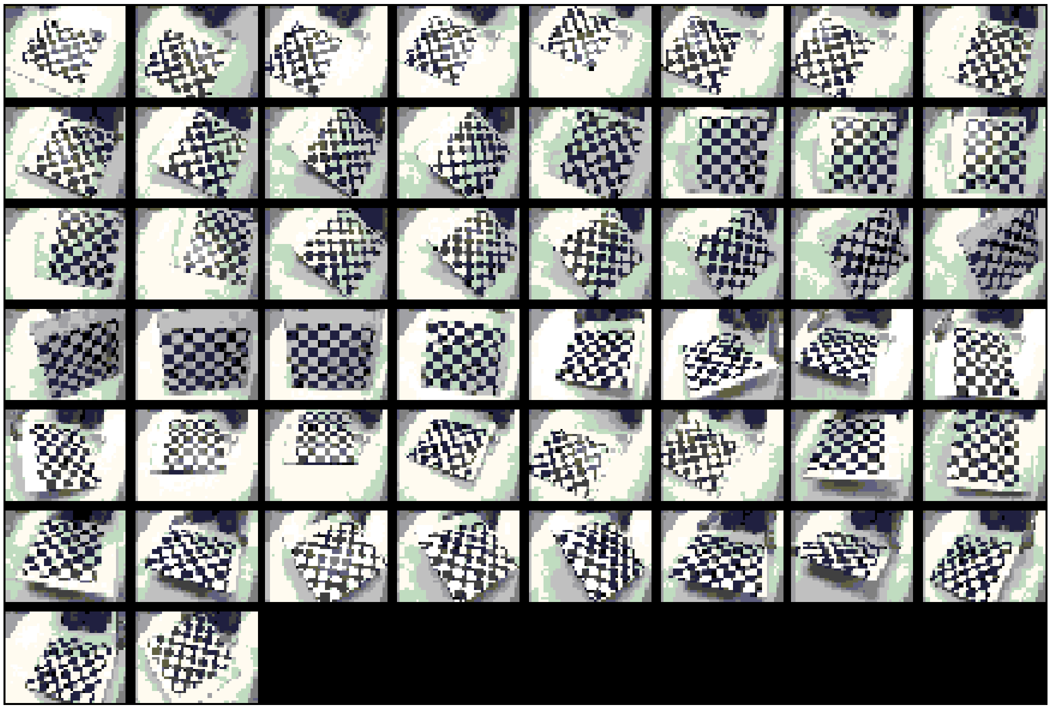

Figure 42 - Calibration images for camera #3 as a left camera for camera #4

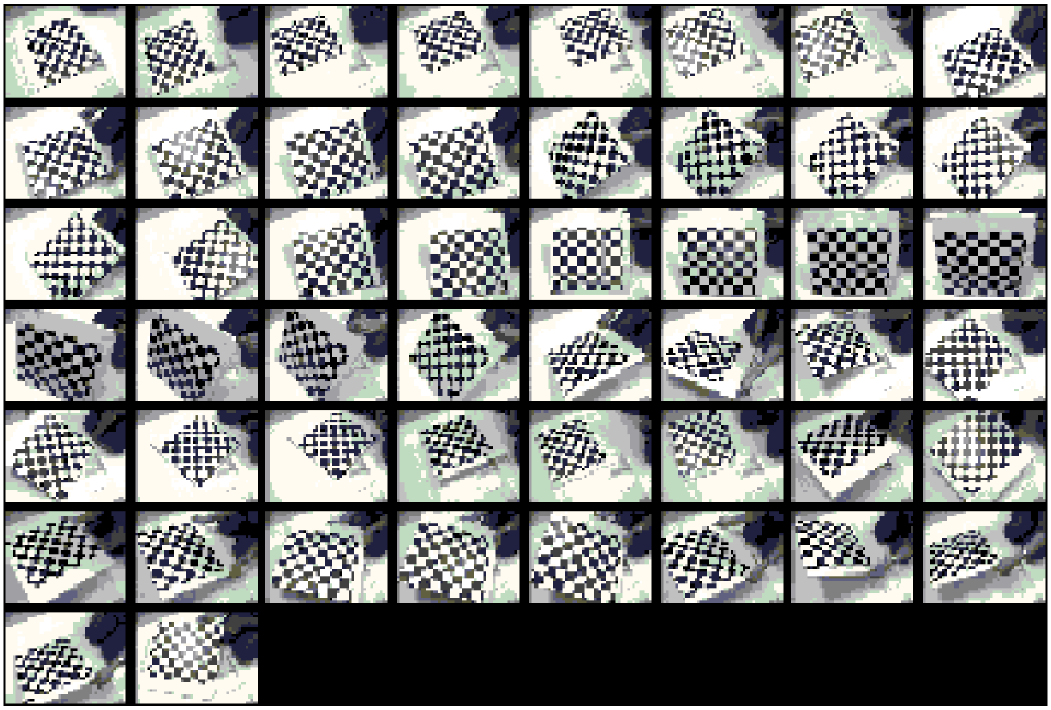

Figure 43 - Calibration images for camera #4 as a right camera for camera #3

Once the images are taken, the grid corners must be extracted for each single image. First, the four extreme corners on the rectangular checkerboard pattern must be indicated manually by clicking on them. As mentioned, the first chosen corner declares the origin of the coordinate frame and the sequence of choosing other three grids declares the direction of the coordinate frame for each image. Since the stereo calibration requires that the left and right images of the same scene have the same coordinate frame, the same sequence must be chosen for every single frame.

Afterwards, the program extracts all grid corners bounded by the four extreme corners, as shown in Figure 44.

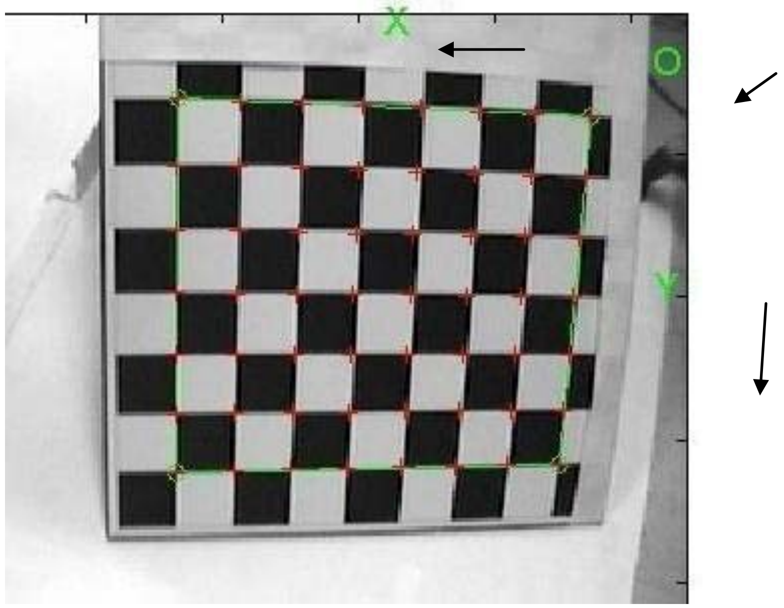

Figure 44 - Grid extraction for a sample image

Once the grid corners for all images of each camera are extracted, the intrinsic and extrinsic parameters of the camera can be estimated. The resulting intrinsic parameters of each camera are listed in Table 3.

Table 3 - Intrinsic parameters

	Camera #1	Camera #2	Camera #3	Camera #4
Focal Length	3.865 mm	3.8442 mm	3.8890 mm	3.8458 mm
Image Scale Factor	0.7776	0.7775	0.7753	0.7776
Principal Point	X: 131.12 pixels Y: 130.10 pixels	X: 152.74 pixels Y: 122.79 pixels	X: 144.77 pixels Y: 118.23 pixels	X: 136.90 pixels Y: 145.34 pixels
Distortion Coefficients	$K_{r,x}$: -0.3494 $K_{r,y}$: 0.1511 $K_{t,x}$: 0.0032 $K_{t,y}$: -0.0030	$K_{r,x}$: -0.3522 $K_{r,y}$: 0.1608 $K_{t,x}$: 0.0047 $K_{t,y}$: -0.0005	$K_{r,x}$: -0.3567 $K_{r,y}$: 0.0998 $K_{t,x}$: -0.0024 $K_{t,y}$: 0.0016	$K_{r,x}$: -0.3522 $K_{r,y}$: 0.0885 $K_{t,x}$: 0.0024 $K_{t,y}$: -0.0002
Skew Coefficient	0.00	0.00	0.00	0.00

By using the estimated radial and tangential distortion parameters, the complete model of the camera distortion can be computed. For example, the complete distortion model of Camera #1 is shown in Figure 45, while the radial and tangential distortion models are represented in Figure 46 and Figure 47, respectively.

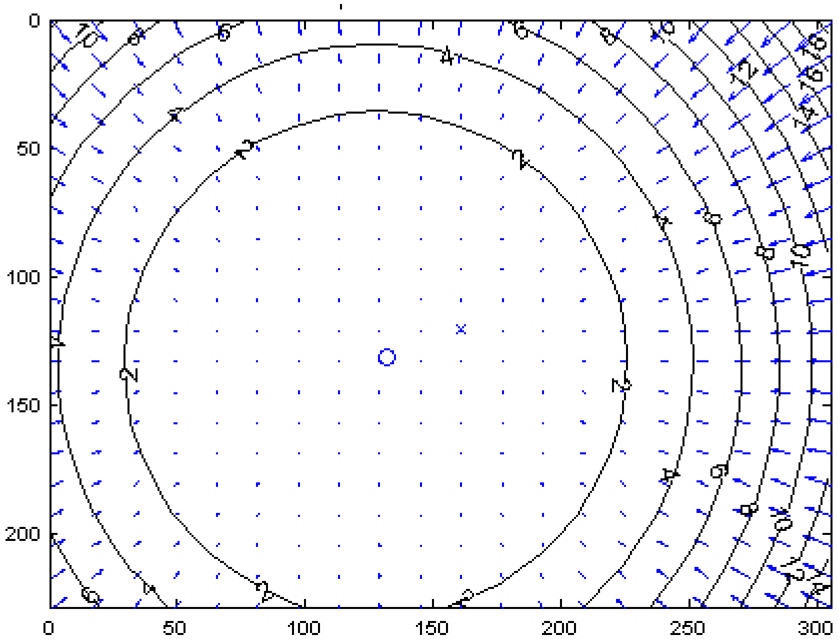

Figure 45 - Complete distortion model of camera #1

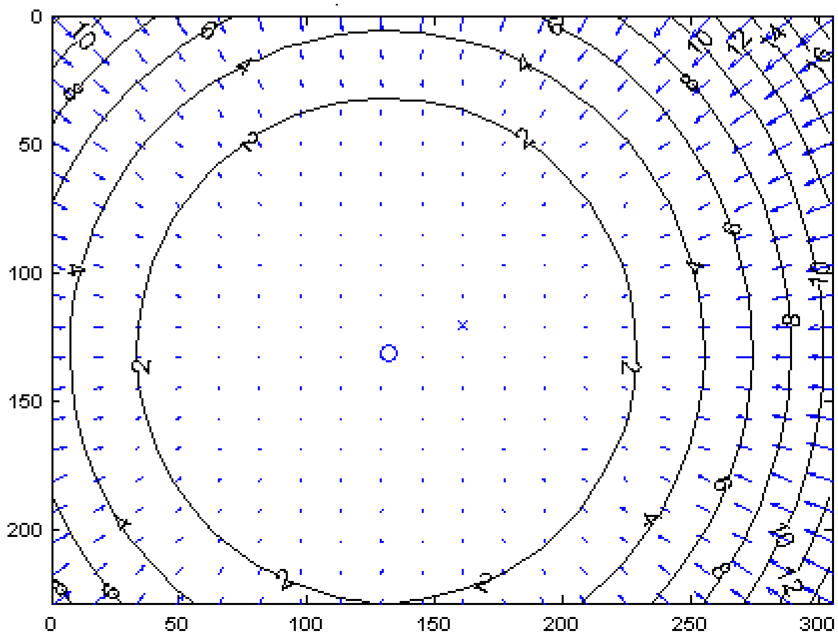

Figure 46 - Radial component of distortion model of camera #1

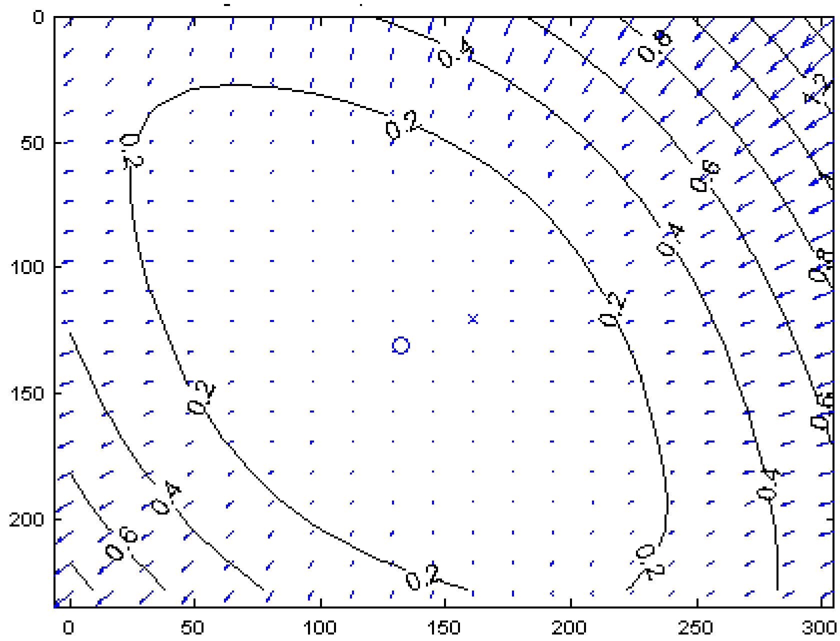

Figure 47 - Tangential component of distortion model of camera #1

Furthermore, the extrinsic parameters in both camera-centered and world-centered of each set of calibration images in Figure 38 through Figure 43 are represented in Figure 48 through Figure 53. It should be mentioned that because of simplifying the parameters estimation, the skew coefficients of cameras are assumed to be zero.

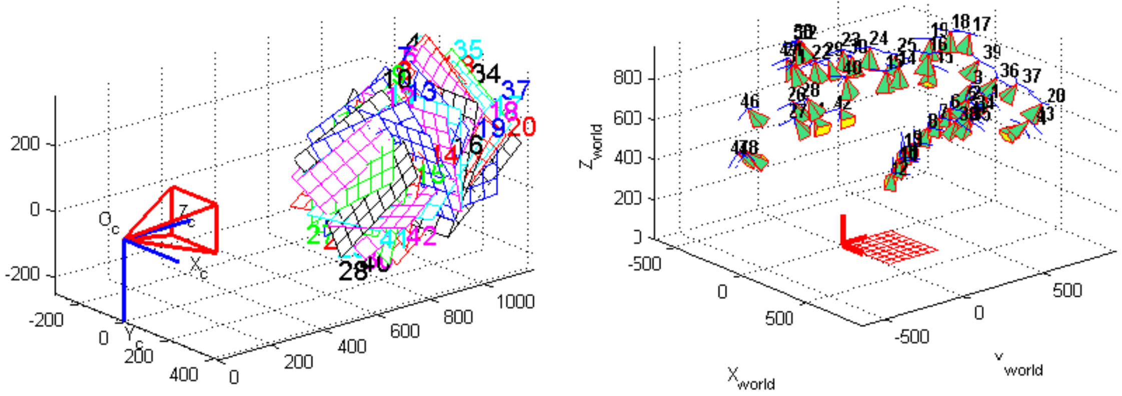

Figure 48 - Extrinsic parameters cam #1 in Figure 38: (left) camera-centered, (right) world-centered

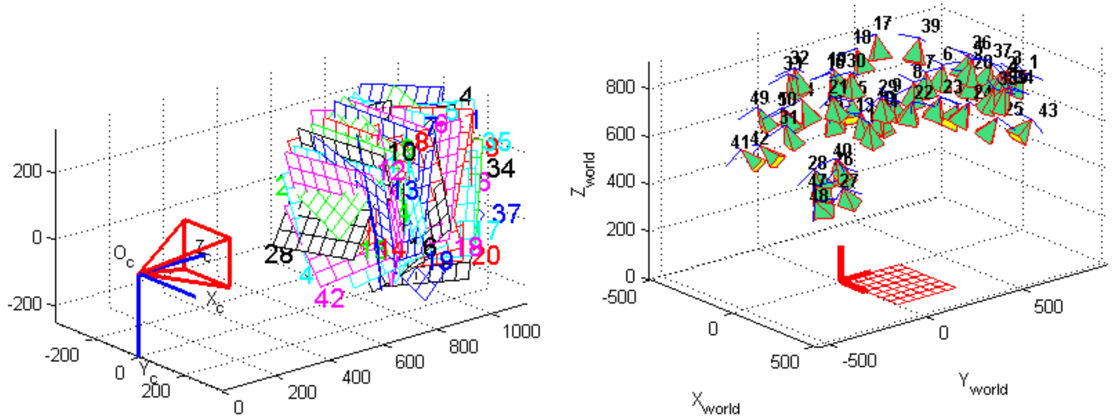

Figure 49 - Extrinsic parameters cam. #2 in Figure 39: (left) camera-centered, (right) world-centered

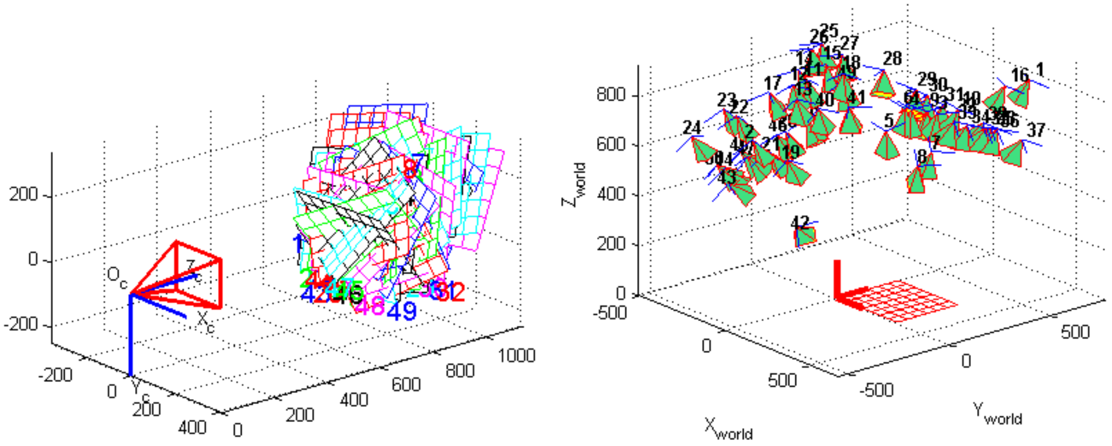

Figure 50 - Extrinsic parameters cam. #2 in Figure 40: (left) camera-centered, (right) world-centered

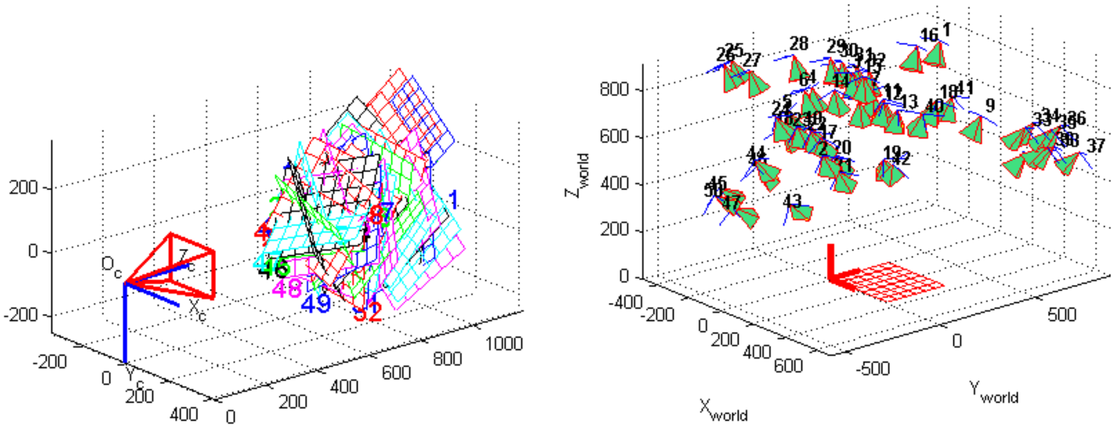

Figure 51 - Extrinsic parameters cam. #3 in Figure 41: (left) camera-centered, (right) world-centered

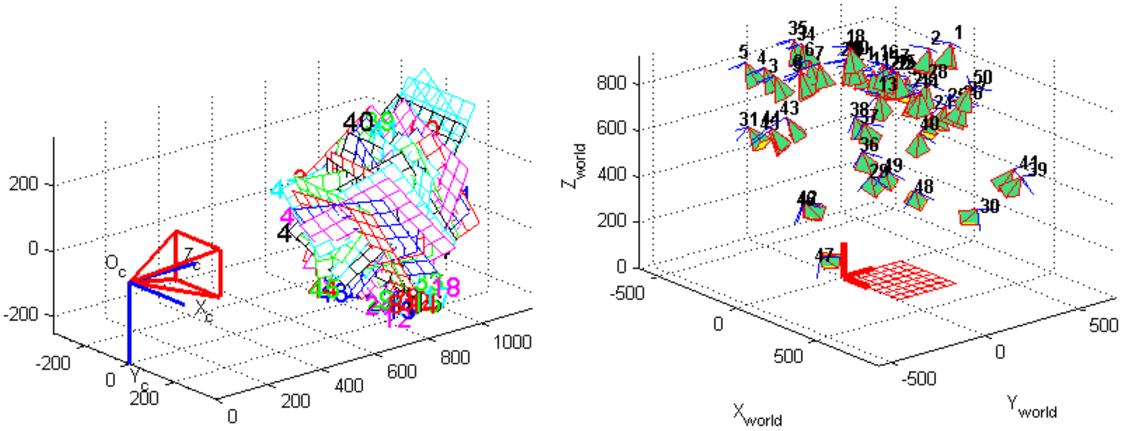

Figure 52 - Extrinsic parameters cam. #3 in Figure 42: (left) camera-centered, (right) world-centered

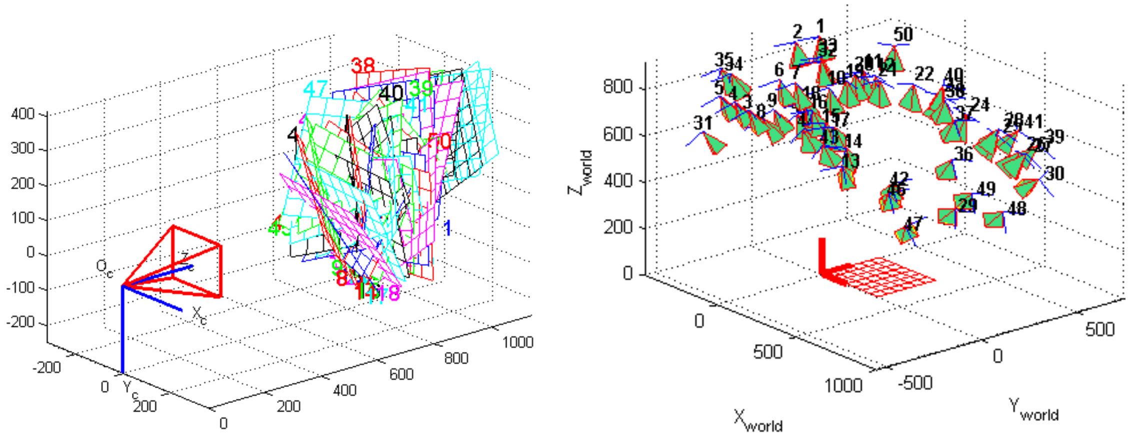

Figure 53 - Extrinsic parameters cam. #4 in Figure 43: (left) camera-centered, (right) world-centered

In addition, introducing the world coordinate system requires that all four cameras observe the checkerboard and capture its image at the same time, as shown in Figure 33.

Since the single calibration images includes the above corresponding images for each camera, the rotation and translation vectors for transforming each point in the camera frame to the navigation frame are calculated by the single calibration procedure. Table 4 shows the transformation parameters for each individual camera.

Table 4 - Transformation parameters from each camera frame to the world coordinate system

	Camera #1	Camera #2	Camera #3	Camera #4
Rotation Vector	1.552265 2.255665 -0.635153	0.4686021 2.889162 -0.7405382	0.6128003 -2.859007 0.7741390	1.537200 -2.314144 0.4821106
Translation Vector	729.4870 mm 293.6999 mm 873.3399 mm	385.2578 mm 625.1560 mm 840.7220 mm	-61.1933 mm 623.1377 mm 851.9321 mm	-365.5847 mm 289.6135 mm 848.5442 mm

3.3.3 Stereo Calibration

The stereo calibration process refers to an algorithm of estimating extrinsic parameters of the right camera with respect to the left camera for each two adjacent cameras. The result of the stereo calibration allows applying the triangulation technique to estimate the depth of the desired object.

Since the captured images for each of two neighboring cameras in the single camera calibration phase are followed the required rule for executing the stereo calibration procedure, the direct result of the single calibration step can be employed in the stereo calibration algorithm. Table 5 shows the rotation and translation vector for transforming each point in the right camera frame to the left camera frame.

Table 5 - Extrinsic parameters for each two adjacent cameras

	Camera #1 & #2	Camera #2 & #3	Camera #3 & #4
Rotation Vector	0.02865 0.42562 0.76695	-0.03225 0.42071 0.63442	0.09050 0.42463 0.64168
Translation Vector	-431.649730 mm -197.41507 mm 55.10179 mm	-410.24851 mm -147.60000 mm 105.27998 mm	-419.84660 mm -134.27390 mm 94.60045 mm

3.3.4 Image Processing

In this research, the image processing techniques are applied to every single frame from each camera to localize the tool tip. The results of the image processing techniques are shown on a selected image which is displayed in Figure 54.

Figure 54 - Original Image

First, the average operator with the window mask of 3×3 is applied to reduce the effect of the isolated noise as shown in Figure 55.

Figure 55 - Denoised image

As a result of the noise reduction, the original image is blurred and the edges are distorted. Therefore, unsharp masking is used to sharpen the edges and image adjustment is applied to enhance the contrast of the image to restore the distorted edges, Figure 56 and Figure 57..

Figure 56 - Edge Enhancement

Figure 57 - Contrast Enhancement

In order to extracting the tool tip, the edge detection and boundary extraction are required. In order to obtain the gradient of the image, each pair of the Sobel operator is applied to the enhanced image from the last step, and then the magnitude of the gradient is computed for the first step of the edge detection, see section 3.2.2.

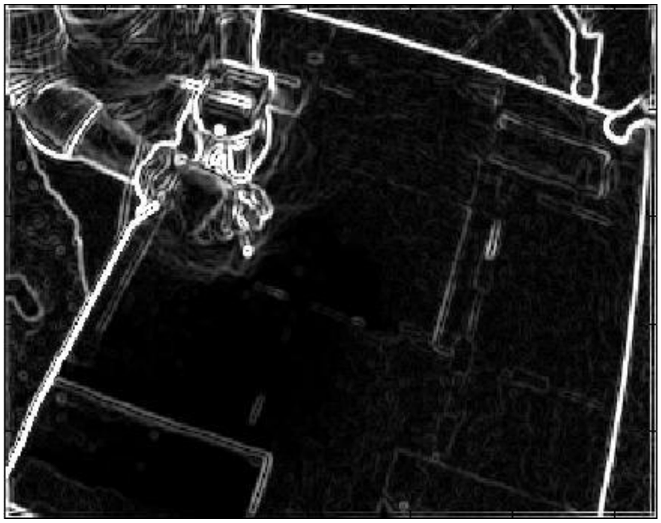

Figure 58 - Detected edge by gradient operator

Obtaining the edge of the tool tip requires thresholding. Each pixel is detected as an edge if its gradient is greater than the threshold. In this research, the threshold is chosen as the boundary pixels of the tool tip are detected as the edge positions. Since the size of the tool tip is about a few pixels, then recursive thresholding is applied to remove the noise pixels around the tool tip as much as possible. For this purpose, a masking window is chosen around the initial guess of the position of the tool tip. Then, a fixed threshold is chosen which select pixels that their value is above the %80 of the value of all pixels of the image. If the boundary detection technique can identify the boundary of the tool tip, then it shows that the threshold selection is appropriate. Otherwise, the previous threshold is reduced by %5, and this procedure is run recursively to find the proper threshold. The desired edges are detected by thresholding shown in Figure 59.

Figure 59 - Detected Edges

Afterwards, the opening morphologic operation followed by closing operation is applied to simplify and smooth the shape of the tool tip. As shown in Figure 60, the undesired pixels which are detected as an edge will be removed. As a result, the position of the masking window and the tool tip will be computed more accurately.

Figure 60 - The effect of opening morphologic operations followed by closing operation

Finally, the boundary of the tool tip can be detected and extracted by using the eight-connected neighbors, illustrated in Figure 61.

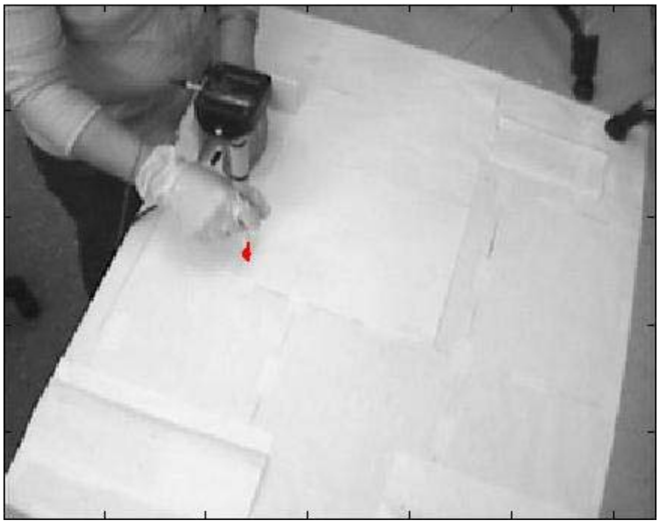

Figure 61 - Extracted boundary of the tool tip

Since the initial position of the tool tip in the first frame is known, the masking window is chosen based on this position, see Figure 62.

Figure 62 - Initial guess window mask for the position of tool tip

After boundary detection, the mask is relocated to keep the tool tip in the middle of the window demonstrated in Figure 63.

Figure 63 - Mask repositioning

The new position of the mask is the initial guess for searching the tool tip in next image frame. In fact, the relocated mask in each frame is the initial guess masking window for the next frame.

3.3.5 Tool Tracking

After estimating all required parameters of the vision system and applying image processing techniques, each single camera can track the tool tip. Figure 64 through Figure 67 demonstrate the result of the video tracking by each camera.

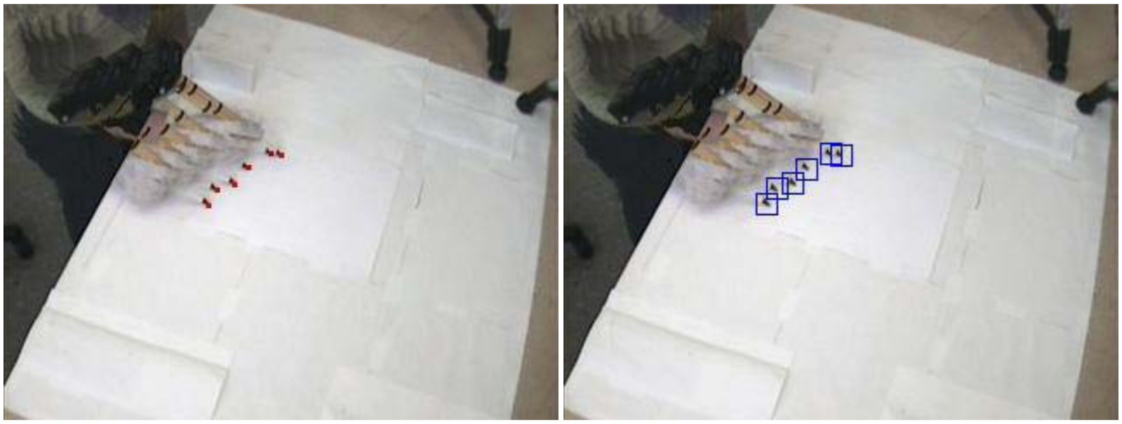

Figure 64 - Tool tip tracking by camera #1

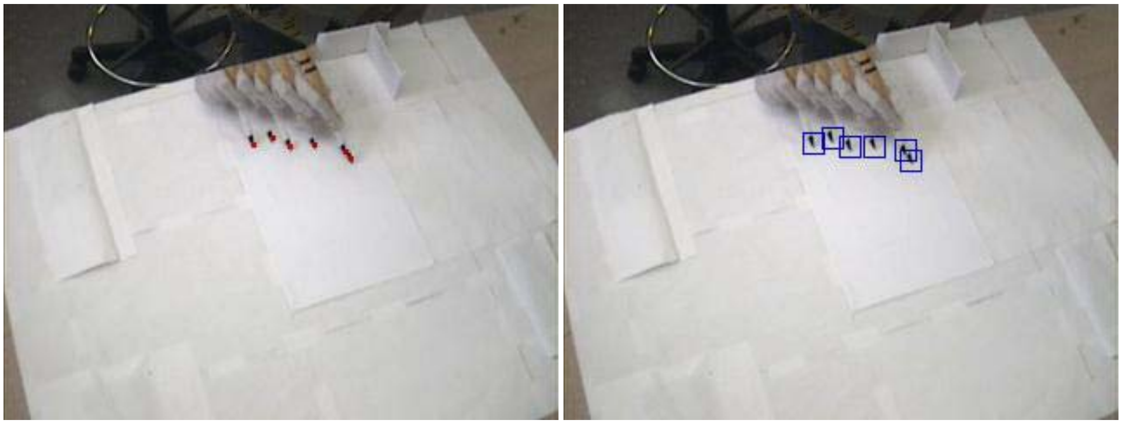

Figure 65 - Tool tip tracking by camera #2

Figure 66 - Tool tip tracking by camera #3

Figure 67 - Tool tip tracking by camera #4

The 3D position of the tool tip can be estimated by using the measured 2D position of the tool tip in the image plane by each two adjacent cameras and employing the triangulation technique while knowing the intrinsic and extrinsic parameters of cameras. Subsequently, the average of three 3D estimated positions resulting from each two neighboring cameras is calculated as the final 3D tool tip position.

Figure 68 through Figure 70 show the estimated position of the proposed multi-camera vision system versus the estimated position of each two neighboring cameras and the original traced path.

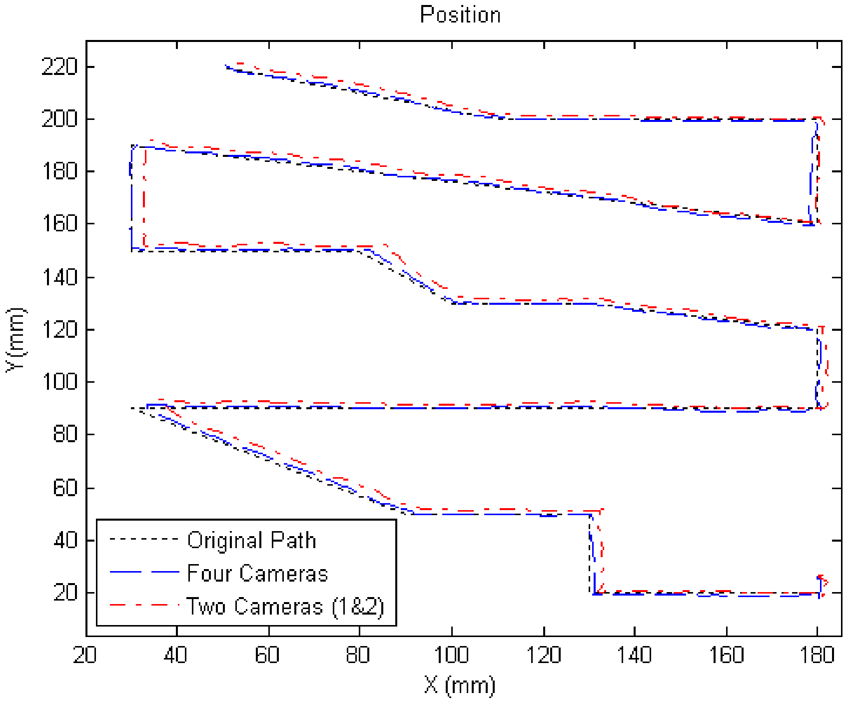

Figure 68 - Comparison of the positioning with the use of two cameras (1&2) and four cameras

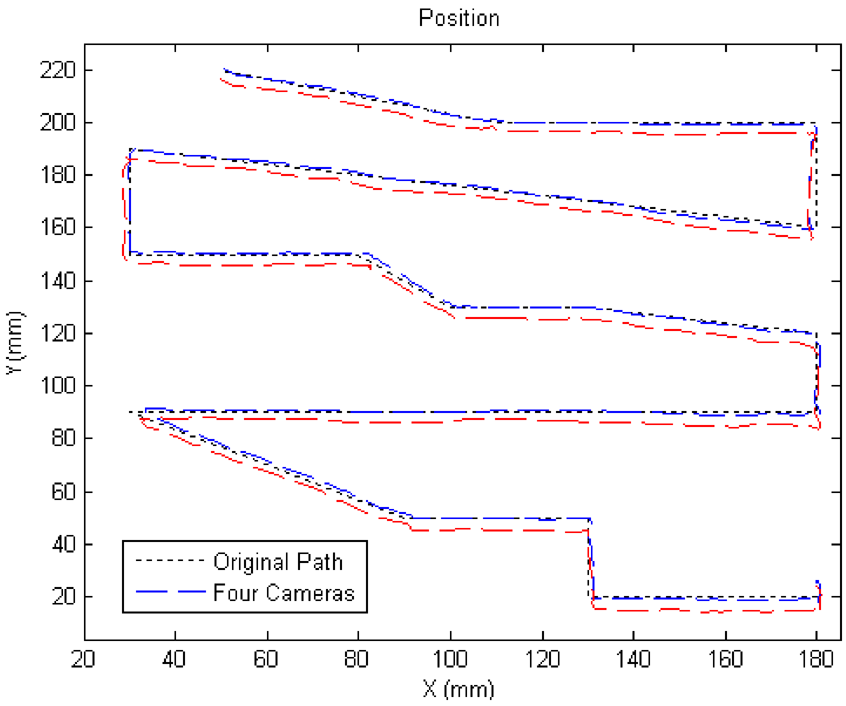

Figure 69 - Comparison of the positioning with the use of two cameras (2&3) and four cameras

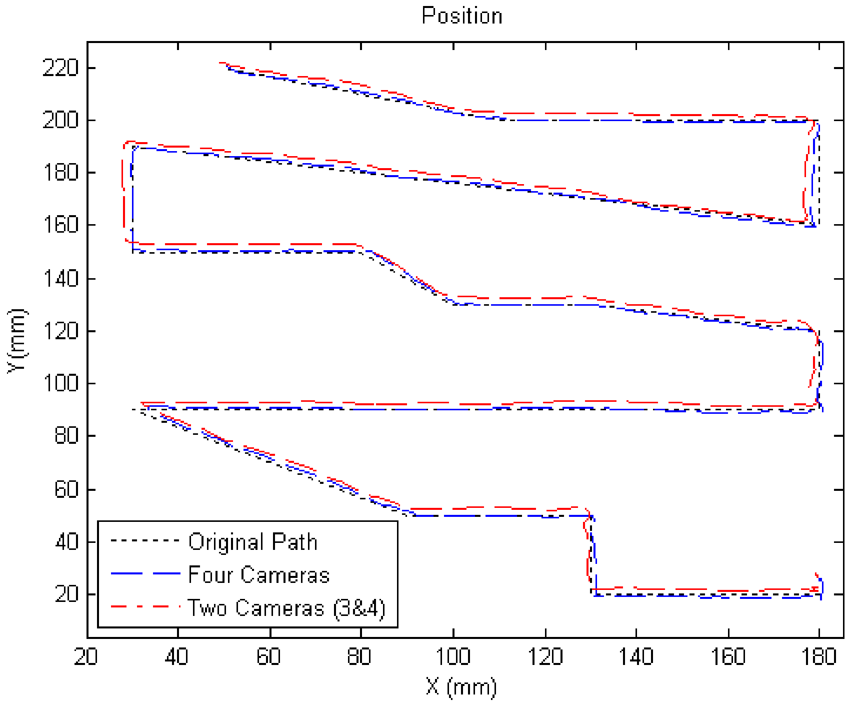

Figure 70 - Comparison of the positioning with the use of two cameras (3&4) and four cameras

Table 6 - The position error of the multi-camera vision system compared with each camera pair

Camera Pair	Positioning Error reduction	Variance
Cameras #1 and #2	2.1 mm RMS	0.881
Cameras #2 and #3	3.5 mm RMS	0.958
Cameras #3 and #4	2.8 mm RMS	0.488

As illustrated in Table 6, the error of the vision system is significantly reduced by employing the proposed camera arrangement; but the error is still considerable for some applications.

Accordingly, the maximum error is occurred at section 2 which is about 5 mm. These errors are resulted from two factors: human hand motion error and vision system error.

It should be mentioned that a predesigned path is printed on the 2D plane and it is tried to be traced by the tool tip during its movement on the plane.

In fact, because of hand tremor and other physiological factors, the precision of the hand manipulation is restricted; therefore, the desired path cannot be traced accurately by hand motion. The resulted errors can not be measured by available instruments in our lab. In addition, the positioning error of the multi camera vision system with respect to the predesigned path can not be evaluated, since this path is independent of the time and the tracing speed. Figure 71 compares the pre-designed path with the traced path by tool tip moved by hand.

Since the pre-designed path is almost traced by tool tip, all results are compared with the pre-designed path.

The locations of the maximum errors occurred during video tracking are shown in Figure 72 and their magnified images are listed in Table 7.

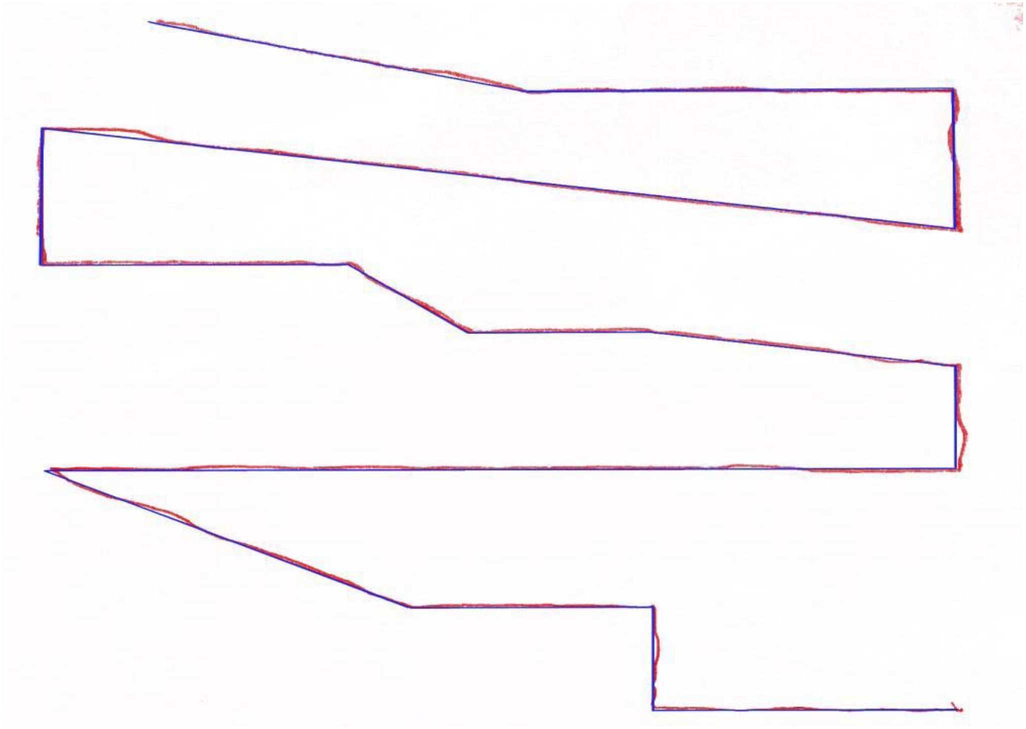

Figure 71 - The traced path by tool tip (red) in comparison with the pre-designed path (blue)

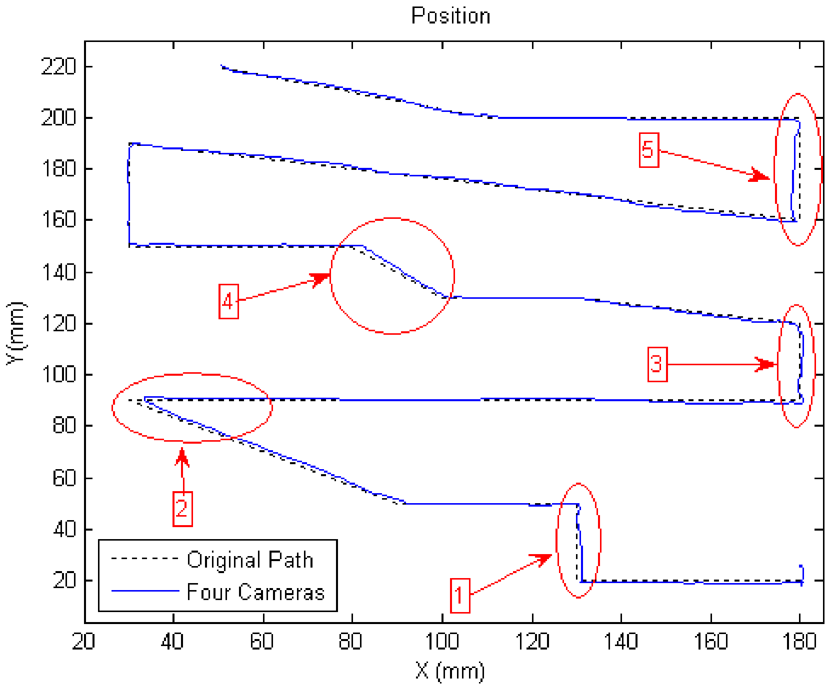

Figure 72 - The location of the maximum errors occurred during video tracking

Table 7 - Magnified images of the maximum errors in the tool tip positioning

<table>
<tr><th>Error At Section</th><th>Magnified Image</th></tr>
<tr><td>1</td><td>
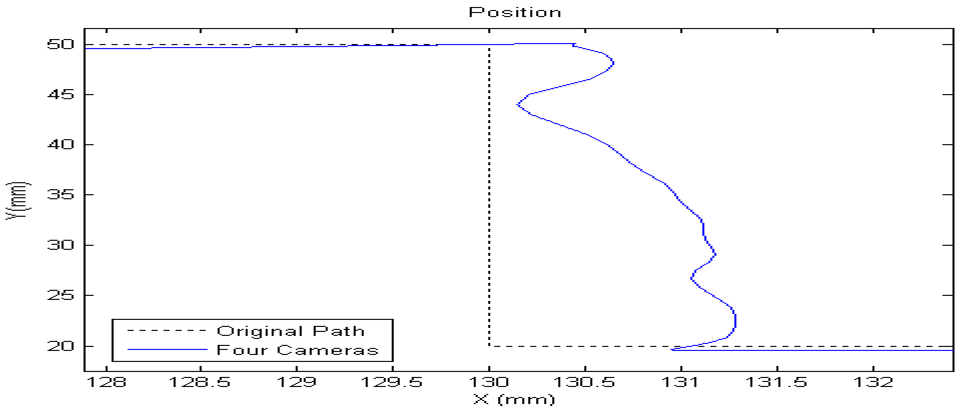

</td></tr>
<tr><td>2</td><td>
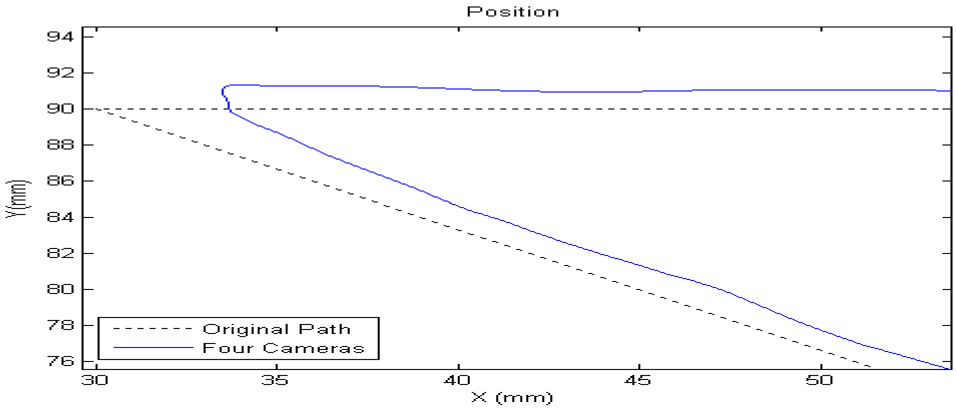

</td></tr>
<tr><td>3</td><td>
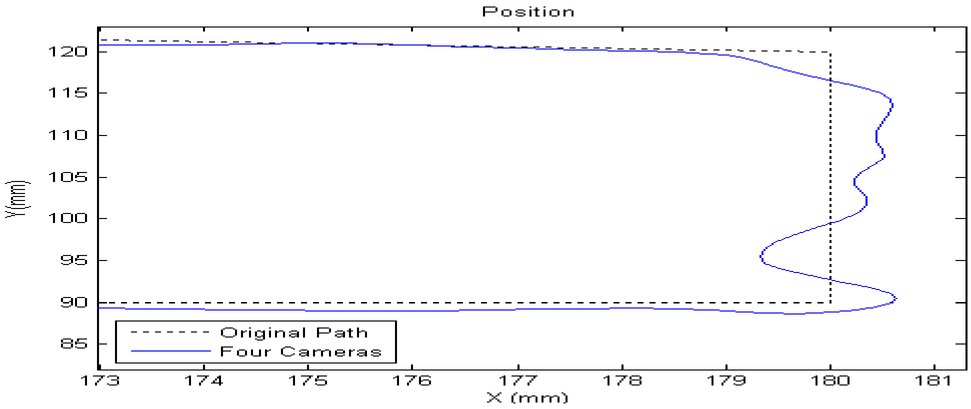

</td></tr>
</table>

Table 7 - Continued

Error At Section	Magnified Image
4	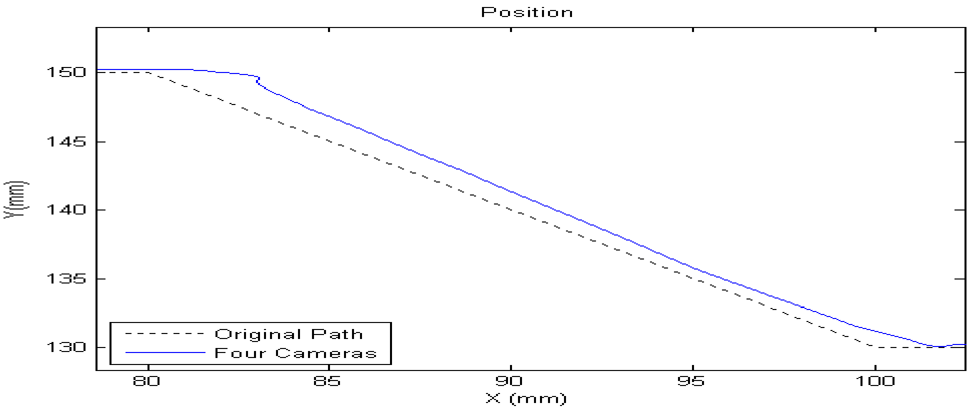
5	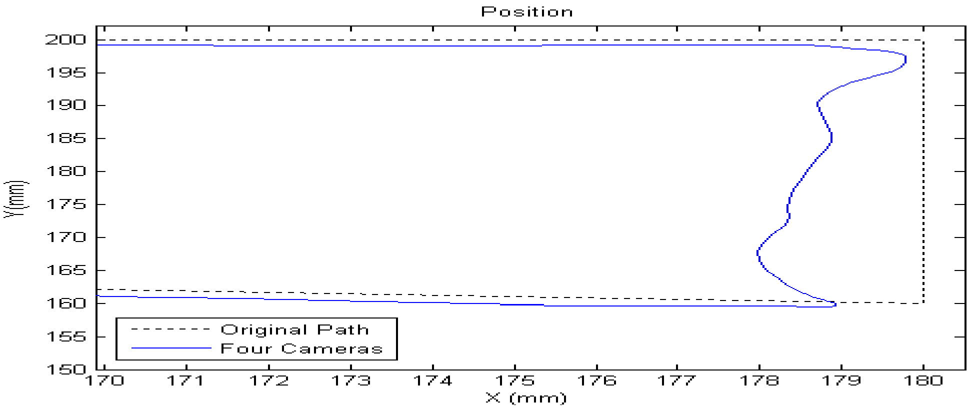

The low quality of the cameras, calibration error, object detection error, and tracking algorithm error lead to the positioning error of the vision system. However, the complex algorithms are designed in computer vision to reduce the error of the video tracking; implementing these algorithms to respond in real time requires advanced, high-speed, and multi-processor PCs, which are usually extremely expensive.

3.4 Summary

This chapter details a multi-camera vision system. The proposed vision system includes four cameras located in a semicircle instead of arranged in the classical pattern. As a result, the entire workspace is covered by this configuration is expanded and a wide circular field of view is provided. As a result, the possibility of the loss of line-of-sight is reduced.

Furthermore, the accuracy of the vision system increases by using multi-cameras; however, its precision is affected by the low quality of the cameras, calibration error, object detection error, and tracking algorithm error. Reducing the error of the video tracking requires applying complex computer vision algorithms whose implementation algorithms needs advanced multi-processor PCs to respond in real time.

However, low-quality cameras and simple image processing techniques are applied; the experimental result shows that the accuracy of the multi-camera vision system is less than 5 mm and acceptable for many applications.

Chapter 4

Extended Kalman Filter

Most research studies show that the inertial navigation sensors have drifts. There are two components in the inertial sensor drift, bias stability and bias variability. These components are involved in double integration in position calculation; so after a while, the output of the inertial navigation system (INS) is not reliable. To remove the resulted drifts in position, the INS is assisted by other positioning technologies such as GPS, vision system, or odometer.

The use of Kalman filters is a common method in the data fusion technique. The Kalman filter technique is a powerful method for improving the output estimation and reducing the effect of the sensor drift. Different Kalman filters are being developed in the area of the sensor fusion [20- 25].

In the past, the three-dimensional attitude representations were applied, but these representations are singular or discontinuous for certain attitudes [65]. As a result, the quaternion parameterization was proposed, which has the lowest dimensional possibility for a globally non-singular attitude representation [51, 66].

In assisted inertial navigation systems, the state variables of a Kalman filter usually take one of two forms: first, the sensed quantities such as acceleration, velocity, and attitude, etc.; and second, the errors of these quantities. The first form is used by the centralized Kalman filter [25], unscented Kalman filter [48, 102, 103], adaptive Kalman filter [50, 104], and sigma-point extended Kalman filter [105], while the second one is used by the indirect Kalman filter [26, 27,106].

A Kalman filter that operates on the error states is called an indirect or a complementary Kalman filter. The optimal estimates of the errors are then subtracted from the sensed quantities to obtain the optimal estimates. Since the 1960s, the complementary Kalman filter has become the standard method of integrating non-inertial with inertial measurements in aircrafts and spacecrafts navigation. This method requires dynamic models for both the navigation variable states and the error states [64].

In this chapter, a modified EKF is developed. In this filter method, the magnitude of the changes in position and velocity are estimated and then added to the previous estimation of the position and velocity, respectively.

4.1 General Extended Kalman Filter

Extended Kalman filter (EKF) is an estimation method for conveniently integrating data provided by various sensors in order to obtain the best estimate for the states of a nonlinear dynamic system [107]. Figure 73 shows a block diagram of the integration of the multi-camera vision system and the inertial navigation system:

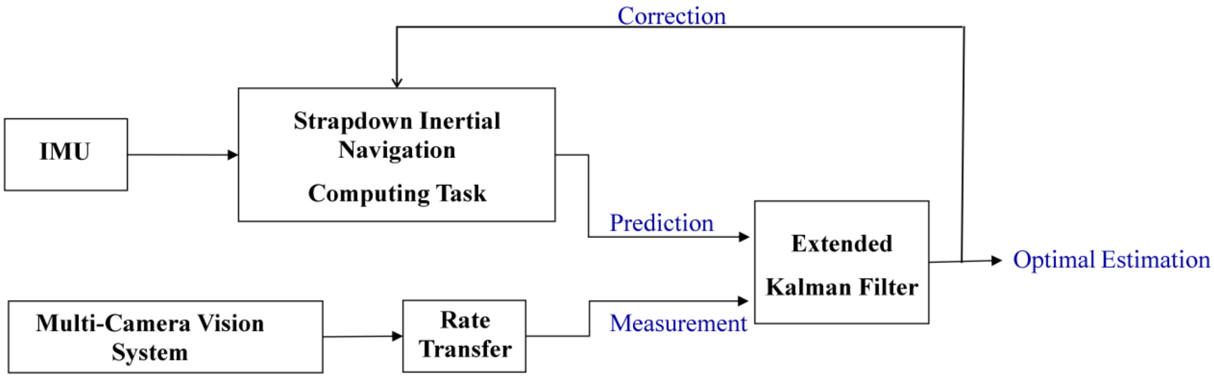

Figure 73 - Integration of SDINS and vision system with using EKF

Typically, EKF is applied by combining two independent estimates of a nonlinear variable [3, 108]. The continuous form of a nonlinear system is described as:

$$\begin{aligned} \dot{x}(t) &= f(x(t),t) + G(t)\eta(t) \\ z(t) &= h(x(t),k) + n \end{aligned} \tag{4.1}$$

where the system noise and the measurement noise are zero-mean Gaussian random processes with known covariance R and S, respectively.

4.1.1 System Model

By considering the state-space vector $X = [x_1\ x_2\ x_3]^T = [r\ v\ q]^T$ and the input noise η, the set of equation (2.50) can be revised as follows:

$$\begin{aligned} \dot{r}^n &= v^n = f_1(x_2) \\ \dot{v}^n &= C_b^n(f_A - a_t - a_n) + g_n + C_b^n \eta_1(t) = f_2(x_3) + g_2(x_3)\, \eta_1(t) \\ \dot{q} &= \frac{1}{2}\Lambda_{nb}^n\, q + \frac{1}{2}Q(q)\eta_2(t) = f_3(x_3) + g_3(x_3)\, \eta_2(t) \end{aligned} \tag{4.2}$$

or

$$\begin{bmatrix} \dot{r} \\ \dot{v} \\ \dot{q} \end{bmatrix} = \begin{bmatrix} 0 & I & 0 \\ 0 & 0 & 0 \\ 0 & 0 & 0.5\Lambda \end{bmatrix} \begin{bmatrix} r \\ v \\ q \end{bmatrix} + \begin{bmatrix} 0 \\ C_b^n(f_A - a_t - a_n) + g_n \\ 0 \end{bmatrix} + \begin{bmatrix} 0 & 0 \\ 0 & C_b^n \\ 0.5Q(q) & 0 \end{bmatrix} \eta(t) \tag{4.3}$$

4.1.2 Measurement Model

The multi-camera vision system with the Gaussian noise of *n~N(0,S)* provides the position of the tool tip; therefore, velocity can be computed by taking the derivation of the position:

$$\begin{gathered} z = \begin{bmatrix} I & 0 & 0 \\ 0 & I & 0 \\ 0 & 0 & 0 \end{bmatrix} \begin{bmatrix} r \\ v \\ 0 \end{bmatrix} + n \\ v = \frac{\partial r}{\partial t} \end{gathered} \tag{4.4}$$

As mentioned, the derivative of noisy signals generates a noisy result with the very large magnitudes. In order to address this problem, the input signal must be smoothed and the resulted signal must be filtered by a low-pass filter.

4.1.3 Extended Kalman Filter Equations

According to the general model of the system in equation (4.1), f is defined as:

$$f = \begin{bmatrix} v \\ C_b^n(f_A - a_t - a_n) + g_n \\ \frac{1}{2}\Lambda\, q \end{bmatrix} \tag{4.5}$$

Applying the EKF requires obtaining the transition matrix by linearizing f about the current estimated state [2, 109]. The following matrix F is computed by assuming the state-space vector $X = [r\ v\ q]^T$ and $a = (f_A - a_t - a_n)$:

$$F \equiv \frac{\partial f}{\partial X}\bigg|_{X=\overset{\frown}{\tilde{X}}} = \begin{bmatrix} 0 & I & 0 \\ 0 & 0 & \dfrac{\partial}{\partial q} C_b^n a \\ 0 & 0 & 0.5\Lambda \end{bmatrix} \tag{4.6}$$

where $\frac{\partial}{\partial q} Ca$ is computed as:

$$\begin{aligned} \frac{\partial}{\partial q} Ca = 2 &\left[\begin{matrix} q_1a_1 - q_4a_2 + q_3a_3 & q_2a_1 + q_3a_2 + q_4a_3 \\ q_4a_1 + q_1a_2 - q_4a_3 & q_3a_1 - q_2a_2 - q_1a_3 \\ -q_3a_1 + q_2a_2 + q_1a_3 & q_4a_1 + q_1a_2 - q_2a_3 \end{matrix}\right. \\ &\qquad\qquad \left.\begin{matrix} -q_3a_1 + q_2a_2 + q_1a_3 & -q_4a_1 - q_1a_2 + q_2a_3 \\ q_2a_1 + q_3a_2 + q_4a_3 & q_1a_1 - q_4a_2 - q_1a_3 \\ -q_1a_1 + q_4a_2 - q_3a_3 & q_2a_1 + q_3a_2 + q_4a_3 \end{matrix}\right] \end{aligned} \tag{4.7}$$

Since the measurement model is a linear function, then the observation matrix is defined as:

$$H = \begin{bmatrix} I & 0 & 0 \\ 0 & I & 0 \\ 0 & 0 & 0 \end{bmatrix} \tag{4.8}$$

As a result, the predication and update steps of the EKF can be written as:

Prediction:

$$\begin{aligned} \tilde{x}_{k+1} &= f\left(\overset{\frown}{\tilde{x}}_k, k\right) \\ \tilde{P} &= F_k P_k F_k^T + G_k R_k G_k^T \end{aligned}$$

(4.9)

Update:

$$\begin{aligned} \overset{\frown}{\tilde{x}}_{k+1} &= x_{k+1} + K[z_{k+1} - h(\tilde{x}_k, k)] \\ P_{k+1} &= \tilde{P} - KH_k\tilde{P} \\ K &= \tilde{P}H_k^T(S_k + H_k\tilde{P}H_k^T)^{-1} \end{aligned}$$

4.2 Modified Extended Kalman Filter

Since the sensor outputs are provided at discrete intervals of time, it is appropriate to express the system modeling, shown in equation (4.1), in the form of discrete differential equations:

$$\begin{aligned} x_{k+1} &= \phi_k x_k + \eta_k \\ z_{k+1} &= H_{k+1} x_{k+1} + n_{k+1} \end{aligned} \tag{4.10}$$

where

$$\begin{aligned} \phi_k &= \exp[F(t_{k+1} - t_k)] \\ F(t_k) &\equiv \left.\frac{\partial f}{\partial x}\right|_{x=\hat{x}_k} \end{aligned} \tag{4.11}$$

4.2.1 System Model

According to equations (2.50), (4.10), and (4.11), the discrete form of the system is developed as:

$$\begin{aligned} r_{k+1} &= r_k + T_i v_k \\ v_{k+1} &= v_k + T_i(C_k a_k + g_n + C_k \eta_{1k}) \\ q_{k+1} &= (I + 0.5 T_i \Omega) q_k + 0.5 Q(q_k) \eta_{2k} \\ a &= f_A + \dot{\omega} \times r_{B/A} + \omega \times (\omega \times r_{B/A}) \end{aligned} \tag{4.12}$$

where T_i is the sampling rate of the inertial sensors. In this research, instead of estimating the actual value of these quantities, we propose to estimate how much the position and the velocity will be changed; that is,

$$\begin{aligned} \Delta r_{k+1} &= r_{k+1} - r_k \\ \Delta v_{k+1} &= v_{k+1} - v_k \end{aligned} \tag{4.13}$$

Substituting equation (4.13) into equation (4.12) gives the following results:

$$\begin{gathered} \Delta r_{k+1} = r_k + T_i v_k - r_{k-1} - T_i v_{k-1} = (r_k - x_{k-1}) + T_i(v_k - v_{k-1}) \\ \Longrightarrow \Delta r_{k+1} = \Delta r_k + T_i \Delta v_k \end{gathered} \tag{4.14}$$

and

$$\begin{aligned}
\Delta v_{k+1} &= v_k + T_i(C_k a_k + g_n + C_k \eta_{1k}) - v_{k-1} - T_i\big(C_{k-1} a_{k-1} + g_n + C_{k-1}\eta_{1(k-1)}\big) \\
&= (v_k - v_{k-1}) + T_i(C_k a_k - C_{k-1} a_{k-1}) + T_i\big(C_k \eta_{1k} - C_{k-1}\eta_{1(k-1)}\big) \\
&= \Delta v_k + T_i(C_k a_{k-1} - C_{k-1} a_{k-1} + C_k a_k - C_k a_{k-1}) \\
&+ T_i\big(C_k \eta_{1k} - C_{k-1}\eta_{1(k-1)} + C_{k-1}\eta_{1k} - C_{k-1}\eta_{1k}\big) \\
&\Longrightarrow \Delta v_{k+1} = \Delta v_k + T_i(\Delta C_k a_{k-1} + C_k \Delta a_k + \Delta C_k \eta_{1k} + 2C_k \eta_{1k})
\end{aligned} \tag{4.15}$$

As a consequence, the effect of the gravitational force is removed in the state-space model. In fact, the error caused by inaccurate value of the gravitational force in the state-space model is completely eliminated.

The inertial sensor noise is theoretically modeled with a zero-mean Gaussian random process. In practice, the average of the noise is not absolutely zero. Due to the inherent characteristic of the Gaussian random process, the discrete difference of a zero-mean Gaussian random process is also a zero-mean Gaussian random process with very lower actual mean while its variance is twice of the variance of the original process.

Figure 74 shows a zero-mean Gaussian random process with σ=0.01 when the actual mean is -0.0012. While the program is generating this process, its discrete difference is calculated. As illustrated in Figure 74, its discrete difference is also a zero-mean Gaussian random process with σ=0.02 and actual mean=-0.000012. This shows that the average of the process is significantly reduced. As a result, the drift resulting from the input noise is reduced and a smooth positioning is expected.

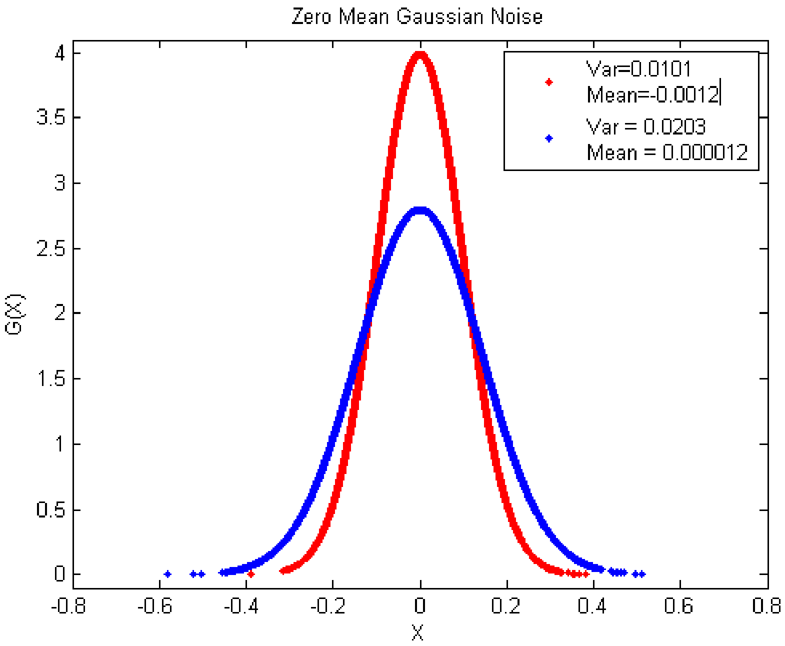

Figure 74 – The discrete difference of a Zero-mean Gaussian noise:

original signal (red) discrete difference (blue)

The equations of the SDINS with the state vector $X = [\Delta x \;\; \Delta v \;\; q]^T$ can be reformulated as:

$$\begin{bmatrix} \dot{\Delta \mathrm{r}} \\ \dot{\Delta v} \\ \dot{q} \end{bmatrix} = \begin{bmatrix} 0 & I & 0 \\ 0 & 0 & 0 \\ 0 & 0 & 0.5\Lambda \end{bmatrix} \begin{bmatrix} \Delta r \\ \Delta v \\ q \end{bmatrix} + \begin{bmatrix} 0 \\ \Delta Ca + C\Delta a \\ 0 \end{bmatrix} + \begin{bmatrix} 0 & 0 \\ 0 & \Delta C + 2C \\ 0.5Q(q) & 0 \end{bmatrix} \eta(t) \tag{4.16}$$

or

$$\begin{bmatrix} \dot{\Delta \mathrm{r}} \\ \dot{\Delta v} \\ \dot{q} \end{bmatrix} = \begin{bmatrix} \Delta v \\ \Delta Ca + C\Delta a \\ 0.5\Lambda\, q \end{bmatrix} + \begin{bmatrix} 0 & 0 \\ 0 & \Delta C + 2C \\ 0.5Q(q) & 0 \end{bmatrix} \eta(t) \tag{4.17}$$

Then the input matrix f is defined as:

$$f = \begin{bmatrix} \Delta v \\ \Delta C a + C \Delta a \\ 0.5 \Lambda \, q \end{bmatrix} \tag{4.18}$$

Subsequently, the transition matrix [108, 109] is calculated as:

$$F \equiv \left. \frac{\partial f}{\partial X} \right|_{X = \overbrace{X}} = \begin{bmatrix} 0 & I & 0 \\ 0 & 0 & \dfrac{\partial}{\partial q}(\Delta C a + C \Delta a) \\ 0 & 0 & 0.5 \Lambda \end{bmatrix} \tag{4.19}$$

By considering $\Delta a = [\Delta_1 \ \Delta_2 \ \Delta_3]^T$:,

$$\frac{\partial}{\partial q} C \Delta a = 2 \begin{bmatrix} q_1\Delta_1 - q_4\Delta_2 + q_3\Delta_3 & q_2\Delta_1 + q_3\Delta_2 + q_4\Delta_3 & -q_3\Delta_1 + q_2\Delta_2 + q_1\Delta_3 & -q_4\Delta_1 - q_1\Delta_2 + q_2\Delta_3 \\ q_4\Delta_1 + q_1\Delta_2 - q_4\Delta_3 & q_3\Delta_1 - q_2\Delta_2 - q_1\Delta_3 & q_2\Delta_1 + q_3\Delta_2 + q_4\Delta_3 & q_1\Delta_1 - q_4\Delta_2 - q_1\Delta_3 \\ -q_3\Delta_1 + q_2\Delta_2 + q_1\Delta_3 & q_4\Delta_1 + q_1\Delta_2 - q_2\Delta_3 & -q_1\Delta_1 + q_4\Delta_2 - q_3\Delta_3 & q_2\Delta_1 + q_3\Delta_2 + q_4\Delta_3 \end{bmatrix} \tag{4.20}$$

Substituting $\dot{C} = \lim\limits_{\Delta t \to 0} \left(\frac{\Delta C}{\Delta t} \right)$, where $\Delta t = T$, into equation (2.38) leads to the following equation:

$$\Delta C = -T_i C \Omega \tag{4.21}$$

Subsequently,

$$\frac{\partial}{\partial q} \Delta C a = \frac{\partial}{\partial q}(-T_i C \Omega a) = -T_i \frac{\partial}{\partial q} C \alpha \tag{4.22}$$

$$\alpha = \Omega a = \begin{bmatrix} \alpha_1 \\ \alpha_2 \\ \alpha_3 \end{bmatrix} = \begin{bmatrix} -\omega_3 a_2 + \omega_2 a_3 \\ \omega_3 a_1 - \omega_1 a_2 \\ \omega_2 a_1 + \omega_1 a_2 \end{bmatrix}$$

As a result of equation (4.22):

$$\frac{\partial}{\partial q} C \alpha = 2 \begin{bmatrix} q_1\alpha_1 - q_4\alpha_2 + q_3\alpha_3 & q_2\alpha_1 + q_3\alpha_2 + q_4\alpha_3 & -q_3\alpha_1 + q_2\alpha_2 + q_1\alpha_3 & -q_4\alpha_1 - q_1\alpha_2 + q_2\alpha_3 \\ q_4\alpha_1 + q_1\alpha_2 - q_4\alpha_3 & q_3\alpha_1 - q_2\alpha_2 - q_1\alpha_3 & q_2\alpha_1 + q_3\alpha_2 + q_4\alpha_3 & q_1\alpha_1 - q_4\alpha_2 - q_1\alpha_3 \\ -q_3\alpha_1 + q_2\alpha_2 + q_1\alpha_3 & q_4\alpha_1 + q_1\alpha_2 - q_2\alpha_3 & -q_1\alpha_1 + q_4\alpha_2 - q_3\alpha_3 & q_2\alpha_1 + q_3\alpha_2 + q_4\alpha_3 \end{bmatrix} \tag{4.23}$$

4.2.2 Measurement Model

Since the vision system as the measurement system provides the position of the tool tip, velocity can be computed from knowledge of the present and the previous position at each time step:

$$\begin{aligned} \tilde{z} &= z + n = \begin{bmatrix} \tilde{r} \\ \tilde{v} \end{bmatrix} \\ \tilde{v}_{l+1} &= \frac{\tilde{r}_{l+1} - \tilde{r}_l}{T_v} \end{aligned} \tag{4.24}$$

where T_v is the sampling rate of the cameras. Accordingly, the measurement model related to the new state-space is:

$$\begin{aligned} \Delta z_{k+1} &= \begin{bmatrix} I & 0 & 0 \\ 0 & I & 0 \\ 0 & 0 & 0 \end{bmatrix} \begin{bmatrix} \Delta r_{k+1} \\ \Delta v_{k+1} \\ q_{k+1} \end{bmatrix} + n_{k+1} \\ \Delta v_{k+1} &= \frac{T_i}{2T_v} (\Delta r_{k+1} - \Delta r_k) \end{aligned} \tag{4.25}$$

Subsequently, the observation matrix is derived as:

$$H = \begin{bmatrix} 0 & I & 0 \\ 0 & I & 0 \\ 0 & 0 & 0 \end{bmatrix} \tag{4.26}$$

As a result, the predication and update steps of the EKF can be written as:

Prediction:

$$\begin{aligned} \tilde{x}_{k+1} &= f\left(\overbrace{x}_k\,, k\right) \\ \tilde{P} &= F_k P_k F_k^T + G_k R_k G_k^T \end{aligned}$$

Update: (4.27)

$$\begin{aligned} \overbrace{x}_{k+1} &= x_{k+1} + K[z_{k+1} - h(\tilde{x}_k, k)] \\ P_{k+1} &= \tilde{P} - K H_k \tilde{P} \\ K &= \tilde{P} H_k^T (2S_k + H_k \tilde{P} H_k^T)^{-1} \end{aligned}$$

4.3 Experimental Result

This section presents the experimental result of applying EKF and the proposed Kalman filter. The experimental hardware includes a 3DX-GX1 IMU from Microstrain, an IDS Falcon Quattro PCIe frame grabber from IDS Imaging Development Systems, and four surveillance IR-CCD cameras.

The integration of the SDINS and multi-camera vision system is accomplished by using classical EKF and modified EKF described in section 4.2. The system model and measurement model, which are derived in section 4.1 and 4.2, are substituted into the prediction and update steps.

The position estimated by both versions of Kalman filter is compared with the position estimated by the vision system and the original path. The sensor fusion techniques allow us estimating the states variables of the system at the sampling rate of the sensor with the highest measurement rate. In this experiment, the sampling rate of cameras and inertial sensors are 20 fps and 100 Hz. As a result of sensor fusion, the measurement rate of the proposed integrated system is 100 HZ. In addition, the classical EKF is applied in both switch and continues modes. In the switch mode, the estimation of the states variables is corrected whenever the measurement of the vision system is available. Otherwise, the states are estimated only based on the SDINS.

In order to reduce the computational complexity of image processing algorithms, sensor fusion allows that the sampling rate of the vision system can be reduced to 10 fps and 5 fps.

As illustrated in Table 8, the positioning error is increased by reducing the sampling rate of the cameras. In addition, the error in proposed EKF grows faster than the other methods; since this technique assumes that the rate of the changes in state variables is constant from one frame to another frame. So, this assumption cannot be valid in lower measurement rates. Although, it is shown in that the position error of the continuous EKF is less than the others; it should be mentioned that the position obtained by the multi-camera vision system still has errors compared with the predesigned path. As mentioned in section 3.3.5, the actual traced path is not measureable.

Table 8 - Positions estimated by different estimation methods are compared with the position estimated by the multi-camera vision system

	Proposed EKF		EKF (Switch)		EKF (Continuous)	
Cameras Measurement Rate	Error (RMS)	Variance	Error (RMS)	Variance	Error (RMS)	Variance
16 fps	0.9854	0.1779	1.0076	0.7851	0.4320	0.1386
10 fps	1.0883	0.3197	1.2147	0.8343	0.5658	0.2149
5 fps	1.4730	1.5173	1.3278	0.8755	0.7257	0.8025

Figure 75 and Figure 76 compare the position resulting from each method at two different parts of the trajectory of the tool tip at two sampling rate of 16 fps and 5 fps. As shown, the camera path is traced smoothly by applying continuous EKF. Since the position is estimated in real-time, it is not possible to fit a curve between each two camera measurement without sensor fusion techniques. The position resulting from switch EKF is crinkly due to the drift position in the SDINS and the wrinkles are amplified by decreasing the measurement rate of the cameras. The position estimated by the proposed EKF is smooth and ripple-free and this method tries to reduce the errors of the entire system compared with the predesigned path.

As a result, the proposed EKF is suitable for the higher measurement rate; while the continuous EKF is recommended for the lower sampling rate.

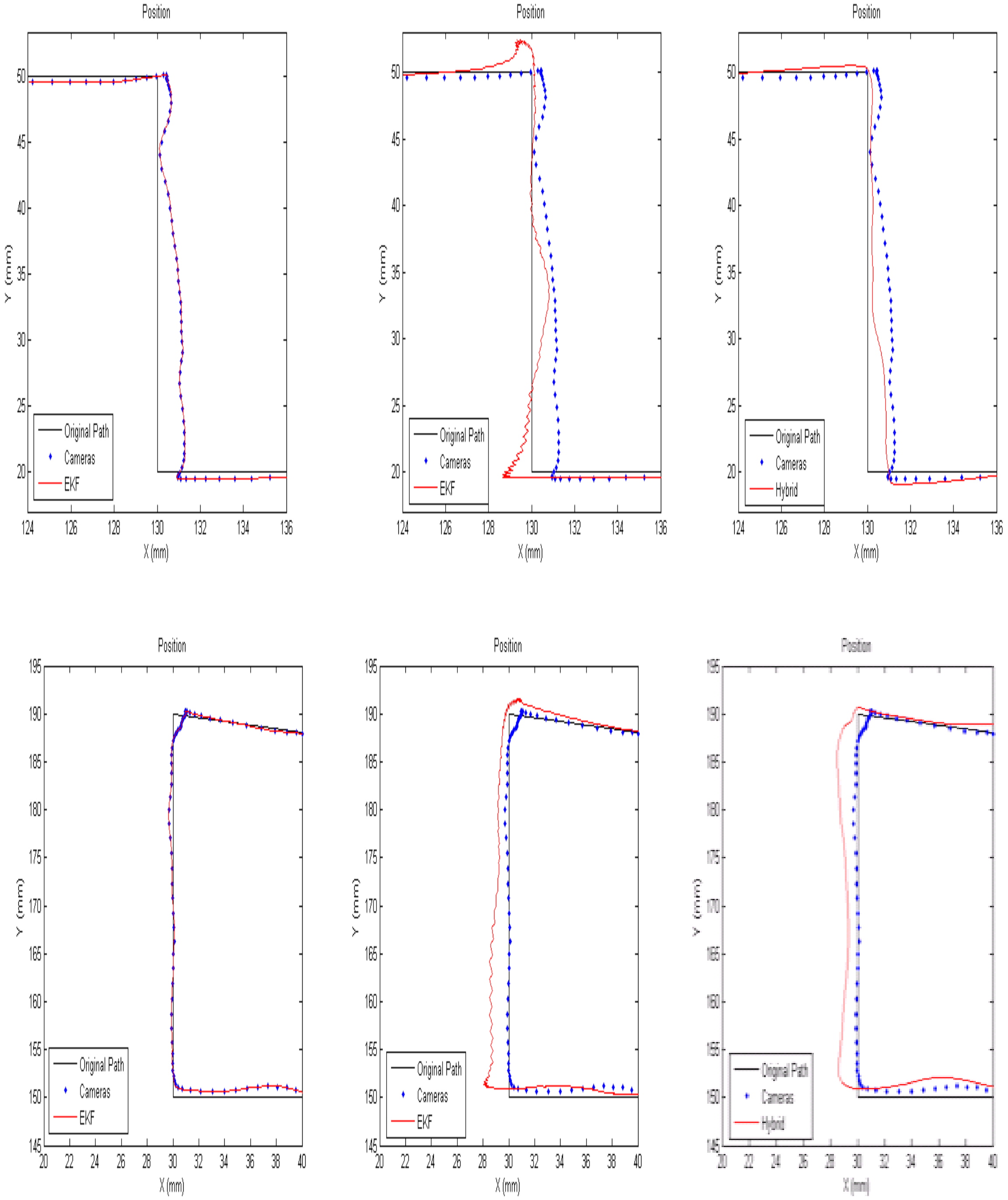

Figure 75 - Estimated position by applying different estimation method: continuous EKF (left), Switch EKF (center), and proposed EKF (right); when the sampling rate of the cameras is 16 fps.

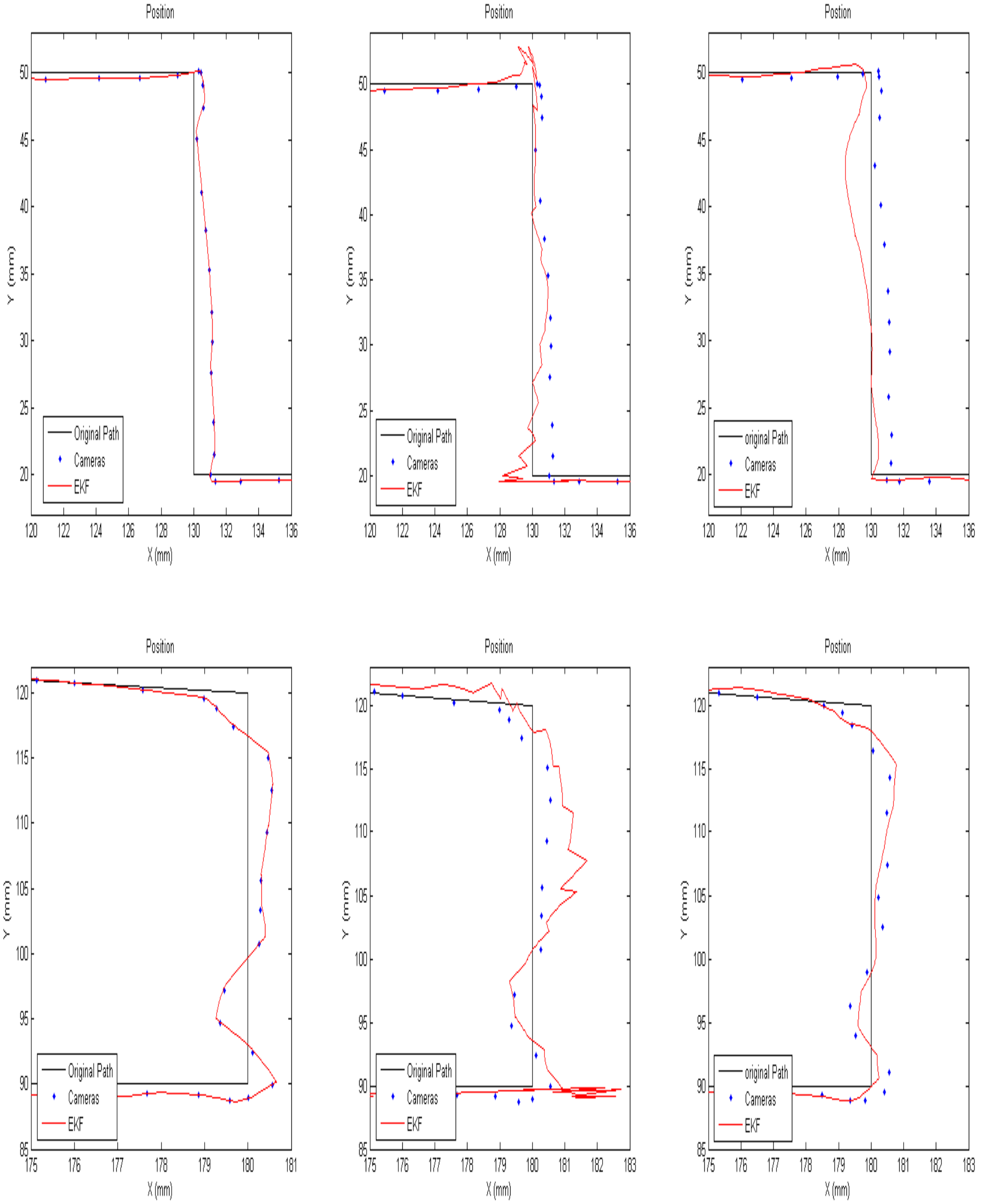

Figure 76 - Estimated position by applying different estimation method: continuous EKF (left), Switch EKF (center), and proposed EKF (right); when the sampling rate of the cameras is 5 fps.

However, the error of inertial sensors resulting from noise and the common motion-dependent errors are compensated according to chapter 2, but the remaining errors cause the position error estimation in the integrated system. In addition, the video tracking errors lead to the position estimation error as well. Since the vision data and inertial sensor outputs were not synchronized by hardware but they were synchronized later manually, new errors were introduced in the system.

4.4 Summary

This chapter describes the use of the EKF to develop integration of the multi-camera vision system and inertial sensors. The sensor fusion techniques allow estimating the state variables at the sampling rate of the sensor with highest measurement rate. This helps to reduce the sampling rate of the sensors with high computational load.

The classical EKF is designed for nonlinear dynamic system such as the strapdown inertial navigation system. The performance of the classical EKF is reduced by lowering the sampling rate of the cameras. When the sampling rate of the cameras is reduced, the rate of updating decreases and the system must rely more on the inertial sensors output for estimating the position. Because of the drift in the SDINS, the position error increases.

The modified EKF is proposed to obtain position estimation with less error. Furthermore, it removes the effect of the gravitational force in the state-space model. In fact, the error resulting from inaccuracy in the evaluation of the gravitational force is eliminated in the state-space model. In addition, the estimated position is smooth and ripple-free. However; the proposed EKF is not convincing at the lower measurement rate.

The error of the estimated position is resulted by inertial sensor errors, uncompensated common motion-dependent errors, attitude errors, video tracking errors, and unsynchronized data.

Chapter 5

Conclusion and Future Work

This chapter reviews the material presented throughout the research and summarizes the major findings and limitations of the study. It also discusses the contribution of this research to the state of knowledge on the subject and provides suggestions for future work.

5.1 Conclusion

Chapter 1 discusses the problem of localization in the field of medical operation applications, presents the available technologies, and describes their limitations in this area. It then introduces the novel idea of the integration of the multi-camera vision system and strapdown inertial navigation system by using a modified EKF, and compares it with other approaches. The chapter also previews the organization of the thesis.

Chapter 2 describes the strapdown inertial navigation system and its implementation requirements. It then introduces inertial sensors and inertial measurement units. The chapter also presents the fundamental idea of the IMU design and its calibration procedure, which includes the computation of the scale factors and compensations for the sensor misalignment, sensor bias, and sensor sensitivity to temperature and gravitational force. In addition, it illustrates how the sensor outputs are impacted by the common motion-dependent components and presents an algorithm to remove these components from the measurements by applying the relative-motion analysis. This chapter also expresses that physiological hand tremor adds Gaussian random noise to the system. Therefore, the errors produced by the sensor noise and the tool vibration are diminished by applying a low pass filter, while the drift resulted by the accelerometer bias is reduced by employing a high pass filter. Finally, the strapdown inertial navigation computing task is developed to estimate the position and attitude of the hand-held tool in addressing the common motion-dependent errors and noise problems. The experimental results show the significant improvement of the system performance. The resulting errors are reduced considerably, but the remaining attitude error is still great enough to cause a drift in the position estimation.

Chapter 3 describes the Local Positioning Systems and available tracking technologies. It then proposes a multi-camera vision system that includes four IR-CCD cameras which are aligned along a semicircle. The chapter also describes the multi-camera vision system calibration procedure, which includes single- and stereo-calibration processes for estimating the intrinsic and extrinsic cameras parameters, and compares it with the calibration procedure for the straight line configuration. The algorithm for aligning the world coordinate system on the navigation frame is also presented. The experimental results of the proposed multi-camera vision system compared with those of the stereo vision system show that the new configuration can cover the entire workspace, reduce the possibility of the loss of line-of-sight, and increase the accuracy of the vision system. As usual, the precision of the vision system depends on the quality of the cameras, precision of the calibration process, and accuracy of the object detection algorithms. Reducing the error of video tracking requires the complex computer vision algorithms. Employing these algorithms requires the use of advanced, high-speed, and multi-processor PCs to respond in real time.

Chapter 4 presents two different extended Kalman filters for integration of the multi-camera vision system and inertial sensors. These methods allow estimating position at the sampling rate of the inertial sensors which have the higher measurement rate than the cameras'. The result of both version of the Kalman filter shows improvement in the system performance. Since the modified EKF removes the effect of the gravitational force in the state-space model, the error resulting from inaccurate value of the gravitational force in the state-space model is eliminated. In addition, the modified EKF reduces the error of the position estimation and results smooth and ripple free position.

Furthermore, the proposed integrated tracking system compared with the multi-camera vision system allows a reduction of the sampling rate of the cameras without loss of accuracy. When the sampling rate is reduced, the system implementation does not require a highly advanced PC and system responses in real-time.

5.2 Contributions

The objective of this thesis is the design of a reliable and cost-effective positioning system with capability of the tool localization by estimating its position and orientation in real-time. The major contributions of this research are as follows:

The system is designed based on the cost-effective factor, since the precise available positioning systems are not affordable to be used in many applications.

Responding in real time is one of the most important contributions of this research. The sampling rate of the proposed positioning system is 100Hz at all time of its operation.

The low-cost MEMS-based IMU including three accelerometers and three rate gyros is introduced to the system in order to provide high frequency and full dynamic range of the motion. Although, the general equations of the SDINS computing task are applied in many navigation applications; but the accuracy of the tool tracking system should be in the range of few millimeters. This requires developing precise kinematics equations in order to minimize the SDINS errors resulting from the common motion-dependent errors as much as possible. The 3D relative motion analysis and developing required 3D kinematics equations for the hand-held tool is the other essential contribution of this thesis.

Even though, the drift error of the SDINS is significantly reduced by developing 3D kinematics equations; but the SDINS still lose its accuracy over the time. It is recommended that the SDINS is integrated with a vision system associated with a sensor fusion technique to improve the accuracy of the system and keep it in the desired range for a longer period of the time. As a matter of cost effectiveness, it is proposed to employ the low-cost CCD cameras in the proposed vision system.

Another significant contribution of this research is the design of a multi-camera vision system with individual configuration so as to prevent the loss of line of sight as much as possible. This configuration proposes to place the cameras along a semicircle in order to expand the angle of view and initiate a wide circular field of view. As a result of this arrangement, an individual calibration procedure is designed to estimate the intrinsic and extrinsic parameters of the multi-camera vision system, which includes the required 3D transformation to map each point expressed in the world coordinate system of the multi-camera vision system into the SDINS navigation frame.

To address the computation load problem of the video tracking, the simple and efficient algorithms for application in hand are selected.

Integration of the multi-camera vision system and SDINS requires an estimation method. This research develops an EKF which offers the estimation of the changes in the state variables.

According to the general equations of the SDINS, the constant value of the gravitational force is removed from the resulted equations and the resulting error from the uncertainty value of the gravitational force is eliminated. As a result of the proposed EKF, it is expected that the resulting drift from input noise is reduced and smooth positioning is obtained.

5.3 Future Work and Research

The design of the integrated multi-camera vision system and strapdown inertial navigation system has not been completed in this research. More engineering efforts are required to overcome the existing bottlenecks in the proposed system.

The performance of the system can be improved by making a few design changes in both the hand-held tool and the multi-camera vision system.

Since the MEMS-based inertial sensors are quite small, the inertial sensors can be placed inside of the tool and as close as possible to the tool tip. Redesigning the hand-held tool would help to reduce the effect of the common motion-dependent errors. Besides, adding a magnetometer per axis, which is not affected by these motions, would help to reduce the attitude errors, resulting in less error in the position estimation. In addition, the resolution of available IMUs, which use a 16-bit analogue to digital converter, is about 5 mg. However, the micromanipulation application requires a better resolution, which can be provided by a 24-bit analogue-to-digital converter.

The performance of the multi-camera vision system can be increased by using eight CCD cameras with a 45° field of view angle or twelve CCD cameras with a 30° field of view angle which can be placed along a circle. However, a complex calibration procedure must be performed to obtain the intrinsic and extrinsic parameters of the multi-camera vision system. Using the low-cost CCD cameras with a higher resolution would help to reduce the error of video tracking algorithms.

In order to synchronize the multi-camera vision system and inertial sensors, additional hardware is required to initiate both systems and obtain their outputs simultaneously.

Aside from the hardware design enhancement, improvement of the software is also required. Future work can focus on reducing the position and attitude error by considering the effects of the coning, sculling, and rotational motion more precisely in the position and attitude computation equations in the strapdown inertial navigation computing task.

Also, the computer vision algorithms proposed in this research for object detection, image segmentation, and object tracking can be enhanced by a few changes or be replaced by new simple and efficient techniques. The orientation of the hand-held tool was not computed by using video tracking algorithm in this research. This estimation can reduce the error of the attitude and position estimation in SDINS by taking into account in the measurement model of the Kalman filter.

Finally, the classical or modified Kalman filter would be developed for the system through these changes.

Although this research focuses on the hand-held tool tracking application, the concept of performing compensation for the common motion-dependent errors, developing the multi-camera vision system, and integrating the different sensors has enormous application in the localization tasks that require accuracy enhancement.

The tracking system developed in this thesis can be applied in a variety of areas such as industry, medicine, human motion tracking, and sports.

Bibliography

1 Rebello, K.J. 2004. "*Applications of MEMS in Surgery,*" Proceedings of the IEEE, Vol. 92, No. 1, pp 43-55.

2 Titterton, D.H., and Weston, J.L., 2004. *Strapdown Inertial Navigation Technology*. The institution of Electrical Engineers, 2nd Edition.

3 J. Farrell, J., and Barth, M., 1999. *Global Positioning System and Inertial Navigation*, McGraw-Hill.

4 Northern Digital Inc., Optotrak, *http://www.ndigital.com/*

5 Ang, W.T., Riviere, C.N., and Khosla, K. 2001. *"Design and Implementation of Active Error Cancelling in Hand-held Microsurgical Instrument,"* Proceedings of IEEE/RSJ International Con. on Intelligent Robots and Systems, pp. 1106-1111.

6 Ang, W.T. 2004, "*Active Tremor Compensation in Handheld Instrument for Microsurgery,"* PhD Thesis, tech. report CMU-RI-TR-04-28, Robotics Institute, Carnegie Mellon University, May, 2004.

7 Ang, W.T., Khosla, K., and Riviere, C.N. 2004. "*Kalman Filtering for Real-Time Orientation Tracking of Handheld Microsurgical Instrument,*" Proceedings of IEEE/RSJ International Con. on Intelligent Robots and Systems, pp. 2574-2580.

8 Tao, Y., and Hu, H. 2008. *"A Novel Sensing and Data Fusion System for 3D Arm Motion Tracking in Tele-Rehabilitation,"* IEEE Transaction on Instrumentation and Measurements, Vol. 75, No. 5, pp. 1029-1040.

9 Tao, Y., Hu, H., and Zhou, H. 2007. *"Integration of Vision and Inertial Sensors for 3D Arm Motion Tracking in Home-based Rehabilitation,"* International Journal of Robotics Research, Vol. 26, No. 6, pp. 607-624.

10 Zhang, S.M., Hu, H., and Zhou, H. 2008. *"An Interactive Internet-based System for Tracking Upper Limb Motion in Home-based Rehabilitation,"* Journal of Medical Biological Engineering and Computing, Vol. 46, No. 3, pp. 241-249.

11 Zhou, H., and Hu, H., 2007. *"Inertial Sensors for Motion Detection of Human Upper Limbs,"* Journal of Sensor Review, Vol. 27, No. 2, pages 151-158.

12 Rehbinder, H., and Hu, X. 2001. *"Drift-Free Attitude Estimation for Accelerated Rigid Bodies,"* Proceedings of IEEE International Conference on Robotics & Automation, pp. 4244-4249.

13 Luinge, H.J. 2002. *"Inertial Sensing of Human Movement,"* PhD. Thesis, University of Twente, University Press.

14 Foxlin E., Harrington M., and Altshuler Y. 1998. *"Miniature 6-DOF Inertial System for Tracking HMDs,"* In SPIE Vol. 3362, Helmet and Head-Mounted Displays III, AeroSense 98, pp. 214-228.

15 Foxlin E. 1996, *"Inertial Head-Tracker Sensor Fusion by a Complementary Separate-Bias Kalman Filter,"* IEEE Proc. of VRAIS '96, pp. 185-194.

16 Bachmann, E.R., Yun, X., McKinney, D., McGhee, R.B., and Zyda, M.J. 2003. *"Design and Implementation of MARG Sensors for 3DOF Orientation Measurement of Rigid Bodies,"* Proceedings of IEEE International Con. on Robots & Automation, pp.1171-1178.

17 Yun, X., Lizarrage, M. Bachmann, E.R., and McGhee. 2003. *"An Improved Quaternion-Based Kalman Filter for Real-Time Tracking of Rigid Body Orientation,"* Proceedings of IEEE/RSJ International Con. on Intelligent Robots and Systems, pp. 1074-1079.

18 Gebre-Egziabher, D., Elkaim, G.H., Powell, J.D., and Pakinson, B.W. 2000. *"A Gyro-Free Quaternion-Based Attitude Determination System Suitable for Implementation Using Low Cost Sensors,"* Proc. IEEE Position, Location, and Navigation Symp., pp. 185-192.

19 Hofmann-Wellenhof, B. 2001. *Global Positioning System: Theory and Practice*, 5th edition, Springer-Verlag.

20 Abuhadrous, I., Nashashibi, F., and Laurgeau, C. 2003. *"Multi-Sensor Fusion for Land Vehicle Localization Using* ^{RT}*MAPS,"* Proceedings of the 11th International Conference on Advanced Robotics, pp. 71-76.

21 Bian, H., Jin, Z., and Tian, W. 2005. *"Study on GPS Attitude Determination System Aided INS Using Adaptive Kalman Filter,*" Measurement Science and TechNology, Vol.16, pp. 2072–2079.

22 Crassidis, J.L., Lightsey, E.G., and Markley, F.L. 1999. *"Efficient and Optimal Attitude Determination Using Recursive Global Positioning System Signal Operations,"* Journal of Guidance, Control, and Dynamics, Vol.22, No.2, pp. 193-201.

23 Crassidis, J.L., and Markley, F.L., 1997. *"New Algorithm for Attitude Determination Using Global Positioning System Signals,"* Journal of Guidance, Control, and Dynamics, Vol. 20, No. 5, pp. 891-896.

24 Kumar, N.V. 2004. *"Integration of Inertial Navigation System and Global Positioning System Using Kalman Filtering,"* PhD. Thesis, Indian Institute of Technology.

25 Lee, T.G. 2003. *"Centralized Kalman Filter with Adaptive Measurement Fusion: it's Application to a GPS/SDINS Integration System with an Additional Sensor,"* International Journal of Control, Automation, and Systems, Vol. 1, No. 4, pp. 444-452.

26 Chung, H., Ojeda, L., and Borenstein, J. 2001. *"Sensor fusion for Mobile Robot Dead-reckoning with a Precision-calibrated Fibre Optic Gyroscope,"* Proc. of IEEE International Conference on Robotics and Automation, pp. 3588-3593.

27 Chung, H., Ojeda, L., and Borenstein, J. 2004. *"Accurate Mobile Robot Dead-reckoning with a Precision-Calibrated Fibre Optic Gyroscope,*" IEEE Transactions on Robotics and Automation, Vol. 17, No. 1, pp. 80-84.

28 Persa, S., and Jonker, P. 2002. *"Multi-sensor Robot Navigation System,"* Proc. SPIE Int. Soc. Opt. Eng., Vol. 4573, pp. 187-194.

29 Huster, A. 2003. *"Relative Position Sensing by Fusing Monocular Vision and Inertial Rate Sensors,"* PhD. Thesis, Stanford University.

30 Foxlin, E., and Naimark, L. 2003. *"VIS-Tracker: A Wearable Vision-Inertial Self-Tracker,"* Proceedings of IEEE Virtual Reality, pp. 199-206.

31 You, S., Neumann, U., and Azuma, R. 1999. *"Hybrid Inertial and Vision Tracking for Augmented Reality Registration,"* Proceedings of IEEE Virtual Reality, pp. 260-267.

32 Lang, P., and Pinz, A. 2005. *"Calibration of Hybrid Vision / Inertial Tracking Systems,"* Proceedings of the 2nd InerVis: Workshop on Integration of Vision and Inertial Sensors.

33 Parnian N., and Golnaraghi, F., 2007. "*Integration of Vision and Inertial Sensors for Industrial Tools Tracking,"* Sensor Review, Vol. 27, No. 2, pp. 132-141.

34 Werb, J., and Lanzl, C. 1998. *"Designing a Positioning System for Finding Things and People Indoors*," IEEE Spectrum, Vol. 35, No. 9, pp. 71–78.

35 Kantor, G., and Singh, S. 2002. *"Preliminary Results in Range–Only Localization and Mapping,"* Proceedings of IEEE International Conference on Robotics and Automation, Vol. 2, pp. 1818-1823.

36 Shim, H.S., Kim, H.S., Jung, M.J., Choi, I.H., Kim, J.H., and Kim, J.O. 1997. *"Designing Distributed Control Architecture for Cooperative Multi-Agent System and Its Real-Time Application to Soccer Robot,"* ELSEVIER Science, Robotics and Autonomous Systems, Vol. 21, pp. 149-165.

37 Tsou, M.H. 2004. *"Integrated Mobile GIS and Wireless Internet Map Servers for Environmental Monitoring and Management,"* Cartography and Geographic Information Science, Vol. 31, No. 3, pp. 153-165.

38 Giraldo, C., Helal, S., and Mann, W. 2002. *"*mPCA – *A Mobile Patient Care-Giving Assistant for Alzheimer Patients,"* The First International Conference on Ubiquitous Computing.

39 Zekavat, S.A., Tong, H., and Tan, J. 2004. *"A Novel Wireless Local Positioning System for Airport (Indoor) Security,"*Proc. of SPIE, Vol. 5403, pp. 522-533.

40 Aitenbichler, E., and Mühlhäuser, M. 2003. *"An IR Local Positioning System for Smart Items and Devices,"* Proceedings of the 23rd International Conference on Distributed Computing Systems Workshops, pp. 334-339.

41 Hightower, J., and Borriello, G. 2001. *"Location Systems for Ubiquitous Computing,"* IEEE Journal of Computer, Vol. 34, No. 8, pp. 57-66.

42 Steggles, P., and Batty, P. 2003. *"Local Positioning Systems: New Possibilities for Urban Combat Training,"* Ubisense Ltd, IITSEC 2003, pp.1-21.

43 Kelly, I., and Martinoli, A. 2004. *"A Scalable, On-board Localisation and Communication System for Indoor Multi-Robot Experiments,"* Sensor Review, Vol. 24, No. 2, pp. 167–180.

44 Pfeifer, T., and Elias, D. 2003. "*Commercial Hybrid IR/RF Local Positioning System,*" Kommunikation in Verteilten Systemen, Springer, Series: Informatik Aktuell, pp. 119-127.

45 Cybernet Interactive, Firefly Motion Capture System, *http://www.cybernet.com/interactive/*

46 Grewal, M., Weill, L.R., and Andrews, A. P., 2007. *Global Positioning Systems, Inertial Navigation, and Integration,* John Wiley & Sons, 2nd Edition.

47 Ojeda, L., Chung, H., and Borenstein, J. 2000. *"Precision-calibration of Fiber-optics Gyroscopes for Mobile Robot Navigation*," Proceedings of IEEE International Conference on Robotics & Automation, pp.2064-2069.

48 Lai, K.L., Crassidis, J.L., and Harman, R.R. 2003. *"In-Space Spacecraft Alignment Calibration Using the Unscented Filter,"* Proc. of AIAA Guidance, Navigation, and Control Conference and Exhibit, pp. 1-11.

49 Nassar, S., Schwarz, K.P., and El-Sheimy, N. 2004. *"Modeling Inertial Sensor Errors Using Autoregressive (AR) Models,"* Navigation-Alexandria, Vol. 51, No. 4, pp.259-268.

50 Pittelkau, M.E., 2001. *"Kalman Filtering for Spacecraft System Alignment Calibration,"* Journal of Guidance, Control and Dynamics, Vol. 24 No. 6, pp. 1187-1195.

51 Markley, F.L. 2003. *"Attitude Error Representation for Kalman Filtering,"* Journal of Guidance, Control and Dynamics, Vol. 26, No. 2, pp. 311-317.

52 Chatfield, A.B. 1997. *Fundamentals of High Accuracy Inertial Navigation,* American Institute of Aeronautics and Astronautics Inc, Vol. 174.

53 Aggarwal, P., Syed, Z., and El-Sheimy, N. 2008. *"Thermal Calibration of Low Cost MEMS Sensors for Land Vehicle Navigation System,"* IEEE Vehicular Technology Conference, pp. 2859-2863

54 Aggarwal, P., Syed, Z., Niu, *X* ., and El-Sheimy, N. 2008. *"A Standard Testing and Calibration Procedure for Low Cost MEMS Inertial Sensors and Units,"* The Journal of Navigation, Vol. 61, No. 2, pp. 323-336.

55 Ojeda, L., and Borenstein, J., 2007. *"Non-GPS Navigation with the Personal Dead-Reckoning System,"* Proceeding of SPIE, Volume 6561, pp. 65610C.

56 Foxlin, E., 2005. *"Pedestrian Tracking with Shoe-Mounted Inertial Sensors,"* IEEE Computer Graphics and Applications, Vol. 25, No. 6, pp. 38-46.

57 Huddle, J. 1998. *"Trends in Inertial Systems Technology for High Accuracy AUV Navigation,"* Proceedings of the 1998 Workshop on Autonomous Underwater vehicles, AUV'98, pp. 63-73.

58 Ledroz, A., Pech, E., Cramer, D., and Mintchev, M.P., 2005. *"FOG-Based Navigation in Downhole Environement During Horizontal Drilling Utilizing a Complete Inertial Measurement Unit: Directional Measurement-While-Drilling Surveying,"* IEEE Transactions on Instrumentation and Measurement, Vol. 54, No. 4, pp. 217-225.

59 Savage, P.G., 1998. *"Strapdown Inertial Navigation Integration Algorithm Design Part I: Attitude Algorithms,"* Journal of Guidance, Control, and Dynamics, Vol.21, No.1, pp. 19-28.

60 Savage, P.G., 1998. *"Strapdown Inertial Navigation Integration Algorithm Design Part 2: Velocity and Position Algorithms,"* Journal of Guidance, Control, and Dynamics, Vol.21, No.2, pp.208-221.

61 Hibbeler, R.C., 1998. *Enginnering Mechanics: Statics and Dynamics*, Prentice-Hall, 2nd Edition.

62 Greenwood, D.T., 2003. *Advanced Dynamics,* Cambridge, New York, Cambridge University Press.

63 Kajita, S., Kanehiro, F., Kaneko, K., Yokio, K., and Hirukawa, H., 2001. *"The 3D Linear Inverted pendulum Mode: A Simple Modeling for a Biped Walking Pattern generation,"* Proceeding of IEEE/RSJ International conference on Intelligent Robots and Systems, Vol. 1, pp. 239-246.

64 Friedland, B., 1974. *"Analysis Strapdown navigation Using Quaternions,"* IEEE Transaction on Aerospace and Electronic systems, Vol. AES-14, No. 5, pp.764-767.

65 Pittelkau, M.E., 2003. *"An Analysis of the Quaternion Attitude Determination Filter,"* Journal of Astronautical Sciences, Vol. 51, No. 1, pp. 103-120.

66 Markley, F.L. 2004. *"Multiplicative vs. Additive Filtering for Spacecraft Attitude Determination*," Proceeding. of the 6th Conference on Dynamics and Control of Systems and Structures in Space (DCSSS), pp.467-474.

67 Shepperd, S.W., 1978. *"Quaternion from Rotation Matrix,"* AIAA Journal of Guidance, Control, and Dynamics, Vol. 1, No. 3, pp 223-224.

68 Gaylor, D.E., 2003. *"Integrated GPS/INS Navigation System for Design for Autonomous Spacecraft Rendezvous,"* PhD Thesis, The University of Texas at Austin.

69 Bortz, J.E., 1971. *"A New Mathematical Formulation for Strapdown Inertial Navigation,"* IEEE Transaction on Aerospace and Electronic Systems, Vol. AES-7, No. 1, pp. 61-65.

70 Pittelkau, M. E., 2003. *"Rotation Vector in Attitude Estimation,"* Journal of Guidance, Control, and Dynamics, Vol. 26, No. 6, pp.855-860.

71 *http://jason.kamin.com/projects_files/equations.html,* Accessed on Sep. 19, 2008

72 *http://hypertextbook.com/facts/2002/JasonAtkins.shtml,* Accessed on Sep. 19, 2008

73 Zhang, J., and Chu, F., 2005. *"Real-Time Modeling and Prediction of Physiological Hand Tremor,"* Proceeding of Acoustics, Speech, and Signal Processing, Vol. 5, pp. v6445-v648.

74 Singh, S.P.N., and Riviere, C.N., 2002. *"Physiological tremor Amplitude During retinal Microsurgery,"* Proceeding of IEEE Annual Northeast Bioengineering Conference, pp. 171-172.

75 Gebre-Egziabher, D., Hayward, R.C., and Powell, J.D., 2004. *"Design of Multi-Sensor Attitude Determination Systems,"* IEEE Transaction on Aerospace and Electronic Systems, Vol. 40, No. 2.

76 Bouten,C.V.C., Koekkoek,K.T.M., Verduiin, M., Kodde, R., and Janssen, J.D. 1997. *"A Triaxial Accelerometer and Portable Data Processing Unit for the Assessment of Daily Physical Activity,"* IEEE Transactions on Biomedical Engineering, Vol. 44, N. 3, pp. 136-147.

77 Foerster, F., and Fahrenberg, J. 2000. *"Motion Pattern and Posture: Correctly Assessed by Calibrated Accelerometers,"* Behavior Research Method, Instrumenation, and |Computation,

Vol. 32, pp. 450-457.

78 Verburg, J., and Strackee, J. 1974. *"Phaseless Recursive Filtering Applied to Chest Wall Displacements and Velocities Using Accelerometers,"* Med. And Bio. Eng., Vol. 4, pp. 483-488

79 *http://www.microstrain.com/,* Accessed on Sep. 19, 2008

80 Okada, R., Kondoh, N., Stenger, B., 2007. *"A Video Motion Capture System for Interactive Games,"* Proceeding of Machine Vision Application, pp. 186-189.

81 Verplaetse, C., 1996. *"Inertial Proprioceptive Devices: Self-motion-sensing Toys and Tools,"* IBM Journal, Vol. 35, No. 3&4, pp. 639-650.

82 Bigun, J., 2006. *Vision with Direction: A Systematic Introduction to Image Processing and Computer Vision,* Springer-Verlag.

83 Tsai, R.Y., 1987. *"A Versatile Camera Calibration Technique for High Accuracy 3D Machine Vision Metrology Using Off-the-shelf TV Cameras and Lenses,"* IEEE Journal of Robotics and Automation, Vol. RA-3, No. 4, pp. 323-344.

84 Fryer, J.G., and Brown, D.C., 1986. "*Lens Distortion for Close-Range Photogrammetry*,*"* Photogrammetric Engineering and Remote Sensing Vol. 52, No. 1, pp 51-58.

85 Brown, D.C., 1966. "*Decentering Distortion of Lenses*," Photometric Engineering, Vol. 32, No. 3, pp. 444-462.

86 Brown, D.C., 1971. "*Close-Range Camera Calibration,"* Photogrammetric Engineering, Vol. 37, No. 8, pp. 855-866.

87 Yoneyama, S., Kikuta, H.,. Kitagawa, A., and Kitamura, K., 2006. "*Lens Distortion Correction for Digital Image Correlation by Measuring Rigid Body Displacement*," Optical engineering, Vol. 45, No. 2, pp. 023602(1)-023602(9).

88 Clarke, T.A., Fryer, J.G., and Wang, X., 1998 *"The Principal Point and CCD Cameras,"* The Photogrammetric Record, Vol. 16, No. 92, pp. 293-312.

89 Zhang, Z., 1999. *"Flexible Camera Calibration by Viewing a Plane from Unknown Orientations,"* Proceeding of IEEE International Conference on Computer Vision, Vol. 1, pp.666-673.

90 Forsyth, D.A., and Ponce, J., 2003. *Computer Vision: A Modern Approach*, Prentice-Hall.

91 Heikkila, J., 1997. "*Accurate Camera Calibration and Feature-based 3-D Reconstruction from Monocular Image Sequences",* Dissertation, University of Oulu.

92 Hartley, R., and Zisserman, A., 2003. *Multiple View Geometry in Computer Vision,* Cambridge University Press, 2nd Edition.

93 Seul, M., 2000. *Practical Algorithms for Image Analysis: Description, Examples, and Code,* Cambridge University Press.

94 Parker, J.R., 1997. *Algorithms for Image Processing and Computer Vision,* New York: Wiley Computer Publication.

95 Gonzalez, R.C., and Woods, R.E., 2008. *Digital Image Processing,* Prentice-Hall, 3rd Edition.

96 Russ, J.C., 2002. *The Image Processing Handbook,* CRC Press, 4th Edition.

97 Jain, A.K., 1989, *Fundamentals of Digital Image Processing,* Prentice-Hall.

98 Haralick, R.M., and Shapiro, L.G., 1992. *Computer and Robot Vision,* Adison-Wesely.

99 Soile, P., 2003. *Morphological Image Analysis: Principles and Applications,* Springer, 2nd Edition.

100 Klette, R., and Rosenfeld, A., 2004. *Digital Geometry,* Elsevier.

101 *http://www.vision.caltech.edu/bouguetj/calib_doc/,* Accessed on Sep. 19, 2008

102 Crassidis, J.L., and Markley, F.L., 2003*,"Unscented Filtering for Spacecraft Attitude Estimation,"* Journal of Guidance, Control and Dynamics, Vol. 26, No. 4, pp. 536-542.

103 Grewal, M.S., Henderson, V.D., and Miyasako, R.S., 1991. "*Application of Kalman Filtering to the Calibration and Alignment of Inertial Navigation Systems,"* IEEE Trans. on Automatic Control, Vol. 39, No. 1, pp.4-13.

104 Hu, C., Chen, W., Chen, Y., and Liu, D., 2003. *"Adaptive Kalman Filtering for Vehicle Navigation,"* Journal Of Global Positioning Systems, Vol. 2, No. 1, pp.42-47.

105 Merwe, R.V., and Wan, E.A., 2004. *"Sigma-Point Kalman Filters for Integrated Navigation,"* Proceedings of the 60th Annual Meeting of the Institute of Navigation, pp. 641-654.

106 Roumeliotis, S.I., Sukhatme, G.S., and Bekey, G.A., 1999. *"Circumventing Dynamic Modeling: Evaluation of the Error-State Kalman Filter applied to Mobile Robot Localization,"* Proceedings of IEEE International Conference on Robotics and Automation, Vol. 2, pp. 1656-1663.

107 Grewal, M.S., and Andrews, A.P., *Kalman Filtering: Theory and Practice Using MATLAB*, John Wiley, 2nd Edition.

108 Zarchan, P., and Musoff, H., 2005. *Fundamentals of Kalman Filtering: A Practical Approach*, AIAA, 2nd Edition, 2005.

109 Ristic, B., Arulampalam, S., and Gordon, N., 2004. *Beyond the Kalman Filter : Particle Filters for Tracking Applications,* Artech House.

Appendix A

Detailed Specification for MicroStrain IMU

	Parameter	Specification	Comments
Attitude	Range: Pitch, Roll, Yaw (°)	+/-90, 180, 180	No Attitude limitations
	Static Accuracy (°)	+/- 0.5	
	Dynamic Accuracy (° rms)	+/- 2	Typical, application dependent
	Repeatability (°)	+/- 0.2	
	Resolution (°)	0.1	
General Performance	A/D converter resolution (bits)	16	
	Turn on time (sec)	0.8	
	Analog output (Optional)	0.5V	4 channels, user configurable
	Update Rate (Hz maximum)	100	Orientation outputs
Physical	Size (mm)	65×90×25	With enclosure
		42×40×15	Without enclosure
	Weight(grams)	75	With enclosure
		30	Without enclosure
Electrical	Supply Voltage (V)	5.2-12 DC	
	Supply Current (mA)	65	
Environmental	Operating Temperature (°C)	-40 to +70	With enclosure
		-40 to +85	Without enclosure
	Vibration (g rms)	4	20-700, white
	Shock Limit (unpowered) (g)	1000	
	Shock Limit (powered) (g)	500	
Communications	Serial Interface	RS-232, RS-485	RS-485 networking optional
	Serial Communication Speed (kBaud)	19.2, 38.4, 115.2	User selectable
Angular Rate	Range (°/sec)	+/-300	Custom ranges available
	Bias:		
	1)Turn-on to turn-on repeatability (°/sec)	TBD	25°C fixed temperature
	2) In-Run stability, fixed temp. (°/sec)	0.1	After 15 minute warm up
	3) In-Run stability, over temp. (°/sec)	0.7	Over -40°C to +70°C range
	4) Short term stability (°/sec)	0.02	15 second Allan variance floor
	Angle random walk, noise (°/√hour)	3.5	Allan variance method
	Scale Factor Error (%)	0.5	Over -40°C to +70°C range
	Nonlinearity (% FS)	0.2	

	Resolution (°/sec)	0.01	
	G-sensitivity (°/sec/*g*)	0.01	With *g*-sensitivity
	Alignment (°)	0.2	compensation
	Bandwidth (Hz)	30	With alignment compensation
			-3dB Nominal
Acceleration	Range (g)	+/-5	Custom ranges available
	Bias:		
	1)Turn-on to turn-on repeatability (mg)	TBD	25°C fixed temperature
	2) In-Run stability, over temp. (mg)	10	Over -40°C to +70°C range
	3) Short term stability (mg)	0.2	15 second Allan variance floor
	Noise (mg/√Hz rms)	0.4	
	Scale Factor Error (%)	0.5	Over -40°C to +70°C range
	Nonlinearity (% FS)	0.2	
	Resolution (mg)	0.2	
	Alignment (°)	0.2	With alignment compensation
	Bandwidth (Hz)	50	-3dB Nominal
Magnetic Field	Range (Gauss)	+/-1.2	
	Bias:		
	1)Turn-on to turn-on repeatability (mGauss)	TBD	
	2) In-Run stability, over temp. (mGauss)		
	Noise (mGauss/√Hz)	15	Over -40°C to +70°C range
	Scale Factor Error (%)	TBD	
	Nonlinearity (% FS)	0.7	
	Resolution (mGauss)	0.4	
	Alignment (°)	0.2	
	Bandwidth (Hz)	0.2	With alignment compensation
		50	-3dB Nominal